4

Results and Discussion

In the present study, *Cyperus rotundus* (tuber), *Hemigraphis alternata* (leaves), and Pumice stone have been utilized to exploring traditional knowledge in depilation and skin substitute applications. Synthesis of gold nanoparticles, reduced graphene oxide, and gold nano–reduced graphene oxide composite has been explored. As mentioned above, the results of nanoparticle synthesis, characterization, biological activities, and cosmetic applications are discussed in the following pages.

Phase - I

Nanoparticle Synthesis and Biological Activities

4.1. Results of phytochemical assessment of *Cyperus rotundus* tuber and *Hemigraphis alternata* leaves

The identification and isolation of bioactive compounds from the plants are crucial due to the availability of new drugs with various medicinal properties. From the total world population, 80% of people depend on plant sources for their daily needs, like food, medicines and to maintain their health **(Romulo and Rosa, 2005)**. The plants consist of leaves, flowers, bark, root, tuber, fruit, *etc*. Each part is composed of numerous chemical constituents; it involves many biological and pharmacological activities.

The phytochemicals present in the plant extracts, prevent the living organism from various diseases. Alkaloids, flavonoids, terpenoids, sterols, and amino acids provide a significant role in many biological and pharmacological activities. Herbal ingredients are effectively used in cosmetics, and 70% of people prefer and use herbal-based cosmetics. The plant's chemical constitutes involved in various activity of many cosmetic products. It also exhibits long-term efficiency, and excellent property to replace synthetic chemicals **(Bijauliya *et al*., 2017)**.

The elution of phytoconstituents from the plant materials depends on the solvent polarity. Different solvents are used to extract the plant sample. This sequential extraction process helps to analyze the suitable solvent for the following studies based on extracting the major constituents from the plant. The presence of phytoconstituents was confirmed by colour test and the results are given in **Table 10**.

Table 10. Phytochemical assessment of different solvent extracts of CR and HA

W- Water**; EA-** Ethyl acetate**; CF-** Chloroform**; C-**Carbinol**; PE-** Pet Ether**; E-** Ethanol**; A-** Acetone

S. No	Test	*Cyperus rotundus* (tuber)							*Hemigraphis alternata* (leaves)						
		PE	EA	CF	C	A	E	W	PE	EA	CF	C	A	E	W
1	**Alkaloids**														
1 a	Dragendorff	-	+	-	+	+	+	+	+	-	+	+	+	-	+
2	**Flavonoids**														
2 a	NaOH	+	+	-	-	-	-	+	+	-	-	-	-	-	+
2 b	H_2SO_4	-	-	-	-	-	+	-	-	-	-	-	-	+	-
2 c	NH_4	-	-	-	+	-	-	+	-	-	-	-	-	-	-
2 d	Shinoda's	-	-	-	-	-	-	+	+	+	+	+	+	+	-
2 e	$ZnCl_2$	-	-	-	-	-	-	+	+	+	+	+	+	+	-
2 f	$FeCl_3$	-	-	-	-	-	-	+	-	-	-	-	-	-	-
2 g	Lead acetate	-	-	-	-	-	-	+	-	-	-	-	-	-	-
3	**Sterols**														
3 a	Liebermann-Burchard	+	+	+	+	+	+	-	-	-	-	+	-	+	-
3 b	Salkowski's	+	+	-	+	+	+	-	-	-	+	+	-	+	+
4	**Terpenoids**														
4 a	Liebermann-Burchard	+	-	-	-	-	-	-	+	-	-	-	-	-	-
5	**Anthraquinones**	-	-	-	+	+	+	-	-	-	-	-	-	-	-
6	**Anthocyanins**														
6 a	NaOH	-	-	-	-	-	-	-	+	+	-	+	+	+	-
7	**Proteins**														
7 a	Ninhydrin	-	-	+	+	-	-	+	-	+	+	+	+	+	+
7 b	Biuret	-	-	-	-	-	-	-	-	-	-	+	-	+	-
8	**Phenols**														
8 a	Ferric chloride	-	+	+	+	+	+	+	-	-	+	-	-	+	+
8 b	Lead acetate	-	-	-	-	-	-	-	-	-	-	-	-	-	-
9	**Quinones**	-	-	-	-	-	-	-	-	-	-	-	-	-	-
10	**Carbohydrates**														
10 a	Molisch's	+	+	-	+	+	+	+	-	-	-	+	-	+	+
10 b	Fehling's	+	-	-	-	-		+	-	+	+	-	+	-	-
11	**Saponins**														
11 a	Froth test	-	-	-	-	-	-	+	-	-	-	-	-	-	-
11 b	Foam test	-	-	-	-	-	-	+	-	-	-	-	-	-	-

+ Present; - Absent

The present study confirms the presence of alkaloids, flavonoids, sterols, terpenoids, anthraquinones, proteins, phenols, carbohydrates, and saponins in *Cyperus rotundus* tuber. The leaves of *Hemigraphis alternata* confirm the presence of alkaloids, flavonoids, sterols, terpenoids, anthocyanins, proteins, phenols, and carbohydrates.

The order of number of phytoconstituents present in the solvent extracts are given below.

***Cyperus rotundus* tuber** **: W > C > E > A, EA > PE >CF**

***Hemigraphis alternata* leaves** **: CF, C, E, W > A > PE > EA**

The aqueous extract of both plant samples contains more phytoconstituents than other solvent extracts. *Cyperus rotundus* aqueous extract contains alkaloids, flavonoids, protein, phenols, carbohydrates, and saponins. *Hemigraphis alternata* aqueous extract contains alkaloids, flavonoid, sterols, proteins, phenols, and carbohydrates. Water is a commonly used solvent for many extractions process due to its high dielectric constant **(Sharp, 2001)**, polar nature, neutral behaviour (pH = 7), health, and environmental concerns **(Santhiya and Lalitha, 2019)**. In this regard, the aqueous extracts of selected samples were used throughout the study. *Cyperus rotundus* aqueous extract contains more phyto constituents than *Hemigraphis alternata*. These phytochemicals were used as a capping and reducing agent to synthesize nanoparticle and are involved in different biological activities and cosmetic applications mentioned in this study.

Figure 5. Photographs of phyto-chemical assessment of CR and HA solvents extracts

4.2 Synthesis of gold nanoparticles using aqueous extract of CR, HA, and PS

A vast number of chemical and biological methods are available to synthesize gold nanoparticles. Due to the need of more economical methods and less-time consuming methods, the search for different synthesis is at the forefront. In this study, room temperature, sunlight irradiation, sonication, and microwave oven heating were employed to synthesis gold nanoparticles. Based on its results, methods were preliminary screened based on the formation of gold nanoparticles in short time, and which were used throughout nanoparticle synthesis. The gold chloride concentration was kept uniform in a ratio in preliminary screening due to gold chloride's cost and environmental concerns. The formation of gold nanoparticles was initially confirmed with colour change and UV analysis.

4.2.1 Synthesis of gold nanoparticles at Room temperature

Room temperature is a simple and convenient method for the synthesis of gold nanoparticles. The ratio of CRablank, HAablank, and PSablank was mixed with an equal ratio of gold chloride at room temperature (28-35ºC). After mixing the reactants, the container was kept at room temperature, and colour changes were observed visually. Greyish pink, violet, and bluish grey-coloured gold nanoparticles was formed using CRablank, HAablank, and PSablank respectively (given in **Table 11**). With the increase in the concentration of CRablank and HAablank (**Figure 6a**), the time of nano formation decreases. Gold nanoparticle formation using PSablank (**Figure 6b**) was noted after five days at room temperature for all concentrations. Gold nanoparticles using HAablank was formed with a short time (5-20 seconds) compared to CRablank (10-15 min). This may be due to the presence of more sterols (discussed in 4.1) and the other phytoconstituents present in the HAablank.

Table 11. Synthesis of gold nanoparticles using CRablank, HAablank and PSablank at Room temperature method

Concentration ratio ($HAuCl_4$: Sample)	Time taken for gold nano synthesis					
	CRaNP (min)	Colour of CRaNP	HAaNP (sec)	Colour of HAaNP	PSaNP (day)	Colour of PSaNP
1:1	15	Greyish pink	20	Violet	5	Bluish grey
1:2	13		10			
1:3	13		7			
1:4	12		5			
1:5	10		5			

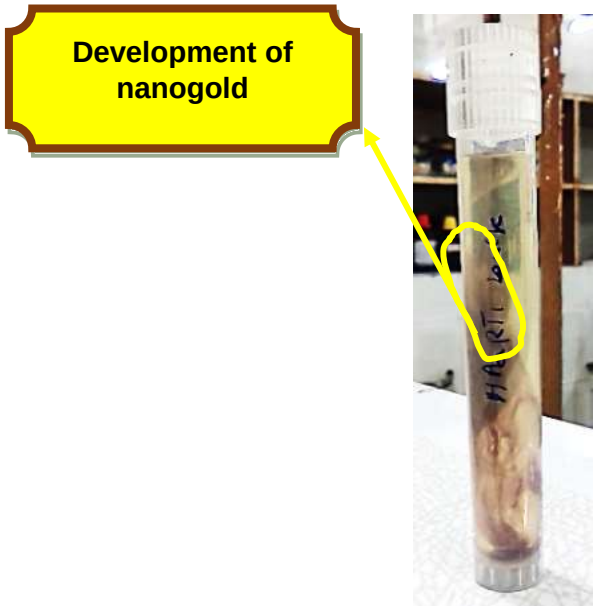

Figure 6a. Photograph of HAaNP

Figure 6b. Photograph of PSaNP

Figure 6a and b. Photographs of synthesized gold nanoparticles at Room temperature

4.2.2 Synthesis of gold nanoparticles by Sonication

Sonication is a facial versatile and conventional method **(Bang and Kenneth, 2010)** that brings serious benefits such as compatibility, cost efficiency, environmental friendliness **(Sillanpaa *et al*., 2011)**, reliable option, and controllable measure to synthesize nanoparticles **(Malik *et al*., 2014)**. It enhances the reactivity of metal surfaces. The high-intensity irradiation passes through the liquid causing acoustic cavitation to

occur near the solid surface, creating localized erosion, which includes high velocity inter collision. This causes fragments and improves mass transport **(Suslick *et al*., 1989)**. No need for an additional heater for temperature studies and magnetic stirrer under atmospheric conditions to examine the possibility of product formation. This method has been employed to reduce the accumulation of fine nanoparticles.

Gold nanoparticles formed by treating gold chloride with CRablank, HAablank, and PSablank (**Table 12)**. CRablank forms greyish pink colour gold nanoparticles within 60 seconds in the ratio of 1:5. Violet colour gold nanoparticles obtained within 5 seconds using HAablank (**Figure 7a and 7b**). The bluish grey gold nanoparticle using PSablank was obtained within 90 min under sonication.

Table 12. Synthesis of gold nanoparticles using CRablank, HAablank and PSablank by Sonication

Concentration ratio ($HAuCl_4$: Sample)	Time taken for gold nanoparticle synthesis					
	CRaNP (min)	Colour of CRaNP	HAaNP (sec)	Colour of HAaNP	PSaNP (min)	Colour of PSaNP
1:1	1	Greyish pink	50	Violet	90	Bluish grey
1:2	1.40		30			
1:3	1.35		15			
1:4	1.30		10			
1:5	1		5			

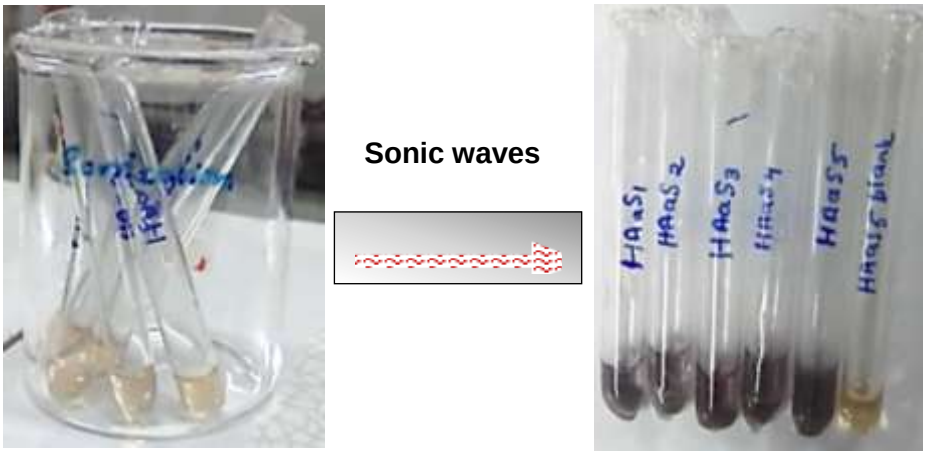

Figure 7a. Photograph of HAablank

Figure 7b. Photograph of HAaNP

Figure 7a and b. Photographs of synthesis of gold nanoparticles by Sonication method

4.2.3 Synthesis of gold nanoparticles under Sunlight irradiation

Sunlight emits electromagnetic radiation with different wavelengths, and it is enhancing the activation of reactant species. Sunlight induces the formation of the nanoparticles in short time and forms more stable particles than room temperature **(Bipin and Arti, 2020)**. Greyish pink, violet, and pink colour gold nanoparticles formed using CRablank, HAablank, and PSablank respectively, under sunlight (**Table 13**). CRaNP formed within 50 seconds in a 1:5 ratio, and HAaNP (**Figure 8a**) showed in 3 seconds in a higher concentration of HAablank (1:5). PSaNP formed in 35 min at 1:1 ratio. With increase in the concentration of plant extracts, the reduction time of gold ions decreases, but in PSaNP (**Figure 8b**), the time of nanoparticles formation increases by increases in PSablank ratio.

Table 13. Synthesis of gold nanoparticles using CRablank, HAablank and PSablank under Sunlight irradiation

Concentration ratio ($HAuCl_4$: Sample)	Time taken for gold nanoparticle synthesis					
	CRaNP (min)	Colour of CRaNP	HAaNP (sec)	Colour of HAaNP	PSaNP (min)	Colour of PSaNP
1:1	2.30	Greyish pink	20	Violet	35	Pink
1:2	2		10		50	
1:3	1		8		90	
1:4	1		6		135	
1:5	0.50		3		135	

Figure 8a. Photograph of HAaNP

Figure 8b. Photograph of PSaNP

Figure 8a and b. Photographs of synthesized gold nanoparticles under Sunlight

4.2.4 Synthesis of gold nanoparticles by Microwave heating

Microwave synthesis is an alternative methodology that helps to synthesize nanoparticles with short time and well size distribution. The reaction occurs by interacting microwave radiation with the reaction mixture by increasing the temperature above their boiling point **(Wing *et al*., 2012)**. Equal concentration of $HAuCl_4$ treated with different concentration of CRablank, HAablank, and PSablank and then it was microwaved. Within 5 sec, greyish pink-coloured gold nanoparticles formed using CRablank, and violet colour HAaNP formed in 3 sec. The brown colour changes was noted using PSablank at 1:1 and 1:2 ratio, and the violet colour was observed in 1:3 to 1:5 ratios (**Table 14**).

Table 14. Synthesis of gold nanoparticles using CRablank, HAablank and PSablank by Microwave heating

Concentration ratio ($HAuCl_4$: Sample)	Time taken for gold nanoparticle synthesis					
	CRaNP (sec)	Colour of CRaNP	HAaNP (sec)	Colour of HAaNP	PSaNP (min)	Colour of PSaNP
1:1	30	Greyish pink	20	Violet	6	Brown
1:2	20		10		4.30	
1:3	15		4		3.30	Violet
1:4	10		3		2	
1:5	5		3		1.30	

4.3 Results of concentration variation study of gold nanoparticles synthesis

Based on 4.2, the concentration variation study was carried out for CRablank by microwave heating, HAablank at room temperature conditions, and PSablank under sunlight irradiation to optimize the formation of gold nanoparticles. The results of the concentration variation study are given below.

4.3.1 Room temperature method

The HAaNP was synthesized using different methods (mentioned in 4.2). The room temperature method shows no significant time difference than a microwave (3 sec), sonication (5 sec) and sunlight (5 sec) method. In room temperature condition, gold nanoparticles were formed within 5 sec at a 1:1 and 1:5 ratio. The colour changes from yellowish-brown to violet due to the increases in the ratio of HAablank and the equal ratio of $HAuCl_4$. The time of nano formation decreases with an increase in extract concentration. With the increase in the ratio of $HAuCl_4$, the time of nano formation

increased and the colour of the gold nanoparticle varied from violet (1:1) to ash blue (2:1 to 5:1) (**Table 15**). The ash blue colour changes due to the agglomeration of the nanoparticles which leads to an increase in size and time of nano formation. For this colour change may be due to the flocculation (**Stojilijkovic *et al*., 2016)**.

Table 15. Concentration variation studies of synthesized gold nanoparticles by varying the concentration of gold chloride and HAablank at Room temperature

Concentration ratio ($HAuCl_4$: HAablank)	Time taken for synthesis HAaNP (Sec)	Colour of HAaNP	Concentration ratio ($HAuCl_4$: HAablank)	Time taken for synthesis HAaNP (sec)	Colour of HAaNP
1:1	20	Violet	1:1	5	Violet
1:2	10		2:1	15	Ash blue
1:3	7		3:1	50	
1:4	5		4:1	120	
1:5	5		5:1	140	

4.3.2 Sunlight irradiation method

The concentration variation studies of PSaNP were carried out using varying the ratio of $HAuCl_4$ and PSablank under sunlight irradiation (**Table 16**). With increase in the ratio of PSablank, the pink-coloured gold nanoparticles formed within 35 to 135 minutes. The bluish-grey colour gold nanoparticles were observed in 25 to 70 minutes by increasing the ratio of $HAuCl_4$. PSaNP formed in a short time by treating an equal ratio of gold chloride and PSablank (1:1). The changes in nanoparticle colour strongly depend on the concentration of the reactant and reaction time. Higher aggregation of gold ions in the mixture resulting in the formation of bluish-grey coloured PSaNP (**Figure 9b**). The lesser aggregation was observed in a decrease in the $HAuCl_4$ ratio and increase PSablank resulting the pink colour gold nanoparticles were formed.

Gold nanoparticle synthesis under sunlight is a mild and a gradual heating process **(Chien *et al*., 2011)** and it helps to transfer electrons from the capping agent present in the pumice stone to the gold ion. Different wavelengths of sunlight activate the reduction of gold ion into gold nanoparticles. The higher content of calcium present in PSablank (**Figure 9a**) may be involves in the reduction of gold ions.

Table 16. Concentration variation studies of synthesized gold nanoparticles by varying the concentration of gold chloride and PSablank under Sunlight irradiation

Concentration ratio ($HAuCl_4$: Psablank)	Time taken for synthesis PSaNP (min)	Colour of PSaNP	Concentration ratio ($HAuCl_4$: PSablank)	Time taken for synthesis PSaNP (min)	Colour of PSaNP
1:1	35	Pink	1:1	25	Bluish grey
1:2	50		2:1	35	
1:3	90		3:1	50	
1:4	135		4:1	60	
1:5	135		5:1	70	

Figure 9a. Photograph of PSablank

Figure 9b. Photograph of PSaNP

Figure 9a and b. Photographs of synthesis of gold nanoparticles under Sunlight irradiation

4.3.3 Microwave heating method

The formation of CRaNP (**Figure 10**) was observed in room temperature, sunlight, sonication, and microwave heating synthesis at different time intervals were mentioned in 4.2. Similar colour (greyish pink) change was noticed in all methods (**Table 17**). Comparing the different methods, the microwave heating method produces nanoparticles in a short time without agglomeration due to its higher heating rate and uniform heat distribution. Microwaves penetrate fast and uniform through the mixture and helps produce narrowly dispersed gold nanoparticles **(Ngo *et al*., 2016)**. Based on the optimization study, the time of nano formation decreased with increase CRablank ratio and time of nano formation increased with increasing the ratio of $HAuCl_4$. The donation of an electron from capping agents in CRablank to gold ions resulting in CRaNP nanoparticles.

Table 17. Concentration variation studies of synthesized gold nanoparticles by varying the concentration of gold chloride and CRablank by Microwave heating

Concentration ratio ($HAuCl_4$: CRablank)	Time taken for synthesis CRaNP (Sec)	Colour of CRaNP	Concentration ratio ($HAuCl_4$: CRablank)	Time taken for synthesis CRaNP (sec)	Colour of CRaNP
1:1	30	Greyish pink	1:1	10	Greyish pink
1:2	20		2:1	15	
1:3	15		3:1	25	
1:4	10		4:1	35	
1:5	5		5:1	40	

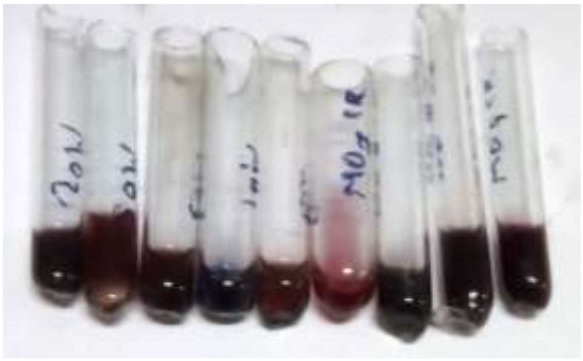

Figure 10. Photograph of synthesized gold nanoparticles using CRablank by Microwave heating method

4.4 Stability and mechanism of gold nanoparticle formation

The secondary metabolites present in the aqueous extract of *Cyperus rotundus* tuber and *Hemigraphis alternata* leaves were confirmed by the colour test (given in 4.1). The available phytoconstituents present in the extract facilitate the formation of gold nanoparticles and act as a capping and stabilizing agent. The stability of prepared gold nanoparticles in colloidal form was monitored visually. There is no microbial growth was observed in PSaNP for two years in both cooling and room temperature. In 6-12 months, microbial growth and accumulation have not occurred in plant aided nanoparticles in room temperature and cooling condition. The dried forms of all the prepared gold nanoparticles were stable for more than three years.

The plant extracts contain several important phytoconstituents such as alkaloids, flavonoids, phenols, terpenoids, protein, carbohydrates, *etc*. **(Jenny *et al*., 1999; Saikat *et al*., 2002; Singh *et al*., 2010; Sukirtha *et al*., 2012; Shubhangini and Cherian, 2013; Yasmin *et al*., 2014; Makarov *et al*., 2014; Adavallan and Krishnakumar, 2014;**

Saware *et al*., 2014; Choudhary *et al*., 2017). The formation of gold nanoparticles is involved by treating $HAuCl_4$ with reducing agent under various conditions. Initially, the reducing agents and $HAuCl_4$ form a complex by functional groups of phytoconstituents with gold ions **(Laure Morel *et al*., 2017)**. Electrons from the phytoconstituents are strongly attached on the metal surface and reduced Au^{3+} ion into Au^0 nanoparticles **(Choudhary *et al*., 2017)**. Structural internal conversion of secondary metabolites releases the reactive hydrogen atoms and reduces the metal ions resulting in gold nanoparticles **(Makarov *et al*., 2014)**. The presence of phytoconstituents mentioned in 4.1, which are involved in reducing gold ions and the suggested mechanism of plant embed gold nanoparticles is given in **Figure 11**.

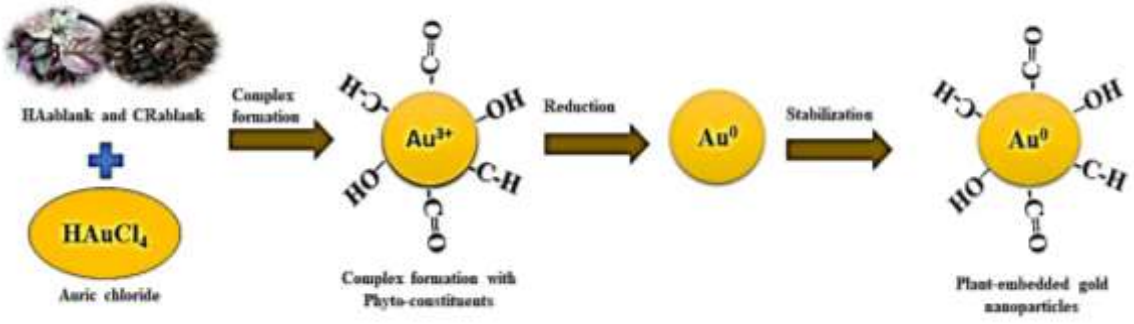

Figure 11. Pictorial representation of mechanism of gold nanoparticles synthesis

The chemical composition of pumice stone contains oxides of K, Na, Ca, Fe, Mg, Mn, Ti and S **(Tunc and Duman, 2009; Ersoy *et al*., 2010)**. In the present study, the EDS analysis of PSablank confirms the presence higher amount of Ca than other metals (O, Na, Ca, Mg, Al and Ti) and the composites may be present in oxide form. Hydroxides (-OH) and oxygen bridges are available on pumice stone surfaces, which are involved in adsorption activity **(Deniz and Sureyya, 2015)**. **Macchione *et al*., 2018** mentioned the formation of gold nanoparticles in wet media of silica surfaces by decomposing gold hydroxide. Based on the mechanism of **Macchione *et al*., 2018**, the following mechanism is derived and mentioned in **Equation 7-9**. The first step of gold nano formation involves converting CaO into $Ca(OH)_2$ during the preparation of PSablank (**Equation 7**). The donation of hydroxide ions (-OH) from $Ca(OH)_2$ form the $[Au(OH)_4]^-$ complex on defect sites with $AuCl_4$ (**Equation 8**). Then the complex decomposed into gold nanoparticles due to the unstable nature of $[Au(OH)_4]^-$ complex (**Equation 9**).

$2CaO + 2H_2O \longrightarrow 2Ca(OH)_2$ **(Equation 7)**

$AuCl_4 + 4OH^- \longrightarrow [Au(OH)_4]^- + 4Cl^-$ **(Equation 8)**

$3[Au(OH)_4]^- \longrightarrow 3\,Au_{(Nanoparticle)} + 3O_2 + 6H_2O$ **(Equation 9)**

4.5 Results of synthesized rGO and AuNPs-rGO composite

Reduced graphene oxide and the composite of gold nanoparticles-reduced graphene oxide was synthesized using aqueous extract of *Cyperus rotundus* and *Hemigraphis alternata* (**Table 18**). The black coloured CRarGO (**Figure 12a**) and HAarGO (**Figure 12b**) was obtained by refluxing method. The nanocomposite of CRaNP–CRarGO and HAaNP-HAarGO represented as CRaNC and HAaNC, respectively. CRaNC and HAaNC prepared by treating equal ratio of AuNPs and rGO under sonication followed by homogenization. Blackish pink coloured CRaNC (**Figure 12c**) and blackish violet coloured HAaNC (**Figure 12d**) were obtained.

Table 18. Details of synthesized rGO and AuNPs-rGO composite

S. No	Plant samples	Solvent extract	rGO/ Composite	Sample code	Method	Synthesis time (h)	Colour changes
1	CR	Aqueous extract	rGO	CRarGO	Refluxing	2	Brown to black
			Composite	CRaNC	Sonication + Homogenization	1+1	Blackish pink
2	HA		rGO	HAarGO	Refluxing	10	Brown to black
			Composite	HAaNC	Sonication + Homogenization	1+1	Blackish violet

Figure 12a. CRarGO **Figure 12b. HAarGO** **Figure 12c. CRaNC** **Figure 12d. HAaNC**

Figure 12a-d. Photographs of synthesized rGO and rGO-AuNPs composite

4.6 Characterization of synthesized AuNPs, rGO, and AuNPs-rGO composite using spectroscopic analysis

Synthesized AuNPs, rGO and AuNPs-rGO composite was characterized by UV-Visible, FTIR, XRD, FESEM and EDS analysis. Raman and TGA analysis was taken for prepared rGO samples. The sonication provides complete dispersion of the sample without any agglomeration leads the better results. Initially, all the prepared samples sonicated well before taken for the analysis.

4.6.1 UV-Visible spectroscopy analysis of synthesized nanoparticles

4.6.1.1 UV-Visible spectrum of synthesized CRaNP, HAaNP and PSaNP

The formation of gold nanoparticles confirmed in UV-Visible region by the coloured samples which allowed to measure the absorbance against distinct wavelengths. The formation of SPR bands by electron oscillation due to the interaction of free conducting electrons and the electromagnetic field **(Smitha *et al*., 2009)**. The formation of gold nanoparticles was initially confirmed by colour change. The SPR band at 530-550 nm (**Figure 13a**), 550 nm (**Figure 13b**) and 450 nm (**Figure 13c**) confirms the formation of CRaNP, HAaNP and PSaNP respectively.

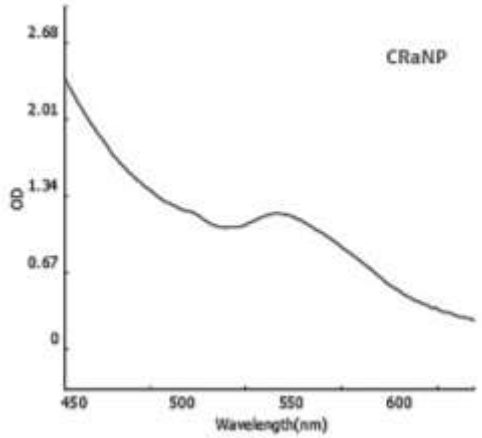

Figure 13a. UV-Visible spectrum of CRaNP

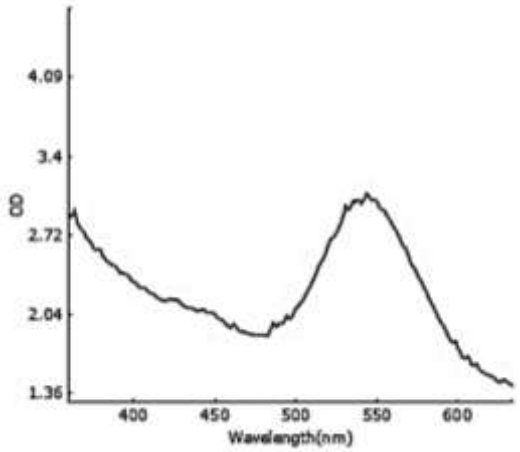

Figure 13b. UV-Visible spectrum of HAaNP

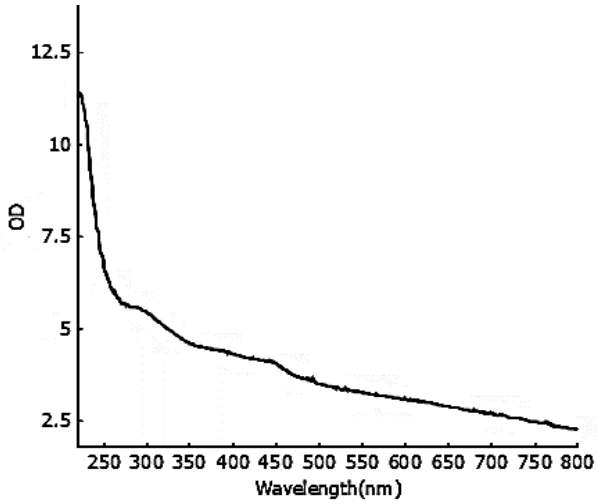

Figure 13c. UV-Visible spectrum of PSaNP

Figure 13a-c. UV-Visible spectrum of synthesized gold nanoparticles a) CRaNP by microwave heating, b) HAaNP at room temperature and c) PSaNP under sunlight

4.6.1.2 UV-Visible spectrum of synthesized CRarGO and HAarGO

The prepared CRarGO and HAarGO strongly dispersed using sonication and homogenization for 10 minutes. The aqueous dispersed GO showed the SPR band at 234 nm. This band observed due to the π→π* transition of aromatic C=C group in graphene oxide. The UV-Visible spectrum of CRarGO (**Figure 14a**) showed band at 274 nm, and HAarGO (**Figure 14b**) showed at 264 nm. The band shift from 234 nm to 274 nm

(CRarGO), 264 nm (HAarGO) and shift in carbonyl group confirm the reduction of GO into rGO due to the n→π* transition in C=O bond.

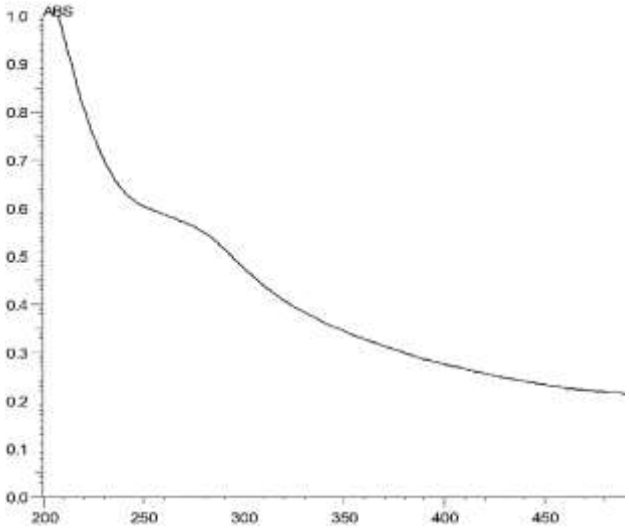

Figure 14a. UV-Visible spectrum of CRarGO

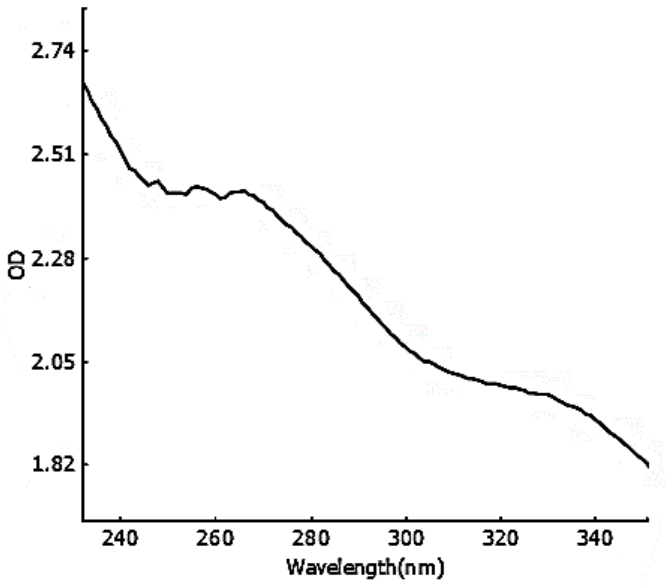

Figure 14b. UV-Visible spectrum of HAarGO

Figure 14a and b. UV-Visible spectrum of synthesized reduced graphene oxides

4.6.1.3 UV-Visible spectrum of synthesized CRaNC and HAaNC

The UV-Visible spectrum of CRaNC (**Figure 15a**) and HAaNC (**Figure 15b**) shows two desired peaks between 250-300 nm and 500-600 nm respectively. This result

shows the presence of both CRaNP and CRarGO in CRaNC and HAaNP and HAarGO in HAaNC.

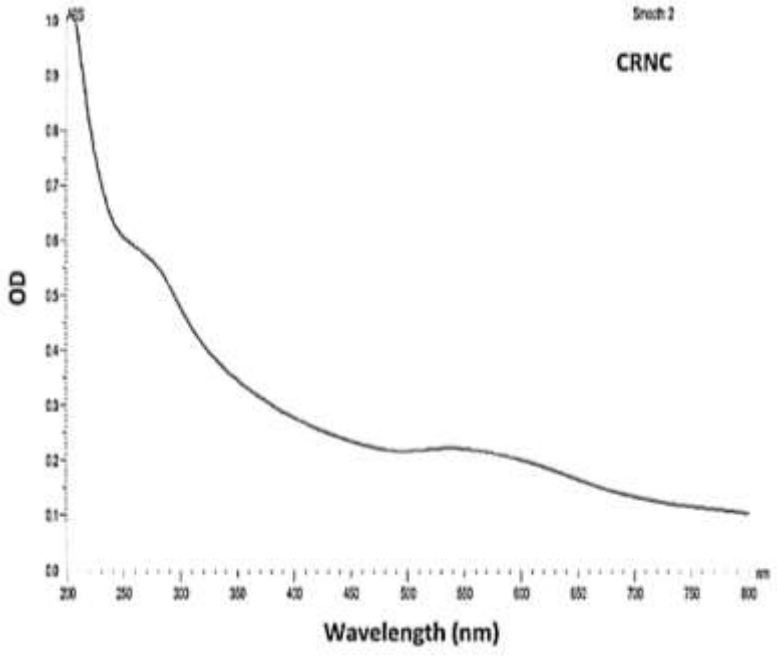

Figure 15a. UV-Visible spectrum of CRaNC

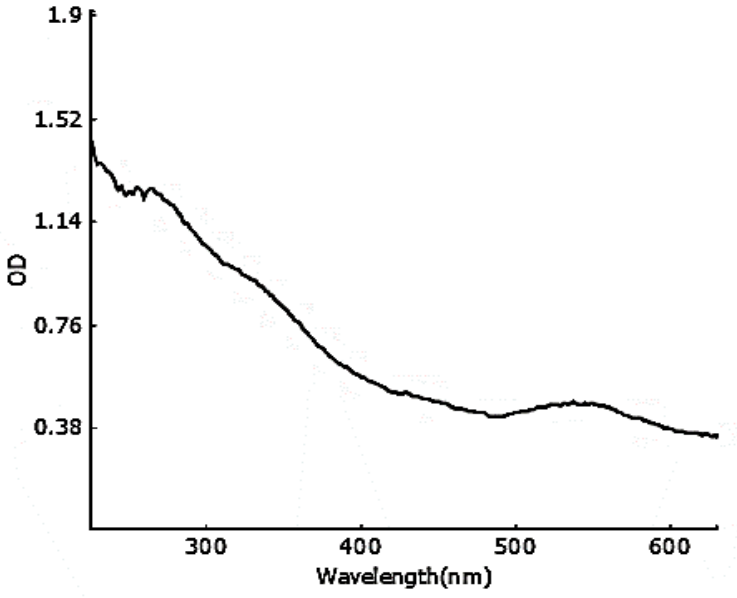

Figure 15b. UV-Visible spectrum of HAaNC

Figure 15a and b. UV-Visible spectrum of synthesized gold nanoparticle-reduced graphene oxide nanocomposites

4.6.2 FTIR spectroscopy analysis of synthesized nanoparticles

4.6.2.1 FTIR spectrum of synthesized CRaNP, HAaNP and PSaNP

FTIR spectrum of CRaNP showed the bands at 3356.14, 2113.98 and 1635.64 cm^{-1} due to –OH, carbonyl group and C=N group respectively (**Figure 16a**). Similarly, 3429.43, 1651.07 and 1450.47 cm^{-1} bands attributed to –OH, -C=O and -C-H for HAaNP respectively (**Figure 16b**). PSaNP showed (**Figure 16c**) bands at 3849.92, 3718.76, 3595.31, 1720.50, 1519.91, 1226.73 and 671.23 cm^{-1} due to the stretching vibrations in metal hydroxides, carbonyl group (C=O) and stretching vibrations in N-O, C-N and C-Cl groups.

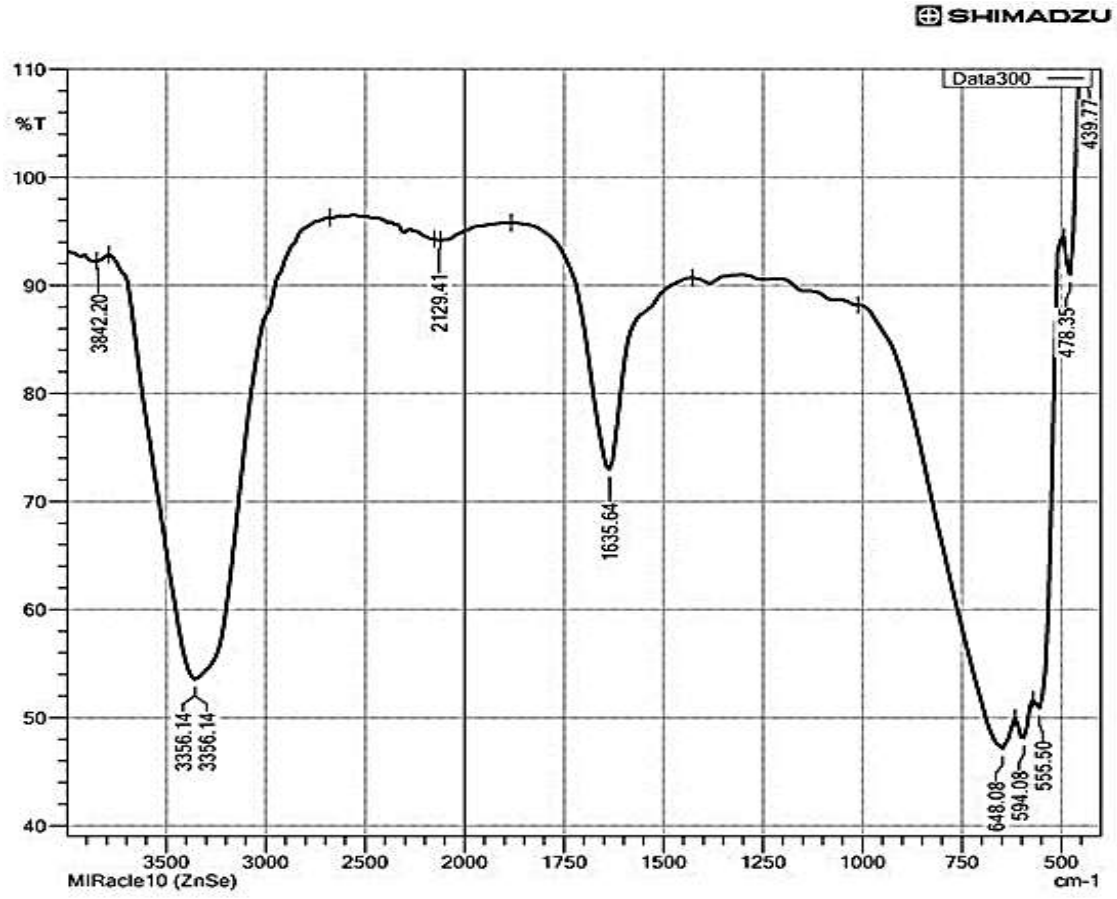

Figure 16a. FTIR spectrum of CRaNP

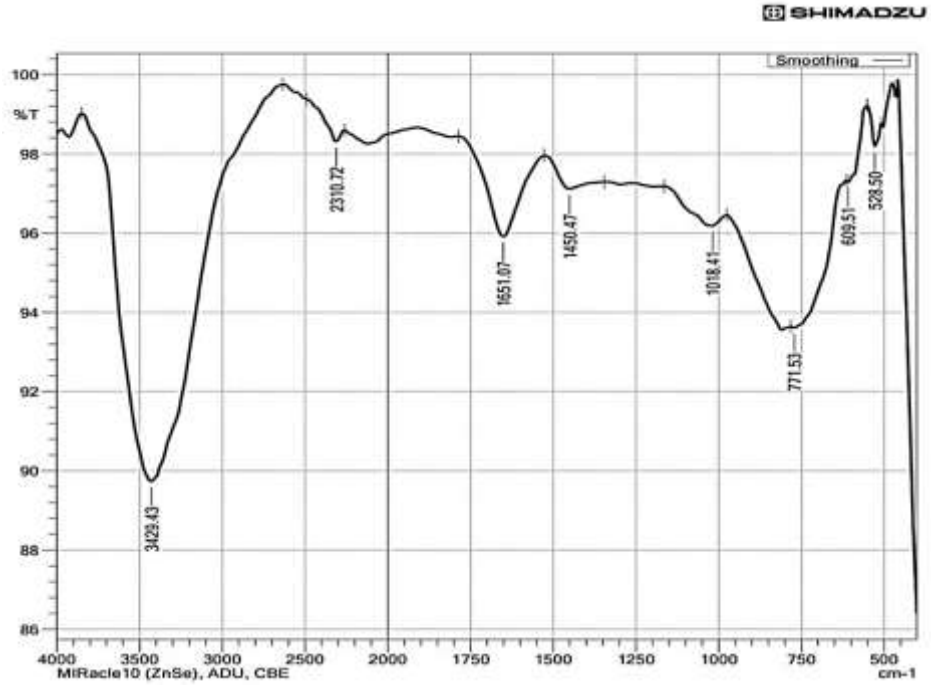

Figure 16b. FTIR spectrum of HAaNP

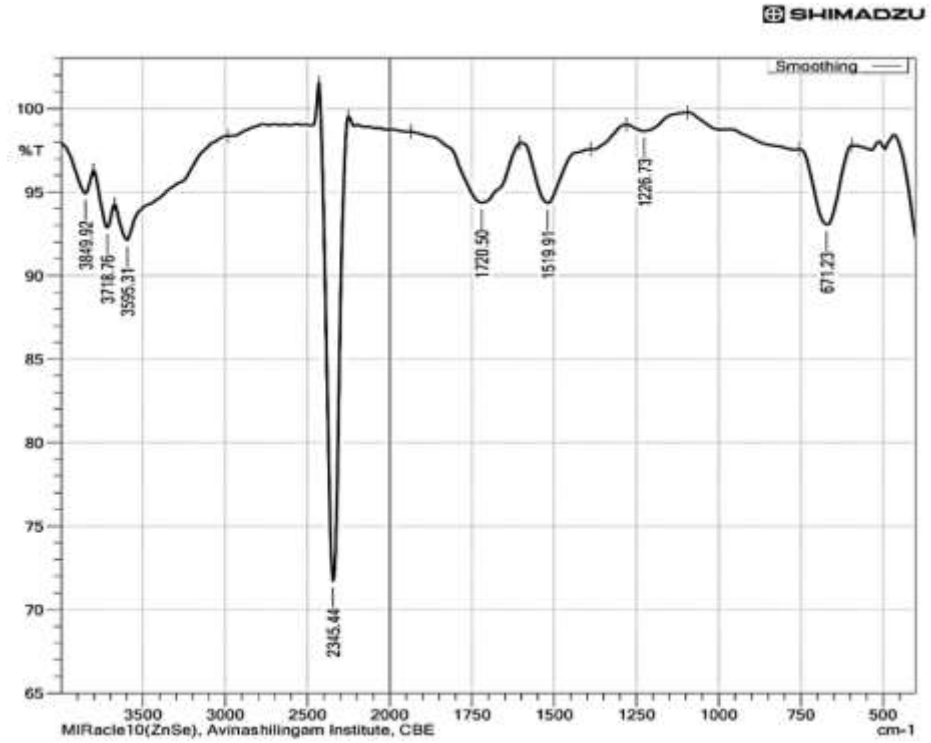

Figure 16c. FTIR spectrum of PSaNP

Figure 16a-c. FTIR spectrum of synthesized gold nanoparticles a) CRaNP by microwave heating, b) HAaNP at room temperature and c) PSaNP under sunlight

4.6.2.2 FTIR spectrum of synthesized CRarGO and HAarGO

CRarGO showed strong bands at 3275, 2916.37, 1622.13, 1371.39 cm^{-1} are due to -OH stretching vibration, -CH stretching which indicates the presence of alkanes, C=N bending vibrations, and C-H bending vibrations respectively. The peak at 1020.34 cm^{-1} indicates due to presence of carbon and oxygen bond in CRarGO. HAarGO showed bands at 3734.19, 1743.65, 1651.07, and 1219.01 cm^{-1} due to the presence of terminal –OH group, –C=O stretching vibration, -C=N and –C-O stretching of COOH group respectively. GO showed the peaks at 3199.31 cm^{-1} due to –OH stretching vibration, 1705.07 cm^{-1} due to -C=O group, 1031.92 cm^{-1} due to -C-O, 1589.34 cm^{-1} are due to -C-C and 856.39 cm^{-1} attributed to –C=N. The shift of carbonyl group in CRarGO (**Figure 17a**) and HAarGO (**Figure 17b**) confirms the reduction of GO.

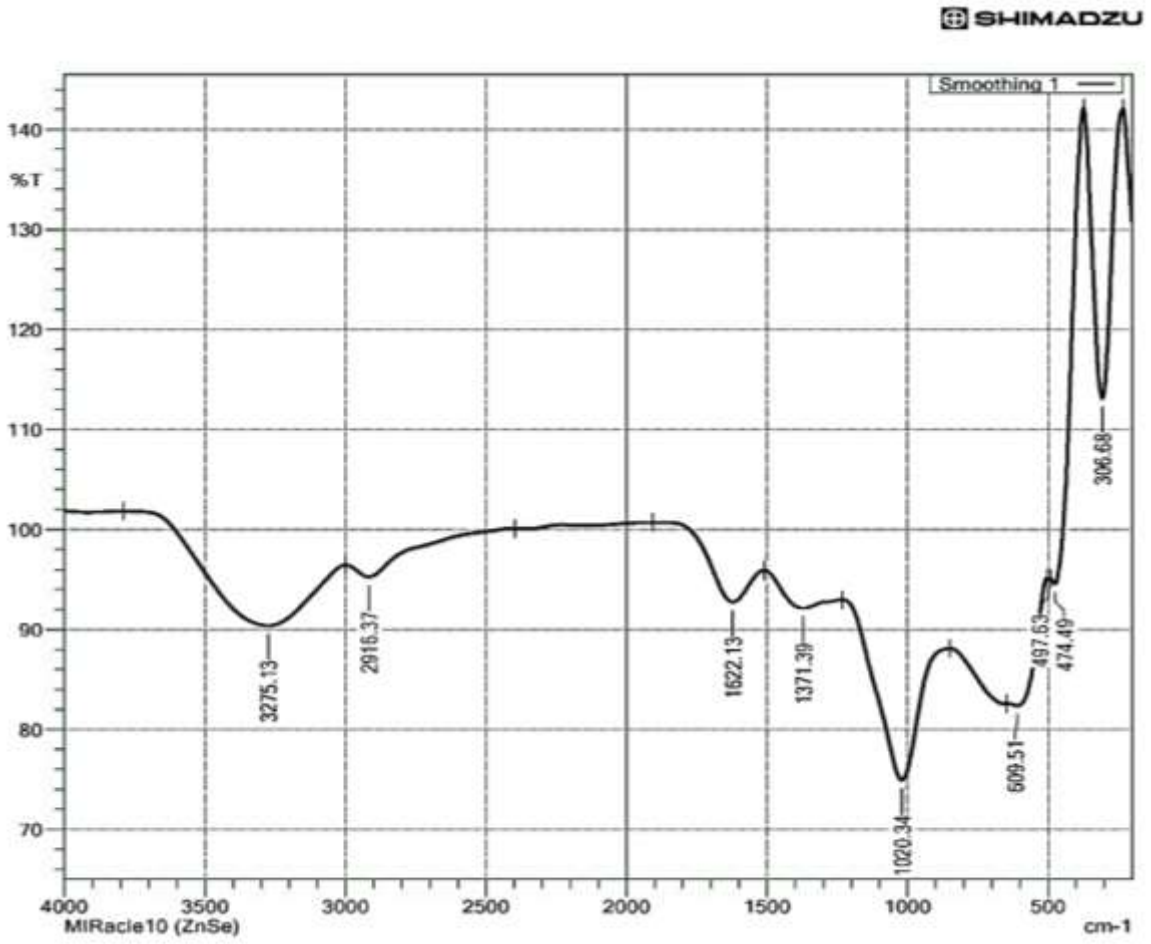

Figure 17a. FTIR spectrum of CRarGO

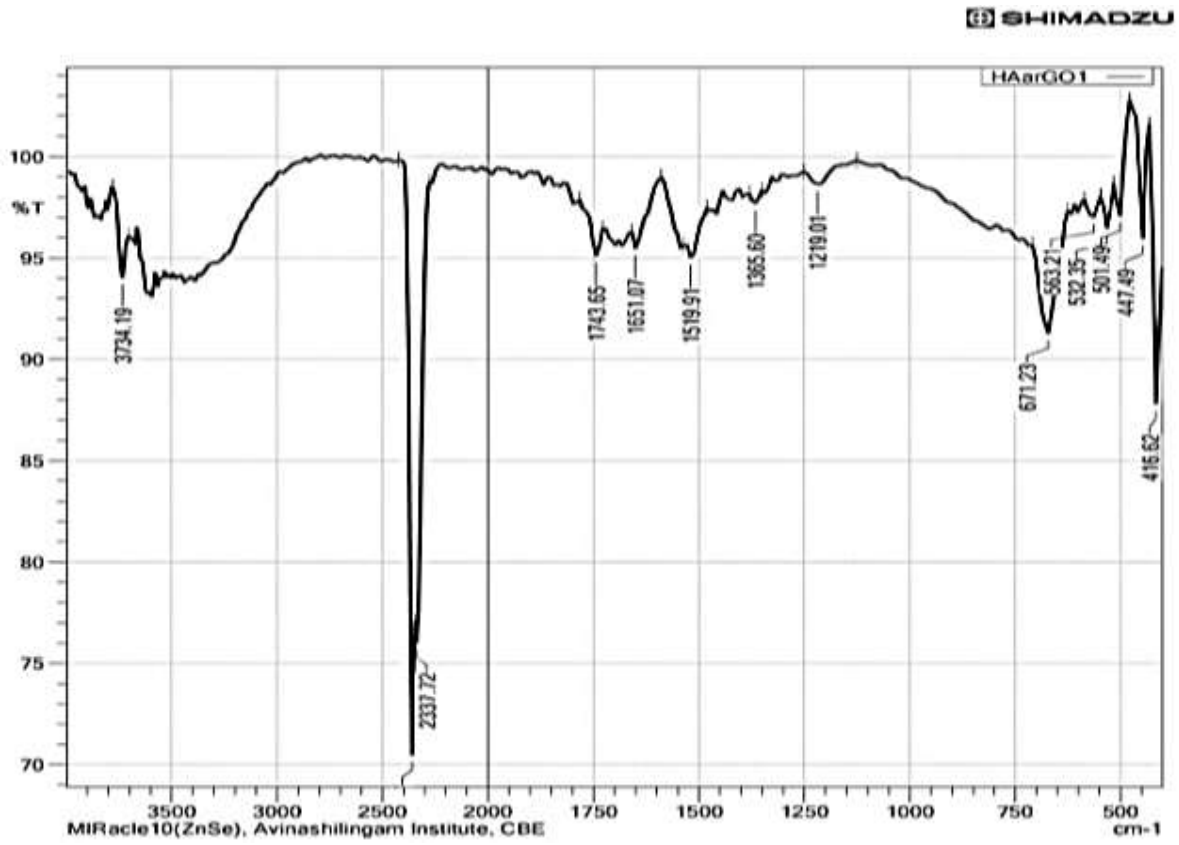

Figure 17b. FTIR spectrum of HAarGO

Figure 17a and b. FTIR spectrum of synthesized reduced graphene oxides

4.6.2.3 FTIR spectrum of synthesized CRaNC and HAaNC

The FTIR spectrum of CRaNC showed peaks at 3356.14, 1631.78 and 655.80 cm^{-1} (**Figure 18a**). HAaNC (**Figure 18b**) showed 3363.86 cm^{-1} due to phenolic –OH, 1635.64 cm^{-1} due to -C=C-,1002.98 cm^{-1} due to C-O, 671.23 cm^{-1} due to C-H and 601.79 cm^{-1} due to C-Cl.

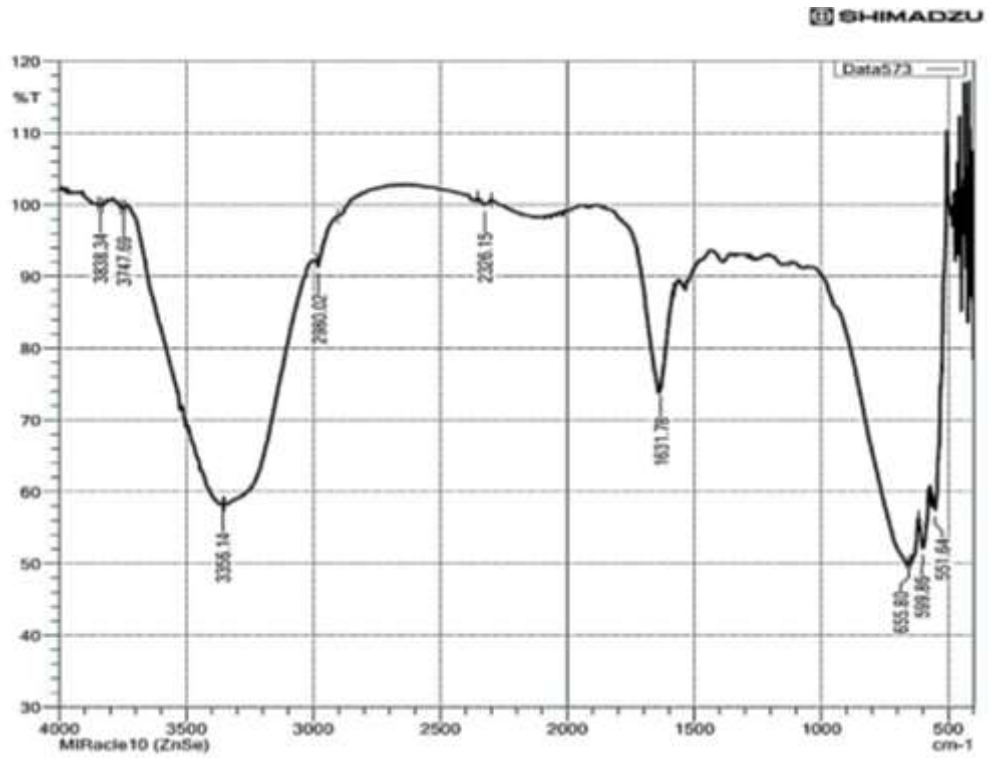

Figure 18a. FTIR spectrum of CRaNC

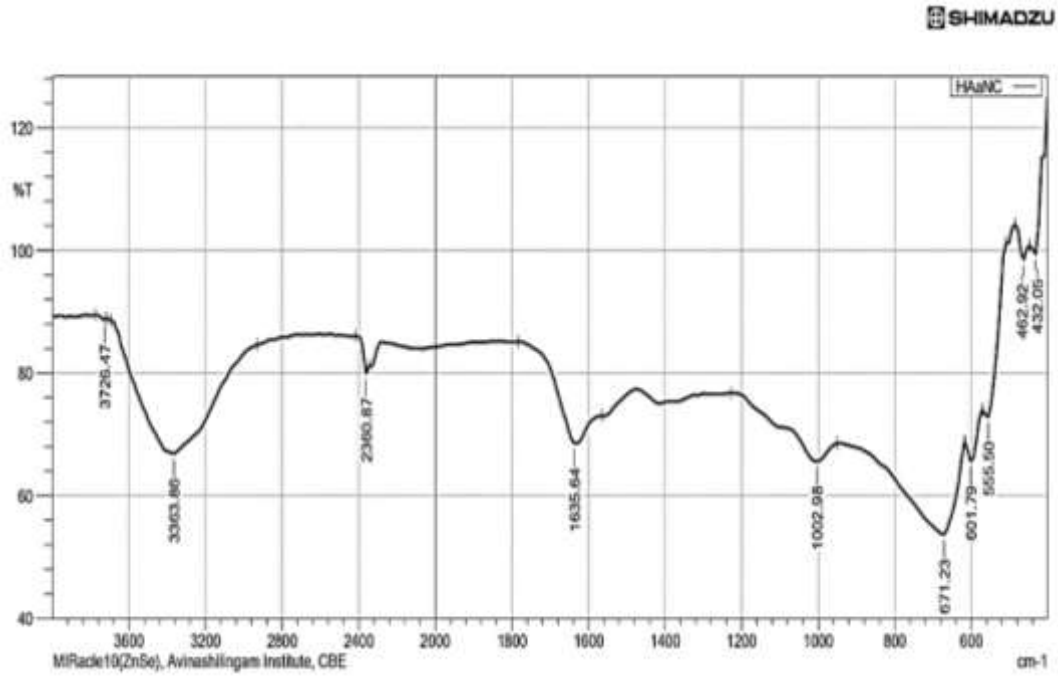

Figure 18b. FTIR spectrum of HAaNC

Figure 18a and b. FTIR spectrum of synthesized gold nanoparticle-reduced graphene oxide nanocomposites

4.6.3 X-Ray diffraction spectroscopy analysis of prepared nanoparticles

4.6.3.1 XRD spectrum of CRaNP, HAaNP and PSaNP

The XRD spectrum of CRaNP, HAaNP, and PSaNP are given in **Figures 19a to 19c**. The 2θ values 44.6308° and 38.4445° are obtained for CRaNP and PSaNP with interspacing of 2.0 Å and 2.34 Å respectively. The 2θ values for HAaNP are 38.4° and 44.6° with d-spacing 2.3 and 2.0 Å respectively. The average size 10 nm, 22 nm, and 11 nm were obtained for CRaNP, HAaNP, and PSaNP respectively. The particle size of the gold nanoparticles was calculated using Scherrer's equation. The XRD spectrum indicates the formation and crystalline nature of prepared gold nanoparticles and the peak details are given in **Table 19**.

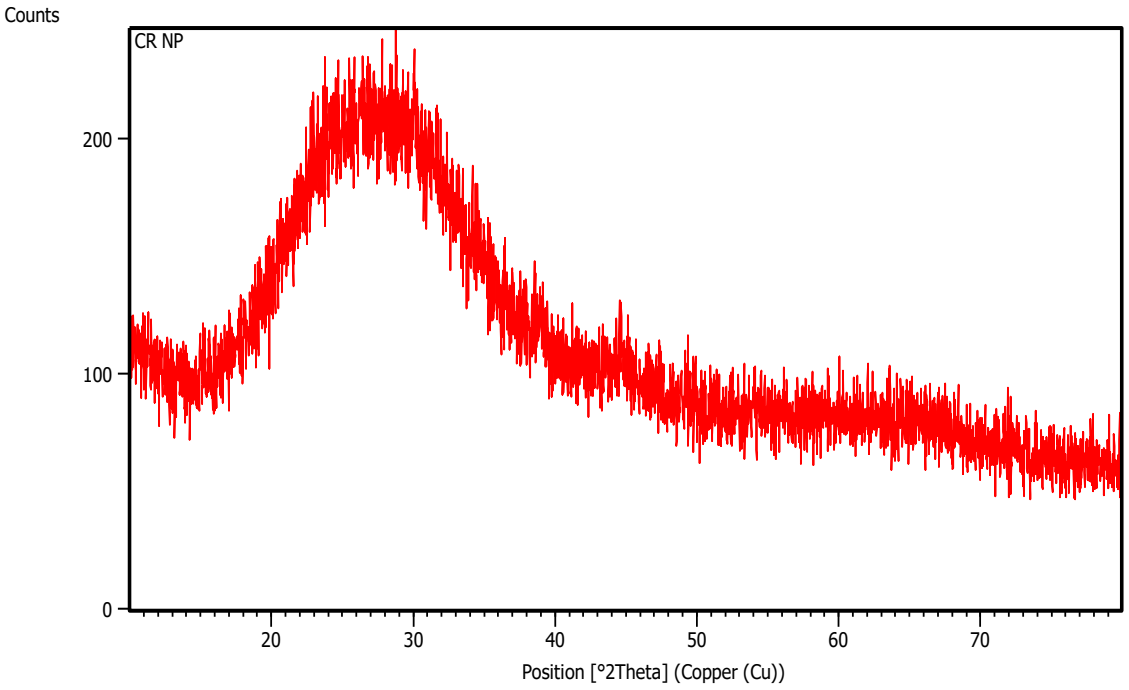

Figure 19a. XRD spectrum of CRaNP

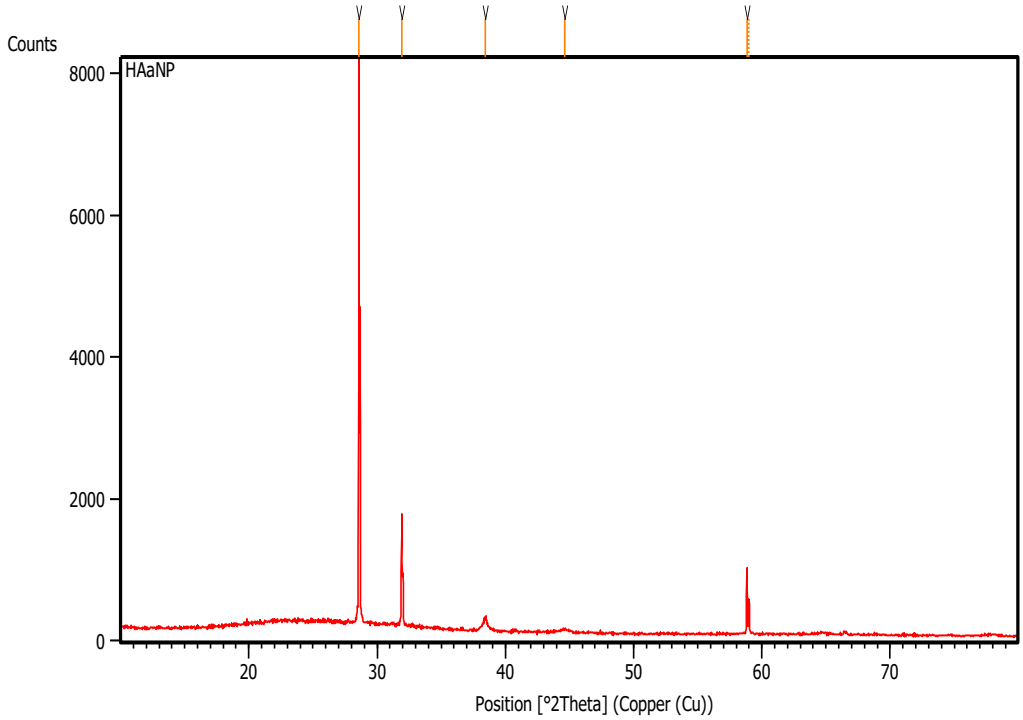

Figure 19b. XRD spectrum of HAaNP

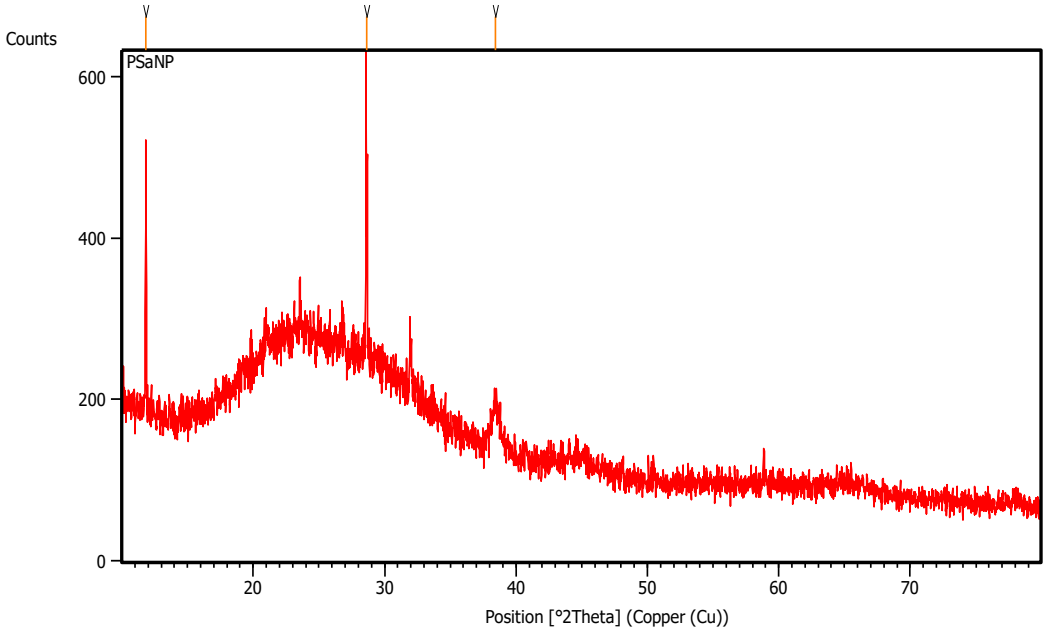

Figure 19c. XRD spectrum of PSaNP

Figure 19a-c. XRD spectrum of synthesized gold nanoparticles a) CRaNP by microwave heating, b) HAaNP at room temperature and c) PSaNP under sunlight

Table 19. XRD pattern of synthesized gold nanoparticles

S. No	Sample code	Pos. [°2 Th.]	Height [cts]	FWHM Left [°2 Th.]	d-spacing [Å]	Rel. Int. [%]
1	CRaNP	44.6308	64.49	0.2007	2.03036	100.00
2	HAaNP	38.4311	178.71	0.2676	2.34240	2.10
		44.6485	41.42	0.8029	2.02959	0.49
3	PSaNP	38.4445	53.22	0.8029	2.34161	17.64

4.6.3.2 XRD spectrum of CRarGO and HAarGO

CRarGO showed 2θ peaks at 28.8° and 26° with d-spacing 3 Å (**Figure 20a**). A broad peak was obtained at 2θ = 26° for HAarGO (**Figure 20b**). GO shows broad peak at 2θ = 9.75° **(Firdhouse and Lalitha, 2014)**. The peak shift in the GO indicates the formation of reduced graphene oxide with amorphous nature.

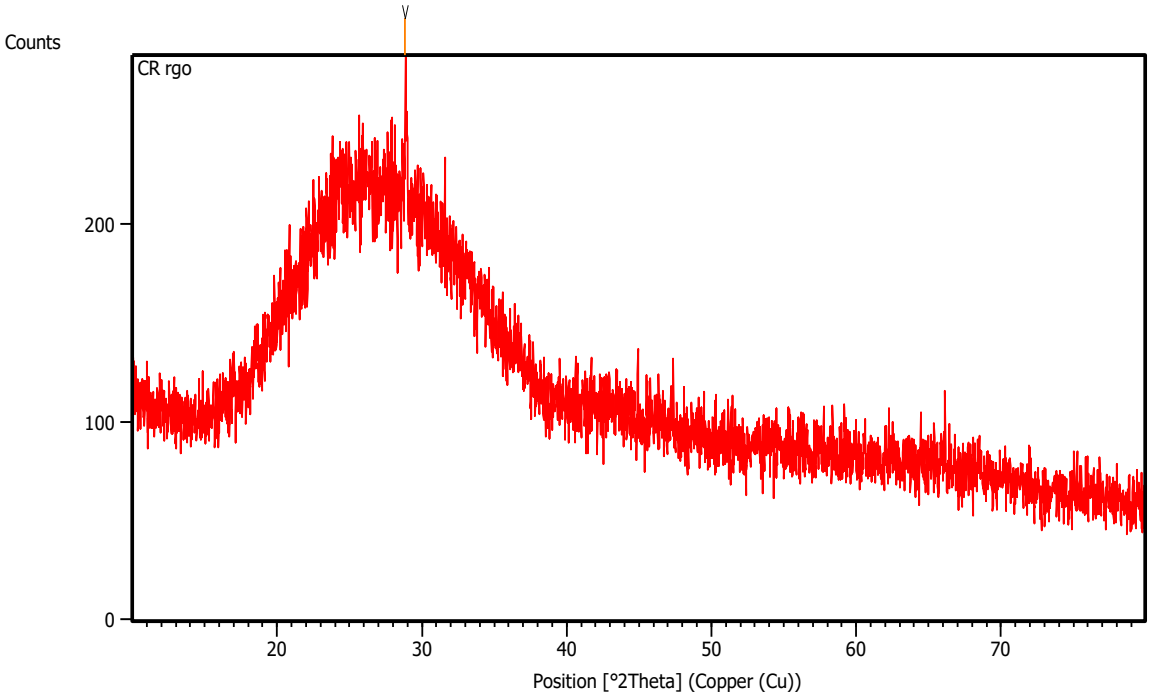

Figure 20a. XRD spectrum of CRarGO

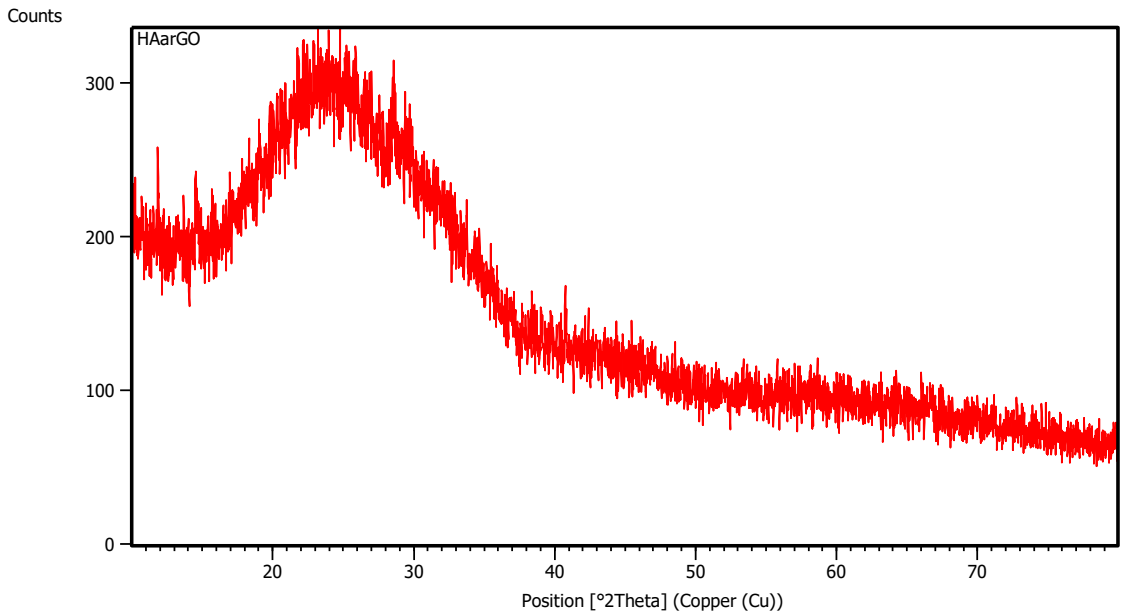

Figure 20b. XRD spectrum of HAarGO

Figure 20a and b. XRD spectrum of synthesized reduced graphene oxides

4.6.3.3 XRD spectrum of CRaNC and HAaNC

CRaNC and HAaNC shows 2θ = 38.7127º (**Figure 21a**) and 2θ = 38.49º (**Figure 21b**) with interspacing difference 2.3 Å. The particle size of the CRaNP present in CRaNC is 45 nm and HAaNP present in HAaNC showed 9 nm. In each nanocomposite shows 2θ peaks around 28º confirms the presence of rGO. The list of XRD peaks of gold nanoparticles in nanocomposites are given in **Table 20**.

Table 20. XRD pattern results of the synthesized nanocomposites

S. No	Sample code	Pos. [°2 Th.]	Height [cts]	FWHM Left [°2 Th.]	d-spacing [Å]	Rel. Int. [%]
1	CRaNC	38.7127	17.45	0.8029	2.32600	27.06
2	HAaNC	38.4941	41.45	0.9792	2.33677	0.56

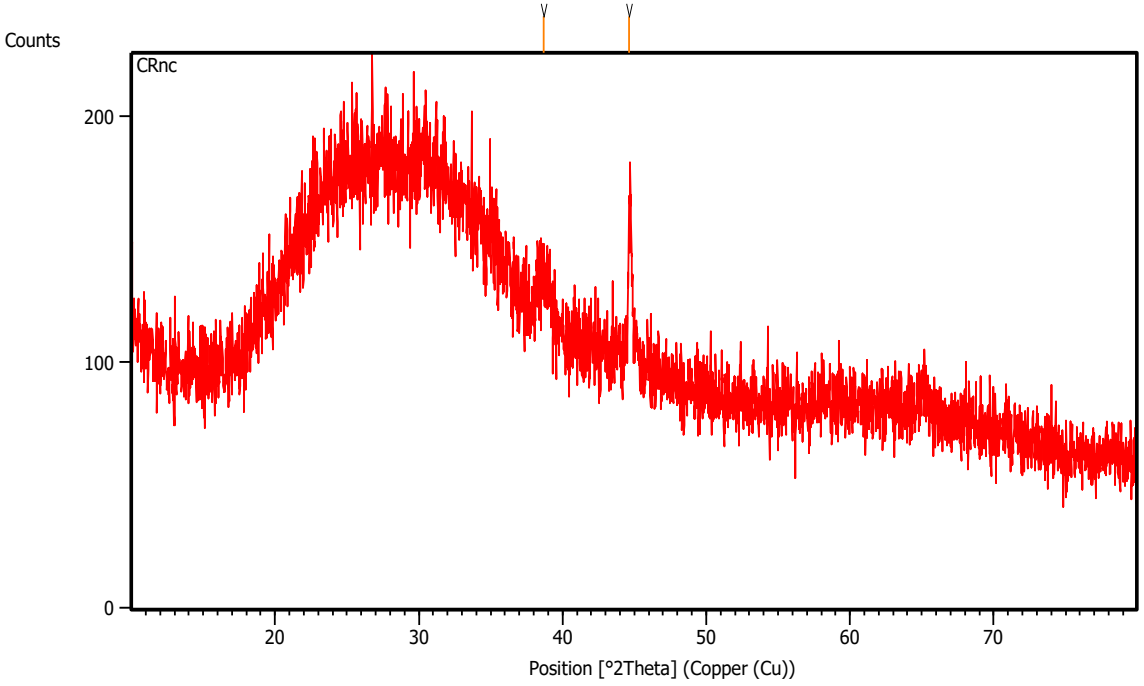

Figure 21a. XRD spectrum of CRaNC

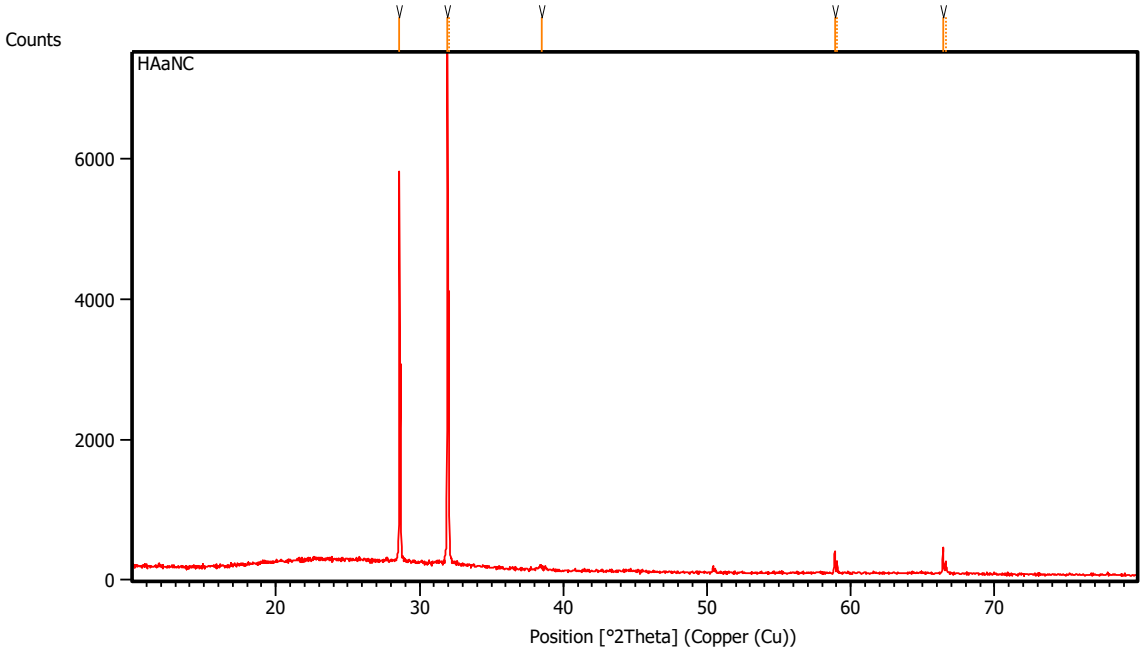

Figure 21b. XRD spectrum of HAaNC

Figure 21a and b. XRD spectrum of synthesized gold nanoparticles-reduced graphene oxide nanocomposites

4.6.4 Thermogravimetric analysis of CRarGO and HAarGO

Thermogravimetric analyses were carried out for CRarGO and HAarGO to analyze for their mass changes and thermal stability. The weight loss of CRarGO (**Figure 22a**) and HAarGO (**Figure 22b**) is caused in four phases, and the graph plotted between sample mass and temperature. The analysis carried out from room temperature to 1200°C. The first major weight loss observed for CRarGO-10.3% and HAarGO-16.5% at 100°C and 27°C-193°C respectively due to the loss of water and volatile moisture content in the sample. Second weight loss of CRarGO-8.2% and HAarGO-19.1% were seen at 189°C-250°C and 193-378°C respectively. This is due to the labile oxygen present in prepared rGO. The decomposition of stable oxygen present in rGO carbon structure occurred at 250°C-350°C for CRarGO (24.6%) and 378°C-619°C for HAarGO (39.9%). A Weight loss of 40.3% and 18.7% was noted in CRarGO and HAarGO at 674°C and 720-908°C respectively. This may be due to the removal of the carbon skeleton in oxygen contained carbon ring in the rGO structure. The results reveal the prepared reduced graphene oxide possesses the highest thermal stability.

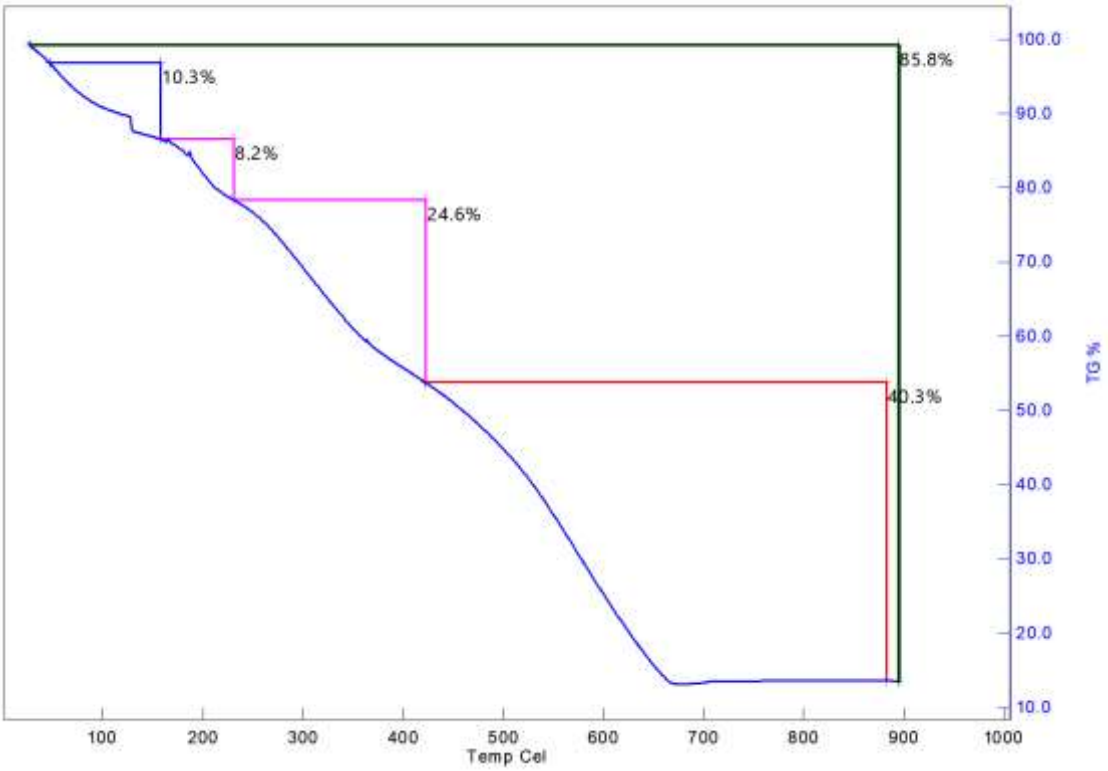

Figure 22a. TGA spectrum of CRarGO

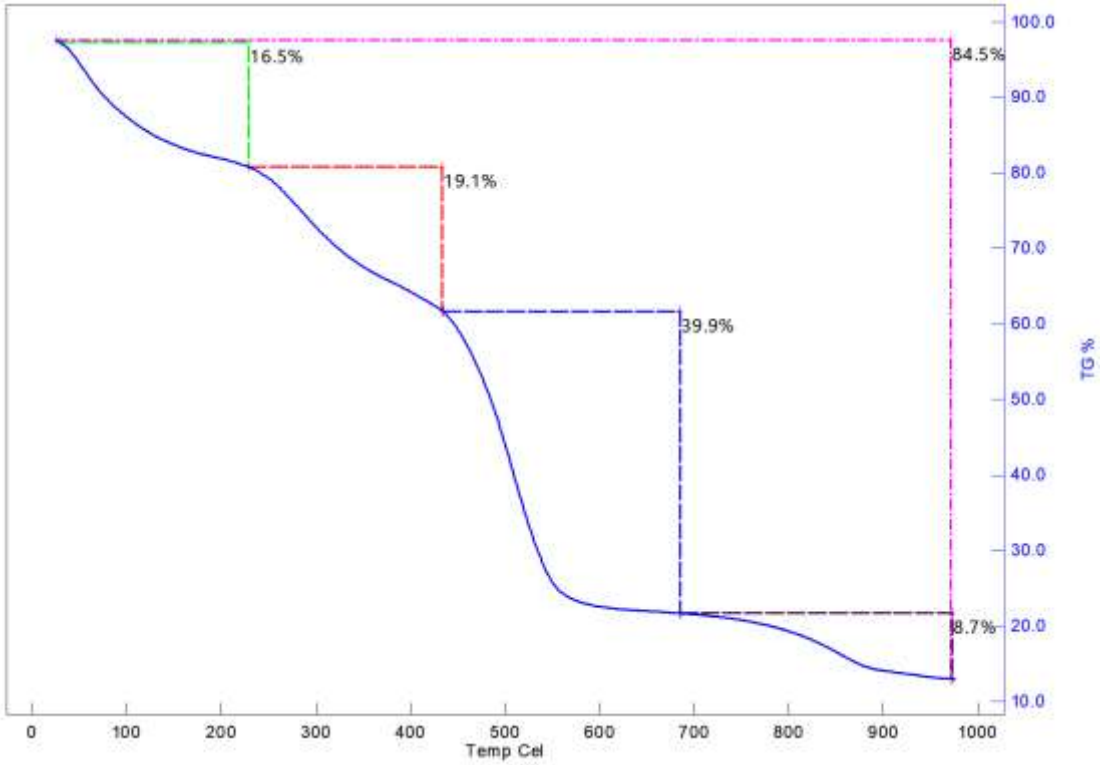

Figure 22b. TGA spectrum of HAarGO

Figure 22a and b. TGA spectrum of synthesized reduced graphene oxides

4.6.5 Raman spectroscopy analysis of CRarGO and HAarGO

The Raman spectrum (**Figure 23a and b)** of CRarGO and HAarGO showed D band at 1309.1 cm^{-1} and G band at 1589.8 and 1640 cm^{-1}, respectively. The D band raises by the destruction of the sp^2 character of carbon lattices **(Silva *et al*., 2019)**. Scattering of E_2g phonon (first-order scattering) in sp^2 carbon atoms raises the G- band **(Purkait *et al*., 2017)**. GO showed band at 1350 cm^{-1} (D-band) and 1589 cm^{-1} (G-band). The bands are occurred due to the hexagonally arranged zig-zag and armchair edges of graphene lattice **(Childres *et al*., 2013)**. The armchair edges of graphene involve scattering the charge carriers and raises D band. This happens due to the excitation of laser polarization parallel to the edges of the armchair. In the case of zig-zag edges, the effect is observed quite smaller due to the roughness in the edges. When the polarized laser excitation occurs in perpendicular to the zig-zag edges and parallels to armchair edges the G band appears. Some minor peaks are also observed in prepared rGOs. These minor peaks are represented as D′, D+G, D+D′ and G+D′. These peaks are representing the defects in shape, intensity, and position of the carbon lattices in

graphene oxide **(Adarsh and Sundara, 2012)**. The shift in G band from 1589 to 1689.8 cm^{-1} (for CRarGO) and 1640.28 cm^{-1} (for HAarGO) and there is no 2D band observed in prepared rGOs which confirms the formation of few-layer graphene oxide.

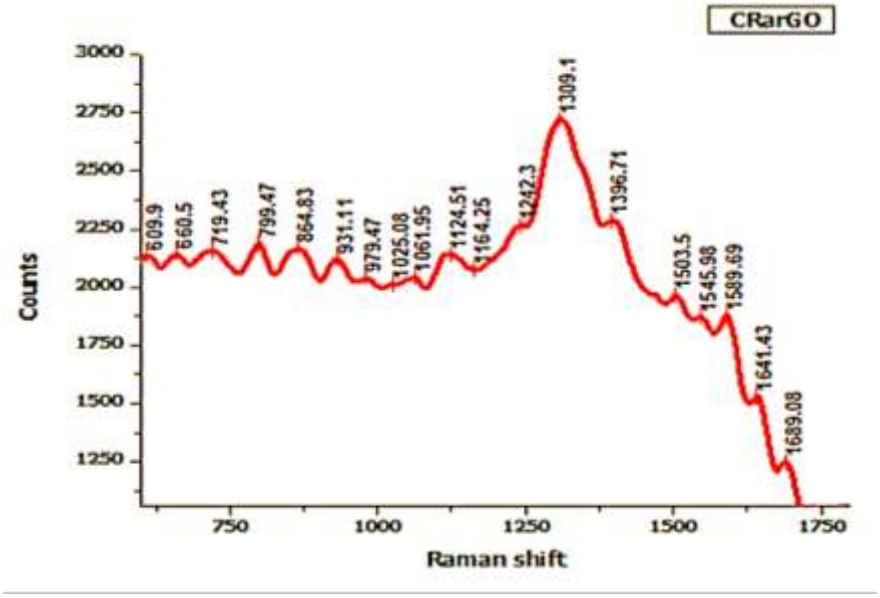

Figure 23a. Raman spectrum of CRarGO

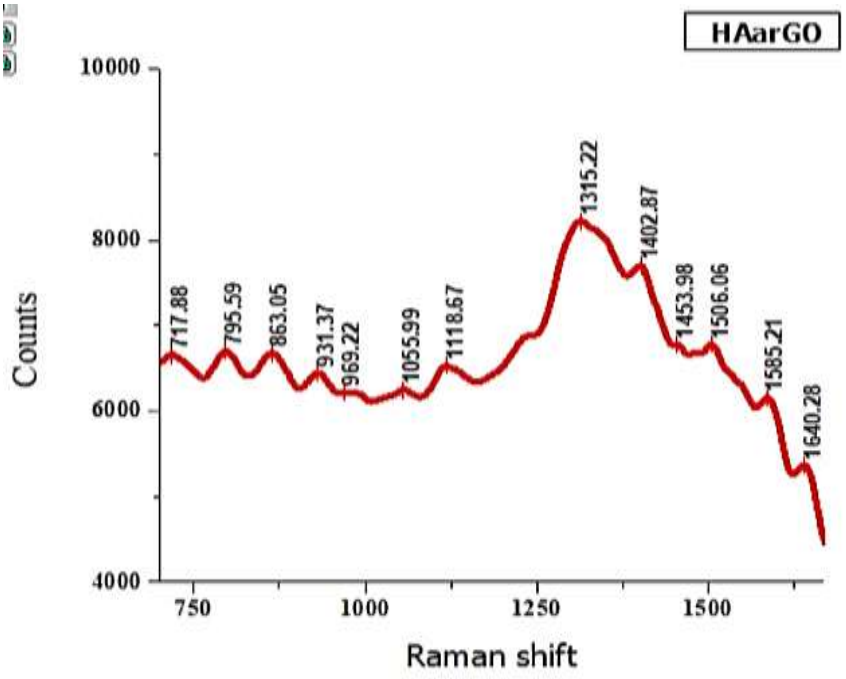

Figure 23b. Raman spectrum of HAarGO

Figure 23a and b. Raman spectrum of synthesized reduced graphene oxides

4.6.6 Field Emission Scanning Electron Microscopy of prepared nanoparticles

4.6.6.1 FESEM images of CRaNP, HAaNP and PSaNP

The surface morphology of synthesized CRaNP, HAaNP and PSaNP were seen using FESEM (MIRA3, TESCAN). CRaNP (**Figure 24a and b**) shows spherical shaped gold nanoparticles and it is embedded with CRablank. The average particles size of the CRaNP is 21 nm. In HAaNP, accumulation of spherical-shaped gold nanoparticles was seen in **Figure 25a** with an average size of 34.80 nm. The surface morphology of PSablank (**Figure 26a**) and PSaNP (**Figure 27a and b**) was evaluated. PSablank was available in the form of flakes with two different edges of sharp and flat.

EDS analysis revealed the presence of Na, Mg, K, Ca and Au in CRaNP (**Figure 24c**). In HAaNP confirms the presence of Ca, K, Na, O, Al, Mg, Cl, Si, Au and Cl (**Figure 25b**). Apart from gold ions, the presence of other elements are due to the available minerals in the plant extract. PSablank is composed of Si, O, Na, Mg, Al, Ca and Ti. PSaNP revealed the presence of O, Si, Au, Na, Ca, Cl, Mg, K and Al. The percentage composition of PSablank and PSaNP are given in **Figure 26b** and **Figure 27c**. The mapping of synthesized gold nanoparticles showed the well distribution of zerovalent gold ions in CRaNP, HAaNP and PSaNP.

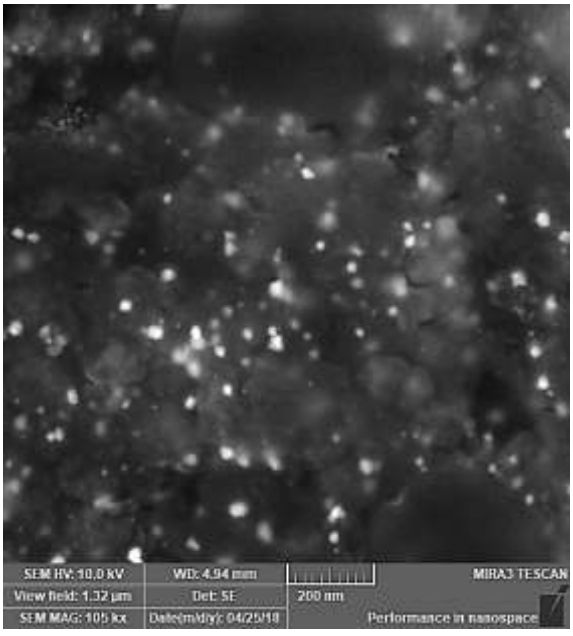

Figure 24a. FESEM image of CRaNP

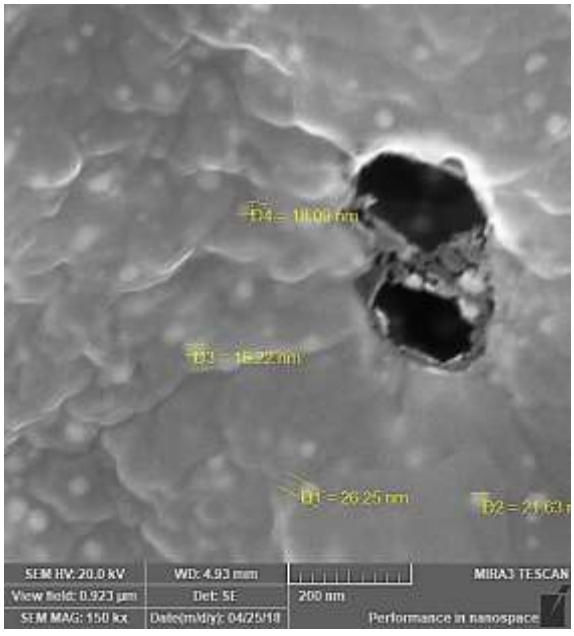

Figure 24b. FESEM image of CRaNP

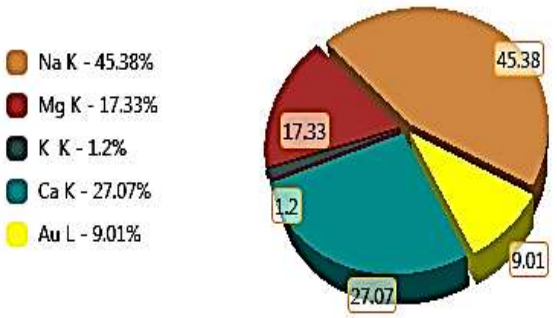

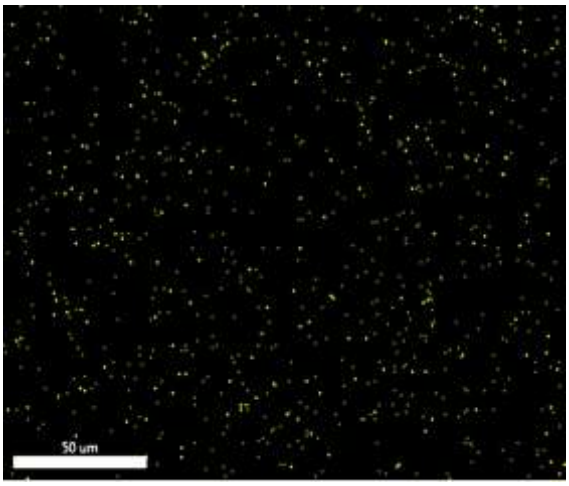

Figure 24c. EDS spectrum of CRaNP

Figure 24d. Mapping image of CRaNP

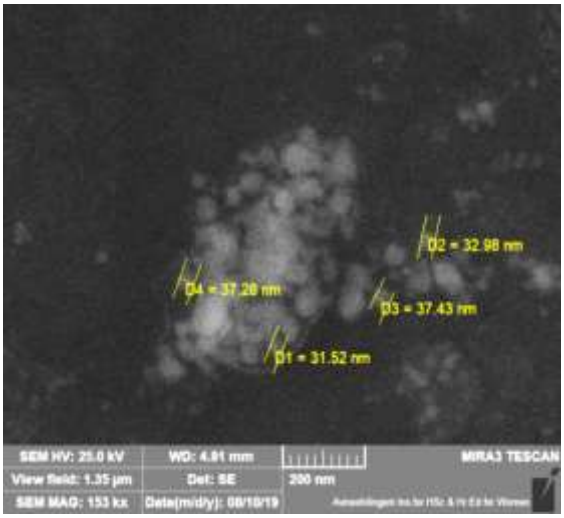

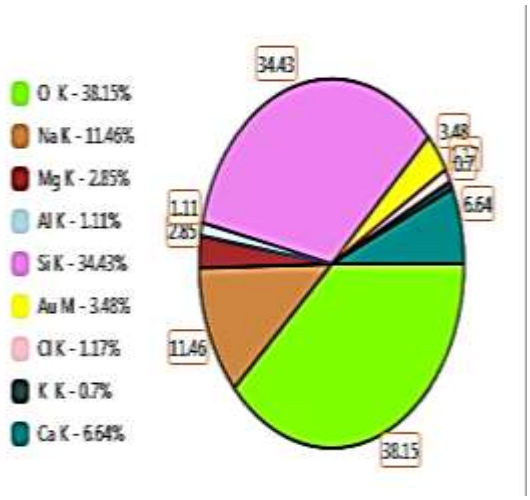

Figure 25a. FESEM image of HAaNP

Figure 25b. EDS spectrum of HAaNP

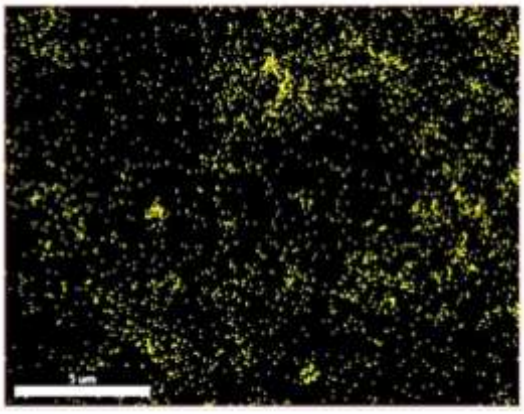

Figure 25c. Mapping image of HAaNP

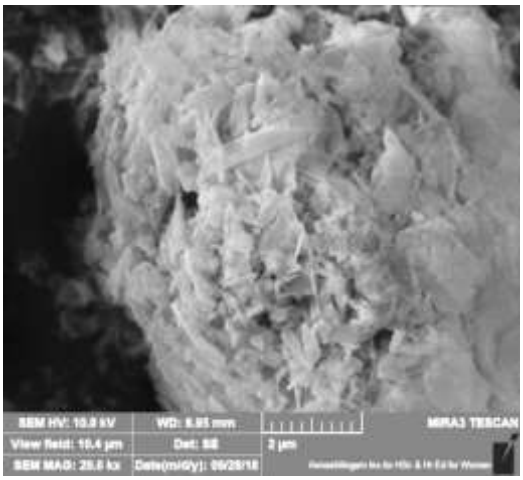

Figure 26a. FESEM image of powder of pumice stone on glass plate

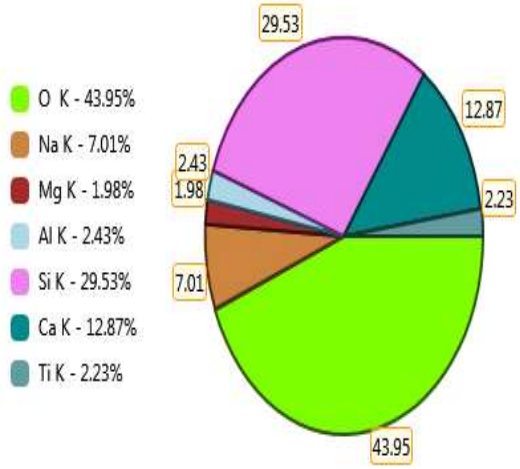

Figure 26b. EDS spectrum of pumice stone

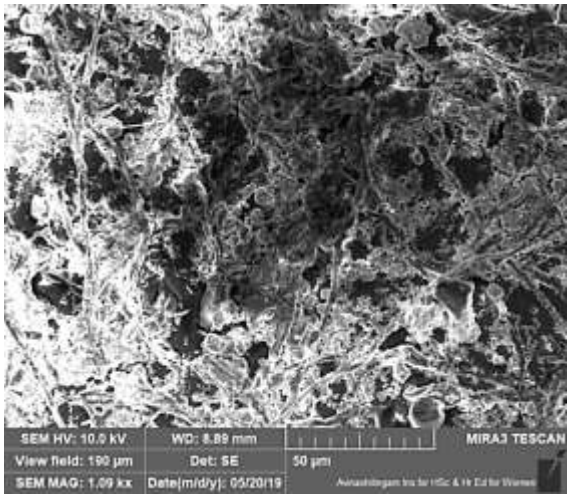

Figure 27a. FESEM image of PSaNP

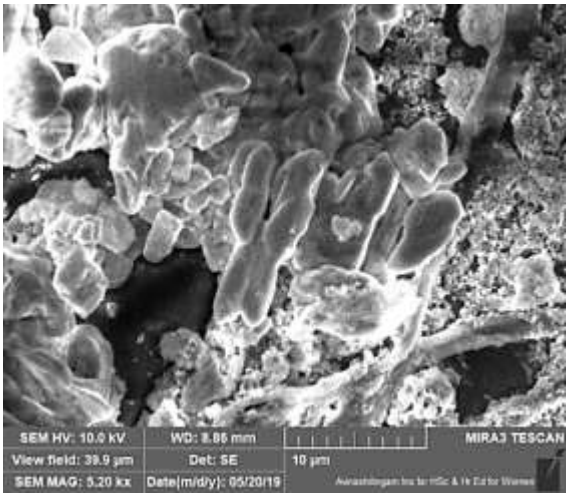

Figure 27b. FESEM image of PSaNP

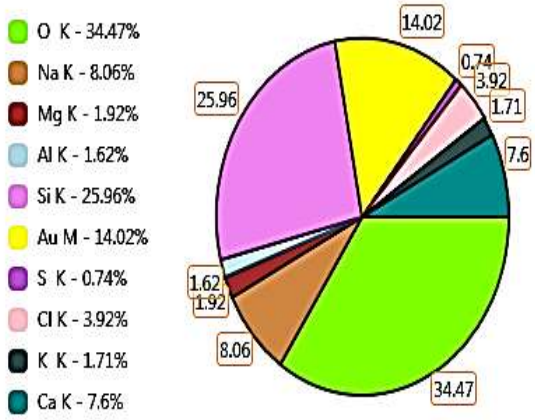

Figure 27c. EDS spectrum of PSaNP

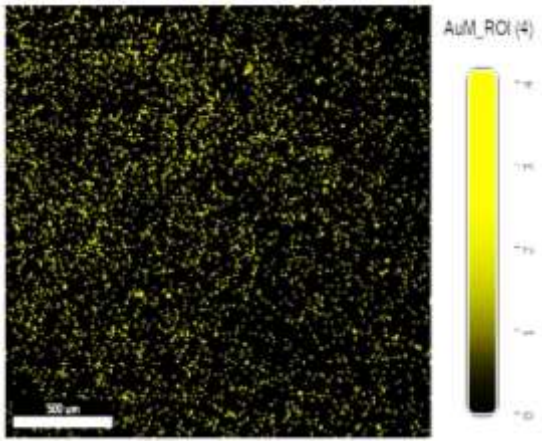

Figure 27d. Mapping image of PSaNP

4.6.6.2 FESEM images of CRarGO and HAarGO

CRarGO and HAarGO were prepared by treating aqueous extract of selected plants with GO by refluxing method. The prepared rGO strongly dispersed in distilled water and coated on a cleaned glass plate. The surface analysis of the rGO was taken in various working difference (WD) using FESEM instrument. In working difference 5.2 mm, the CRarGO (**Figure 28a and b**) shows closely packed flakes texture.

HAarGO shows accumulated flakes at 5.25 mm working distance (**Figure 29a**). At WD-15.08 mm (**Figure 29b**), the clear rGO flakes constructed as the rod in HAarGO with uneven shaped edges was seen and the diameter of the rod is 55.93 and 68.60 µm. From this observation reveals, the HAarGO is capable of forms a bundle of rGO rods.

CRarGO and HAarGO possess a high content of carbon and oxygen atoms which confirmed by EDS analysis. The distribution of elements present in the samples was seen in mapping analysis. The carbon distribution is given in **Figures 28c and 29d**. Carbon particles are capable of forming clusters and resulting in the formation of accumulation in rGO structure.

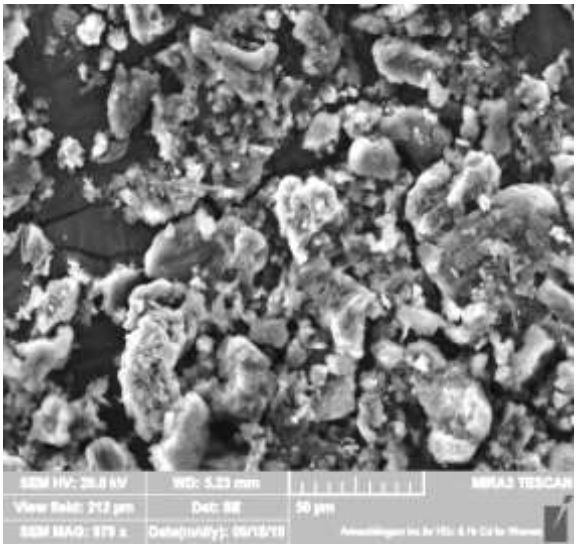

Figure 28a. FESEM image of CRarGO

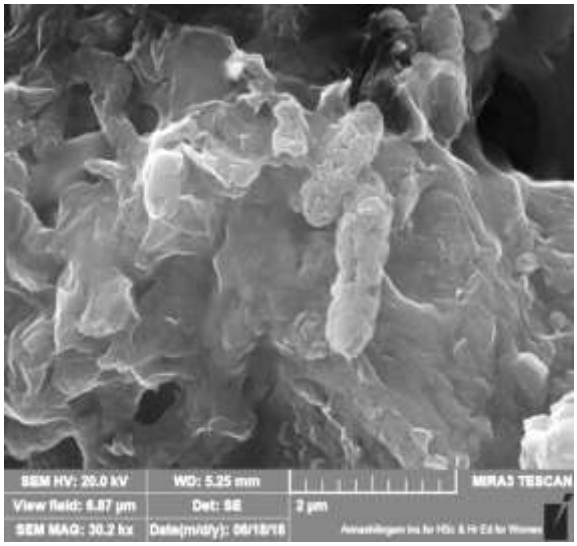

Figure 28b. FESEM image of CRarGO

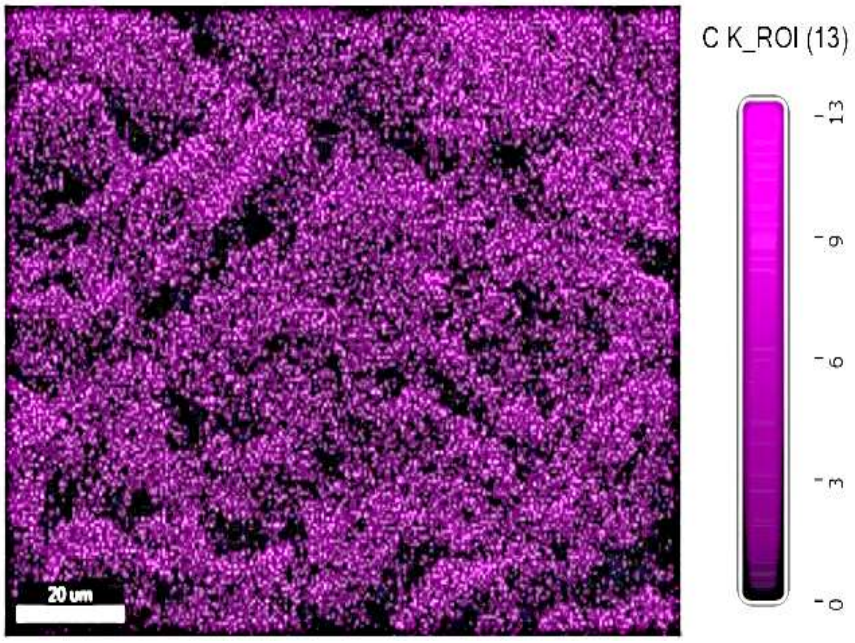

Figure 28c. Carbon distribution in CRarGO

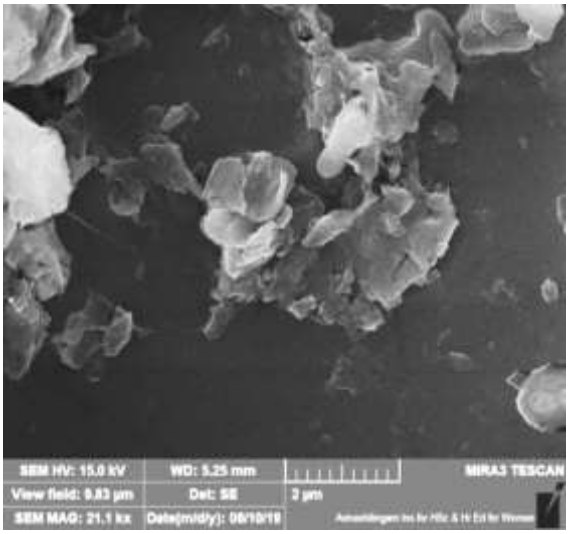

Figure 29a. FESEM image of HAarGO (WD-5.25 mm)

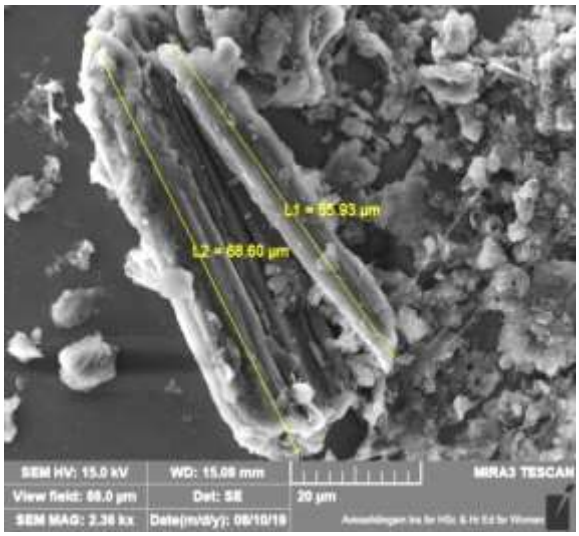

Figure 29b. FESEM image of HAarGO (WD-15.08 mm)

Figure 29c. FESEM image of HAarGO (WD-8.93 mm)

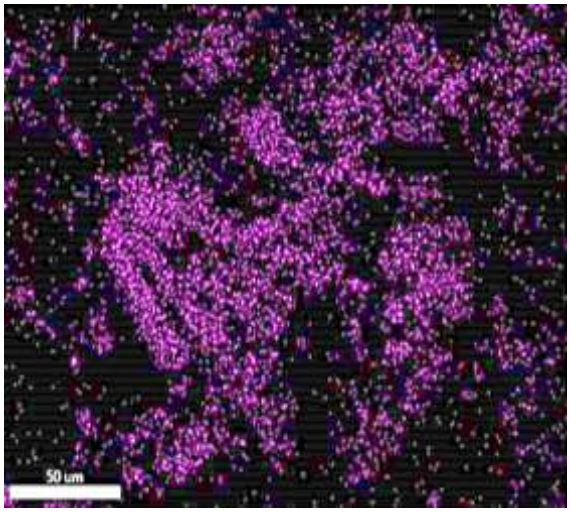

Figure 29d. Carbon distribution in HAarGO

4.6.6.3 FESEM images of CRaNC and HAaNC

The prepared AuNPs-rGO composite was analyzed in FESEM. In **Figure 30a and 30b** and **Figures 31a and 31b** show the surface texture of CRaNC and HAaNC respectively. AuNPs and rGO in nanocomposite strongly bonded together. Few AuNPs are seated inside the carbon structure. The EDS analysis reveals the presence of both carbon and nanogold in CRaNC and HAaNC. The distribution of carbon and gold were seen in mapping analysis. The carbon content of CRarGO (**Figure 30c**) and HAarGO (**Figure 31c)** were seen in accumulated form and CRaNP (**Figure 30d**) and HAaNP

(**Figure 31d**) are uniformly distributed on rGO. Due to the nanosized AuNPs can easily penetrate through the micro-sized rGO and seated strongly into them. The flakes of prepared rGO are capable of forms the cluster resulting in the accumulated structure in the nanocomposite. There is a strong bond can be possible between Au and C materials **(Chenier *et al*., 1989; Hong *et al*., 2013; Rekhroukh *et al*., 2017)**. In this regard, this study suggests a strong Au-C bond between AuNPs and rGO.

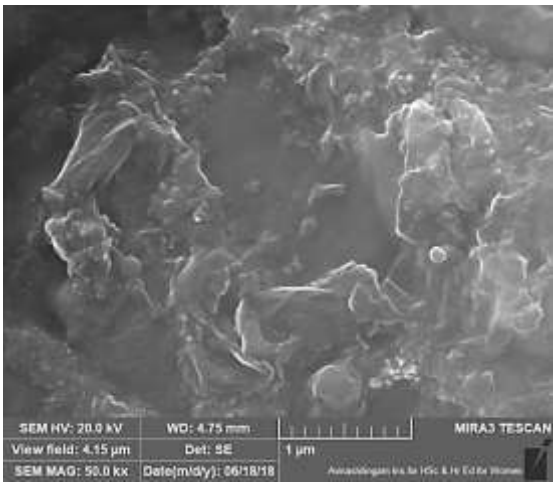

Figure 30a. FESEM image of CRaNC

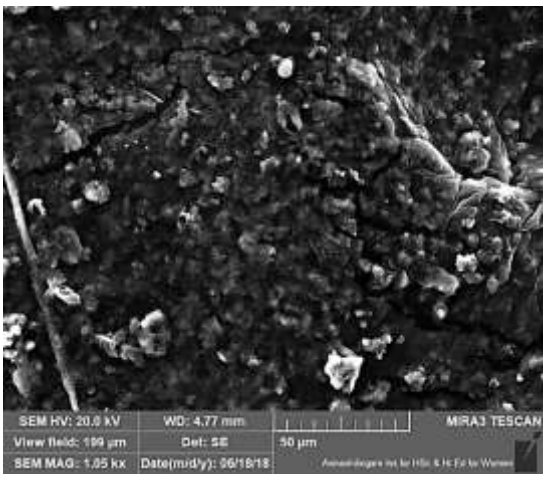

Figure 30b. FESEM image of CRaNC

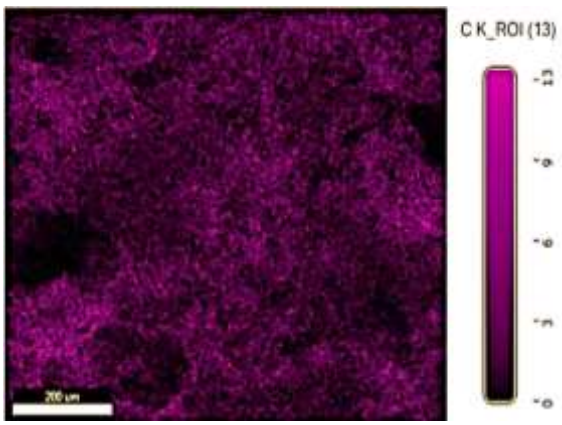

Figure 30c. Carbon distribution in CRaNC

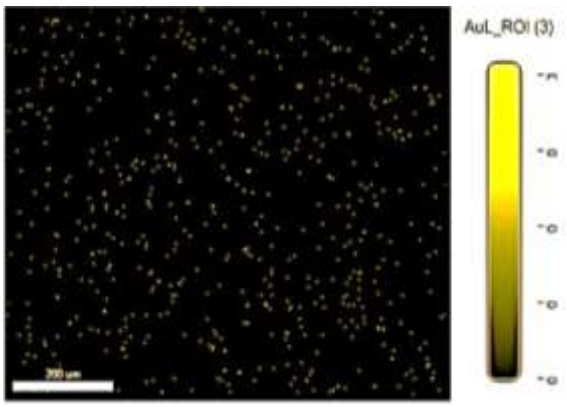

Figure 30d. Gold nanoparticle distribution in CRaNC

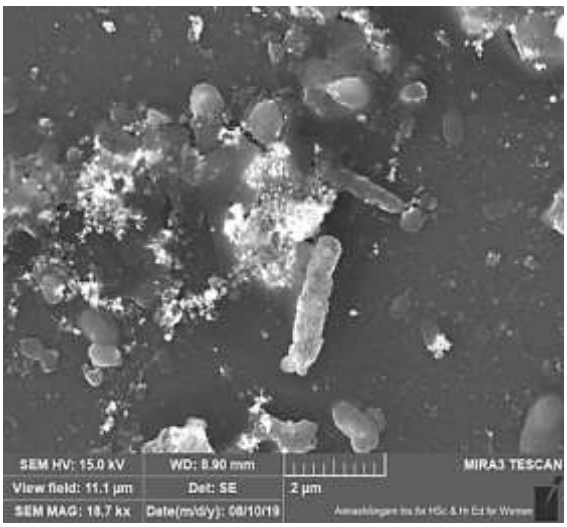

Figure 31a. FESEM image of HAaNC

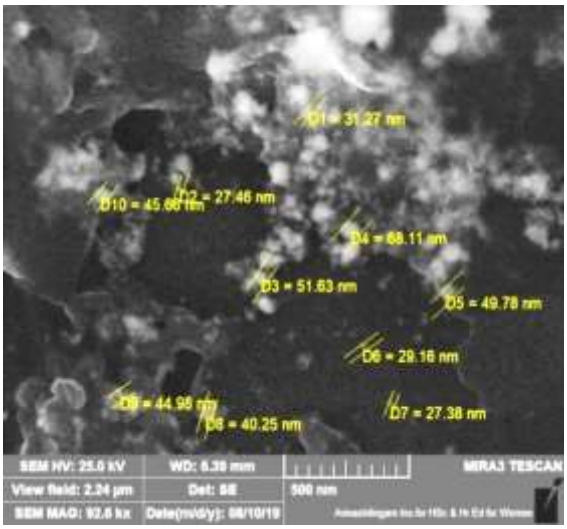

Figure 31b. FESEM image of HAaNC

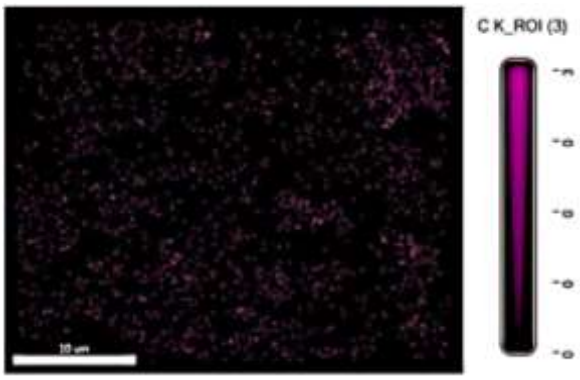

Figure 31c. Carbon distribution in HAaNC

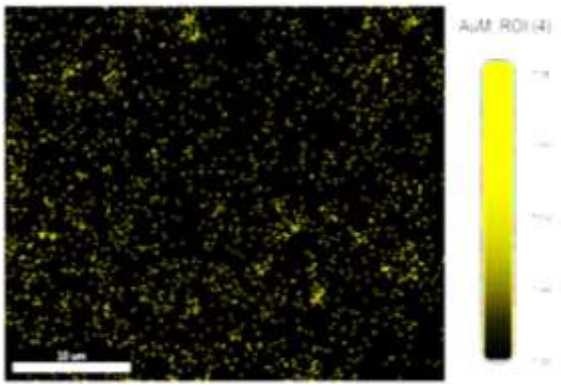

Figure 31d. Gold nanoparticle distribution in HAaNC

4.7 Biological activities of synthesized AuNPs, rGO and AuNPs-rGO composite

4.7.1 Antibacterial activity of synthesized nanoparticles against gram-positive and gram-negative bacteria

Synthesized nanoparticles were tested for their antibacterial activity by Agar-well diffusion method. Gram-positive (*Staphylococcus aureus* and *Bacillus subtilis*) and gram-negative (*Salmonella paratyphi* and *Escherichia coli*) bacteria were used in this study. Ciprofloxacin is a commercially available antibacterial tablet used as a standard for comparing the efficiency of synthesized particles. The diameter of the inhibition zone was measured in millimetre and the Zone of Inhibition is represented as ZOI. The concentrations of the samples are represented as C_1, C_2, C_3 for 150, 200 and 250 µL respectively.

4.7.1.1 Results of antibacterial activity of CRaNP, HAaNP and PSaNP

Synthesized gold nanoparticles showed good antibacterial potential against four bacterial pathogens. The anti-bactericidal potential of greyish pink coloured CRaNP, violet coloured HAaNP and bluish grey coloured PSaNP are given in **Table 21**. The ZOI 15.7, 13, 18 and 17 mm were observed for CRaNP against *Escherichia coli*, *Staphylococcus aureus*, *Salmonella paratyphi* and *Bacillus subtilis* respectively. The ZOI increases by an increase in the concentration of CRaNP from C_1 to C_3. The highest ZOI observed against *Escherichia coli* (19.7 mm), *Staphylococcus aureus* (21 mm), *Salmonella paratyphi* (24.2 mm) and *Bacillus subtilis* (19.5 mm). The ZOI of CRaNP noted after 24h inhibition.

CRaNP shows biofilm formation of bacteria on the inhibited area **(Figure 32a and b)** after 48h treatment. Similarly, ZOI increases by increasing HAaNP concentration. The highest ZOI observed at C_3 concentration shows 19, 16 and 17 mm against *Escherichia coli*, *Salmonella paratyphi* and *Bacillus subtilis* respectively. The ZOI 10 mm against *Staphylococcus aureus* were noted for *Hemigraphis alternata* aided AgNP **(Priyanka *et al*., 2016)**. Here, HAaNP showed highest ZOI (19 mm) against *Staphylococcus aureus*.

PSaNP showed significant antibacterial potential against gram-positive and negative bacteria. PSablank embedded PSaNP well dispersed using an ultrasonic homogenizer before testing. The highest ZOI observed (18 mm) against *Bacillus subtilis* and *Escherichia coli* and are given in **Table 21**. The ZOI 16 and 14 mm were observed against *Staphylococcus aureus* and *Salmonella paratyphi* respectively. The gold nanoparticle has the potential to penetrate the cell wall of the bacteria and break down the cell membranes **(Tao, 2018)**. Hence the interaction between bacteria and nanoparticles enhance the efficiency of inhibition **(Bharathi *et al*., 2019)**.

Table 21. Inhibition zone of CRaNP, HAaNP and PSaNP against gram-positive and gram-negative bacteria

S. No	Concentration of the samples (µL)	Zone of Inhibition (mm)			
		Escherichia coli	***Staphylococcus aureus***	***Salmonella paratyphi***	***Bacillus subtilis***
1	CRaNP C_1	15.7	13	18	17
2	CRaNP C_2	17.2	18	21.2	18.7
3	CRaNP C_3	19.7	21	24.2	19.5
4	HAaNP C_1	17	17	16	16
5	HAaNP C_2	18	19	14	15
6	HAaNP C_3	19	19	16	17
7	PSaNP C_1	15	15	11	16
8	PSaNP C_2	17	15	13	17
9	PSaNP C_3	18	16	14	18

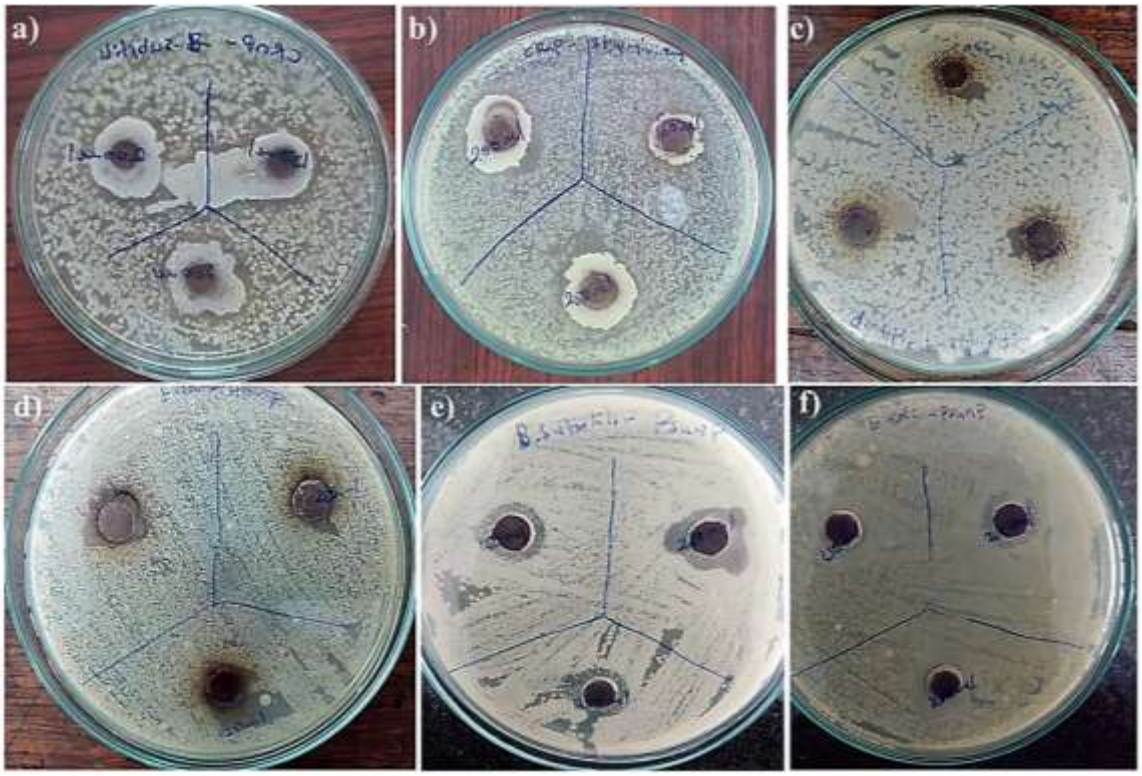

Figure 32a-f. Photographs of ZOI of CRaNP (a and b), HAaNP (c and d) and PSaNP (e and f) against gram-positive and gram-negative bacteria

4.7.1.2 Results of antibacterial activity of CRarGO and HAarGO

Synthesized reduced graphene oxides were well dispersed in distilled water using an ultrasonic homogenizer. Reduced graphene oxide using aqueous extract of *Cyperus rotundus* tuber (**Figure 33a-c**) showed excellent bactericidal inhibition activity. Similarly, rGO using *Hemigraphis alternata* leaves (**Figure 33d-f**) exhibit significant activity against *Escherichia coli*, *Staphylococcus aureus*, *Salmonella paratyphi* and *Bacillus subtilis*. When the concentration of prepared rGO increases from C_1–C_3 the zone of inhibition also increases (**Table 22**).

CRarGO showed ZOI inhibition of 17.5 mm at C_1 concentration against *Escherichia coli*. CRarGO showed ZOI of 13.7, 16 and 14 mm against *Staphylococcus aureus*, *Salmonella paratyphi* and *Bacillus subtilis* respectively. HAarGO showed 16 mm against *Escherichia coli* and 17 mm against *Salmonella paratyphi* and 15 mm against *Staphylococcus aureus* and *Bacillus subtilis*. With an increase in the concentration of CRarGO from C_1 to C_3, the ZOI increases from 17.5 to 19.2 mm against *Escherichia coli*, 13.7 to 17.2 mm against *Staphylococcus aureus*, 16 to 23.7 mm against *Salmonella paratyphi*, and 14 to 17.5 mm against *Bacillus subtilis*. For HAarGO, the ZOI increases from 13 to 16 mm against *Escherichia coli* and 12 to 15 mm against *Staphylococcus aureus*, 14 to 17 mm against *Salmonella paratyphi* and 13 to 15 mm against *Bacillus subtilis*.

CRarGO displays the highest inhibition than HAarGO. The highest zone of inhibition observed for CRarGO against *Salmonella paratyphi* (23.7 mm) > *Escherichia coli* (19.2 mm) > *Bacillus subtilis* (17.5 mm) > *Staphylococcus aureus* (17.2 mm). HAarGO showed highest ZOI against *Salmonella paratyphi* (17 mm) > *Escherichia coli* (16 mm) > *Staphylococcus aureus* (15 mm) and *Bacillus subtilis* (15 mm). Physical and chemical modes of action are involved in the antibacterial activity of reduced graphene oxide. The physical damages are commonly induced by the direct interaction of graphene with the cell membrane of bacteria. The chemical mode is mainly noted from oxidative stress by charge transfer and ROS production on the cell membrane resulting in the destructing and damaging the bacteria cell membrane **(Parveen *et al*., 2019)**. It also alters the DNA/RNA structure and properties **(Mohammed *et al*., 2020)**. Functional groups containing more oxygen on CRarGO and HAarGO surfaces enhance the ROS production of oxygen anions and hydroxyl radicals are involved in bacteria inactivation.

Table 22. Inhibition zone of CRarGO and HAarGO against gram-positive and gram-negative bacteria

S. No	Concentration of the samples (µL)	Zone of Inhibition (mm)			
		Escherichia coli	***Staphylococcus aureus***	***Salmonella paratyphi***	***Bacillus subtilis***
1	CRarGO C_1	17.5	13.7	16	14
2	CRarGO C_2	18.5	16.2	22	15.7
3	CRarGO C_3	19.2	17.2	23.7	17.5
4	HAarGO C_1	16	12	14	13
5	HAarGO C_2	15	14	15	14
6	HAarGO C_3	13	15	17	15

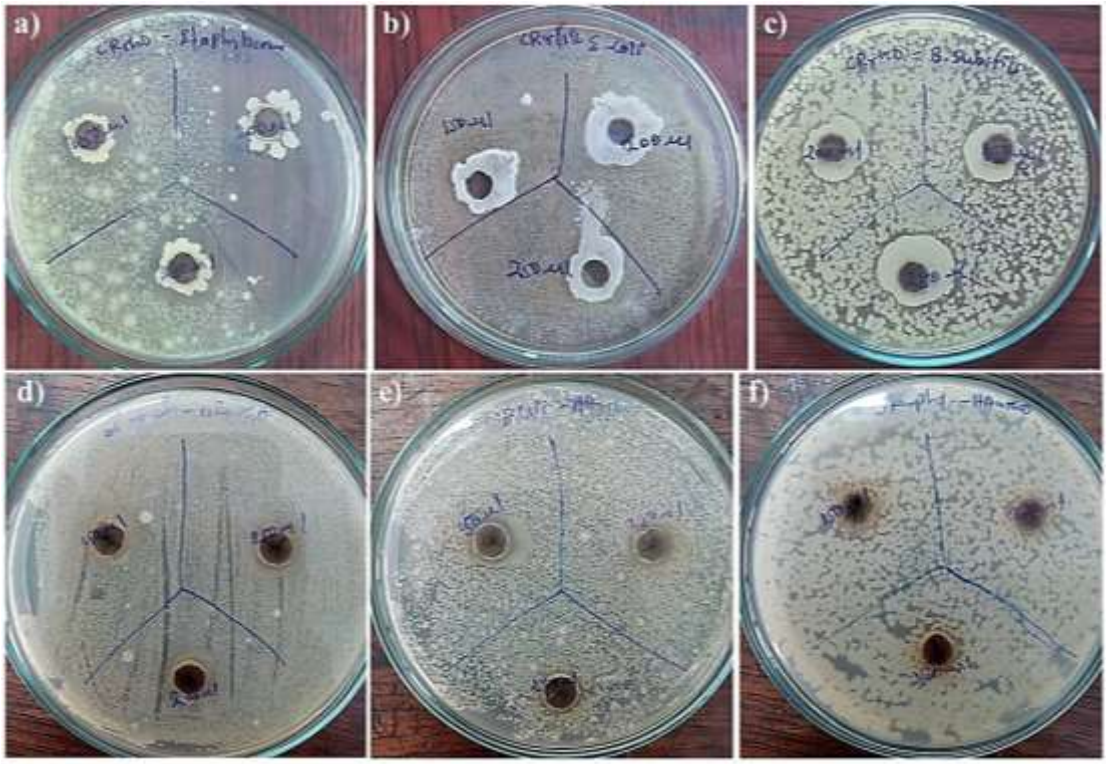

Figure 33a-f. Photographs of ZOI of CRarGO (a-c) and HAarGO (d-f) against gram-positive and gram-negative bacteria

4.7.1.3 Results of antibacterial activity of CRaNC and HAaNC

The nanocomposite is composed of an equal ratio of AuNPs and rGO. The evaluation of the antibacterial activity of CRaNC and HAaNC was carried out using Agar-well diffusion method (**Table 23 and Figure 34a-f**). CRaNC showed lesser inhibition

(13.7 mm) against *Escherichia coli* at lower concentration. With an increase in the concentration of CRaNC from C_1 to C_3, the ZOI increased (13.7 to 16.7 mm). The highest ZOI 16. 7 mm was noted against *Escherichia coli*. At minimum concentration (C_1) of CRaNC the highest ZOI 14.7, 20, 14 mm was observed against *Staphylococcus aureus*, *Salmonella paratyphi* and *Bacillus subtilis* respectively.

In HAaNC, the ZOI against *Escherichia coli* (15 to 16 mm), *Staphylococcus aureus* (16 to 20 mm), *Salmonella paratyphi* (13 to 14 mm), and *Bacillus subtilis* (14 to 17 mm) increases with an increase in the concentration (C_1 to C_3). HAaNC showed the highest inhibition against *Staphylococcus aureus* (20 mm), *Bacillus subtilis* (17 mm), *Escherichia coli* (16 mm) and *Salmonella paratyphi* (14 mm). Comparatively at C_3 concentration CRaNC showed the highest inhibition than HAaNC against *Escherichia coli* and in C_1 concentration CRaNC showed highest ZOI (20 mm) against *Salmonella paratyphi* than HAarGO. At C_3 concentration HAaNC showed the highest inhibition than CRaNC against *Staphylococcus aureus* (20 mm) and *Bacillus subtilis* (17 mm). The sharp edges in rGO sheets facilitate the transport of the metal ions through the cell membrane and disrupt the cells **(Prasad *et al*., 2017)**. Gold nanoparticles present in the nanocomposite can penetrate through the cell membrane and inactivate the bacteria. In nanocomposite charge transfer and particle penetration of combined AuNPs and rGO are responsible for the complete cell death.

Table 23. Inhibition zone of CRaNC and HAaNC against gram-positive and gram-negative bacteria

S. No	Concentration of the samples (µL)	Zone of Inhibition (mm)			
		Escherichia coli	***Staphylococcus aureus***	***Salmonella paratyphi***	***Bacillus subtilis***
1	CRaNC C_1	13.7	14.7	20	14
2	CRaNC C_2	16.2	12.5	18	11.7
3	CRaNC C_3	16.7	10.5	16.2	11.7
4	HAaNC C_1	15	16	13	14
5	HAaNC C_2	15	18	13	16
6	HAaNC C_3	16	20	14	17

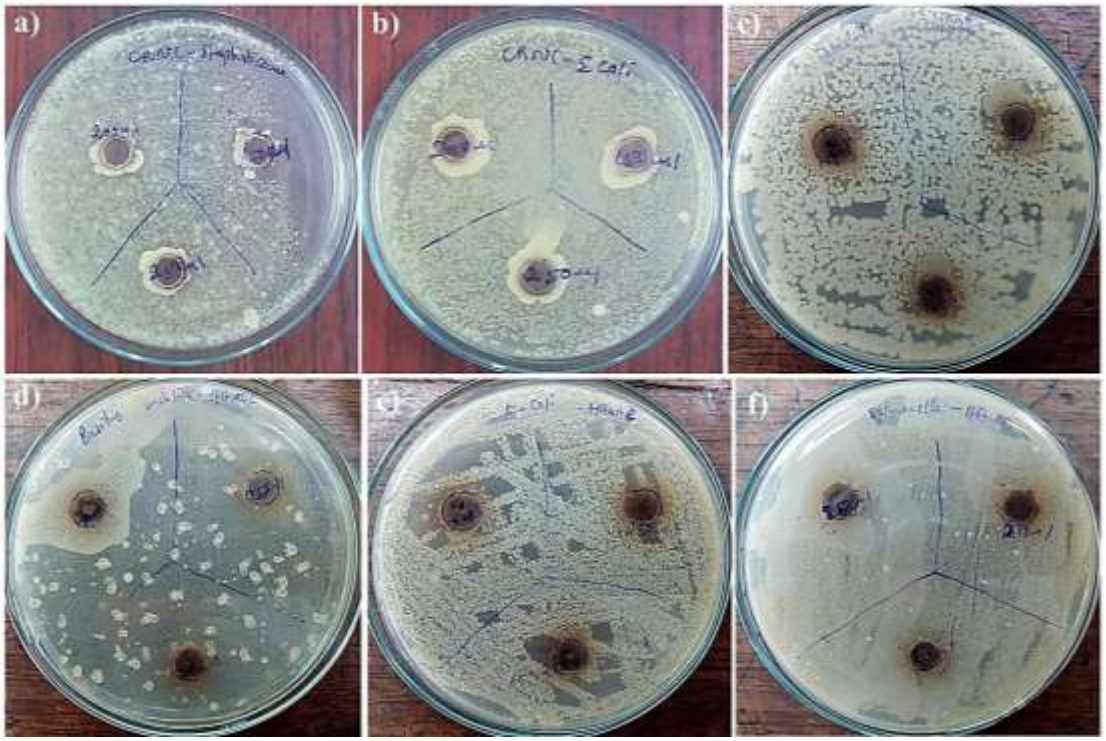

Figure 34a-f. Photographs of ZOI of CRaNC (a-c) and HAaNC (d-f) against gram-positive and gram-negative bacteria

4.7.1.4 Results of antibacterial activity of CRablank, HAablank and PSablank

The prepared CRablank, HAablank and PSablank were analyzed for their antibacterial activity against selected four bacteria and the results are given in **Table 24 and Figure 35a-f**. The CRablank showed minimum inhibitory activity against *Bacillus subtilis* (7.7 mm) than other bacteria. The ZOI increases from 12.5 to 14 mm against *Escherichia coli*, 13 to 17 mm against *Staphylococcus aureus* and 12.5 to 18.7 mm against *Salmonella paratyphi*. The highest ZOI was observed at C_3 concentration against all selected pathogens.

HAablank showed ZOI 15 and 16 mm against *Escherichia coli* and *Staphylococcus aureus* respectively. HAablank displayed 9 and 14 mm against *Salmonella paratyphi* and *Bacillus subtilis,* respectively. The results revealed the HAablank to show lower inhibitory action on *Salmonella paratyphi*. The available phytoconstituents present in CRablank and HAablank are responsible for this activity.

PSablank showed 12 to 16 mm ZOI and 17 to 19 mm ZOI with C_1 to C_3 concentration against *Escherichia coli* and *Staphylococcus aureus,* respectively. The

maximum zone of inhibition 11 mm was observed against *Salmonella paratyphi* and 10 mm against *Bacillus subtilis*. The important metals present in pumice may be involved in this activity. The results of inhibition activity of PSablank reveals which is an efficient agent against *Staphylococcus aureus* (19 mm) and *Escherichia coli* (16 mm) inhibition.

Table 24. Inhibition zone of CRablank, HAablank and PSablank against gram-positive and gram-negative bacteria

S. No	Concentration of the samples (µL)	Zone of Inhibition (mm)			
		Escherichia coli	***Staphylococcus aureus***	***Salmonella paratyphi***	***Bacillus subtilis***
1	CRablank C_1	12.5	13	12.5	7.7
2	CRablank C_2	13.5	16	11.7	7.7
3	CRablank C_3	14	17	18.7	8
4	HAablank C_1	15	13	7	13
5	HAablank C_2	15	16	7	13
6	HAablank C_3	13	16	9	14
7	PSablank C_1	12	17	11	10
8	PSablank C_2	12	17	11	10
9	PSablank C_3	16	19	11	10

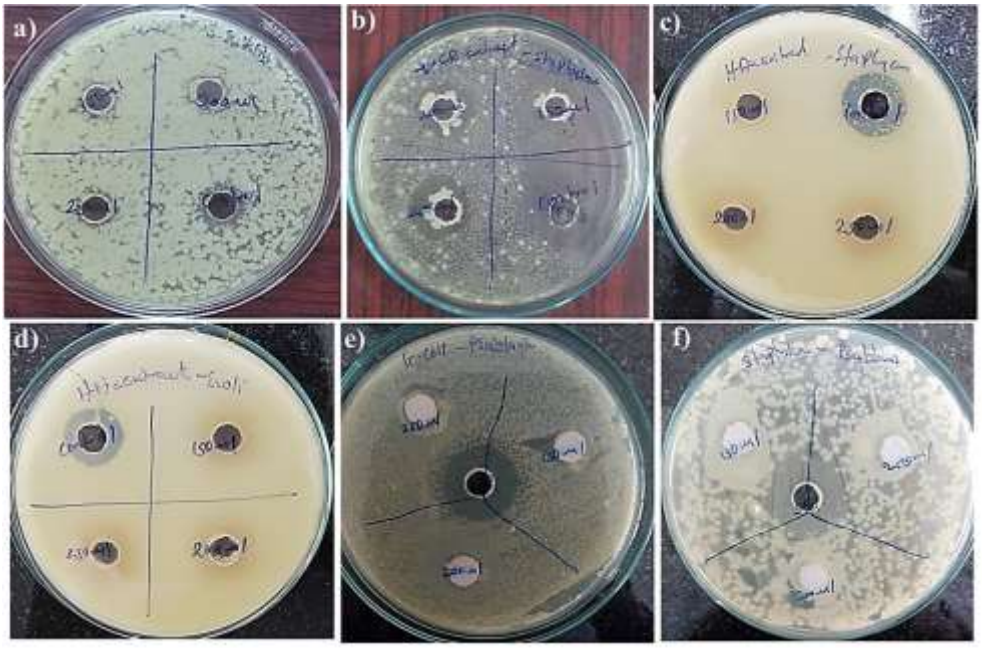

Figure 35a-f. Photographs of ZOI of CRablank, HAablank and PSablank against gram-positive and gram-negative bacteria

4.7.1.5 Comparison of antibacterial activity of synthesized nanoparticles

Compared results of bacterial inhibitory activities between prepared samples are given in **Table 25** and **Figure 36**. Prepared samples (CR, HA and PS) were grouped. The groups were compared with standard, between the groups and selected bacteria. In CR group, the maximum inhibitory activity of CRaNP was noted against *Salmonella paratyphi* (24.2 mm) and *Staphylococcus aureus* (21 mm). CRarGO shows the highest inhibition against *Salmonella paratyphi* (23.7 mm) and *Escherichia coli* (19.2 mm). CRaNC shows maximum ZOI against *Salmonella paratyphi* (20 mm) and *Escherichia coli* (16.7 mm). CRablank shows highest ZOI against *Salmonella paratyphi* (18.7 mm) and *Staphylococcus aureus* (17 mm). Synthesized gold nanoparticles using CR shows significant activity than standard and blank (CRablank). Comparing the results, the prepared gold nanoparticles using *Cyperus rotundus* showing good inhibition activity against all bacteria due to the presence of phytoconstituents of CRablank which enhance the inhibition activity of gold nanoparticles with lesser size (10-20 nm).

Table 25. Comparison between zone of inhibition of prepared samples

S.No	Samples/Groups	Zone of Inhibition in diameter (mm)			
		Escherichia coli	***Staphylococcus aureus***	***Salmonella paratyphi***	***Bacillus subtilis***
1	**CR**				
1.1	CRaNP	19.7	21	24.2	19.5
1.2	CRarGO	19.2	17.2	23.7	17.5
1.3	CRaNC	16.7	14.7	20	14
1.4	CRablank	14	17	18.7	8
1.5	Standard	11.2	23	12.5	10
2	**HA**				
2.1	HAaNP	19	19	16	17
2.2	HAarGO	16	15	17	15
2.3	HAaNC	16	20	14	17
2.4	HAablank	15	16	9	14
2.5	Standard	15	16	15	15
3	**PS**				
3.1	PSaNP	18	16	14	18
3.2	PSablank	16	19	11	10
3.3	Standard	22	22	20	21

HAaNP showed maximum inhibition (19 mm) action in the HA group against *Escherichia coli* and *Staphylococcus aureus*. HAarGO reveals ZOI of 17 mm against *Salmonella paratyphi*. The combination of HAaNP and HAarGO in HAaNC shows the

highest ZOI against *Staphylococcus aureus* (20 mm) than other bacteria. HAablank showed less inhibition activity than HAaNP, HAarGO and HAaNC. HAablank shows the maximum inhibition of 16 mm against *Staphylococcus aureus*. PSaNP shows the maximum zone of inhibition 18 mm against *Escherichia coli* and *Bacillus subtilis*. PSablank showed the highest ZOI 19 mm against *Staphylococcus aureus* and 16 mm against *Escherichia coli* but shows less inhibition against other bacteria.

The zone of inhibition was observed against selected bacteria by treating the prepared samples with bacteria. The order of major inhibitory action on bacteria are given below:

Escherichia coli **:** CRaNP > CRarGO > HAaNP > PSaNP > CRaNC

Staphylococcus aureus **:** CRaNP > HAaNC > PSablank, HAaNP > CRarGO

Salmonella paratyphi **:** CRaNP > CRarGO > CRaNC > CRablank > HAarGO

Bacillus subtilis **:** CRaNP > PSaNP > CRarGO > HAaNP, HAaNC

The order of inhibition zones between groups of AuNPs, rGO and AuNPs-rGO composite are classified below. Among all the sample's, gold nanoparticles show more inhibition against all bacteria. CRaNP and CRarGO show the highest inhibition against all bacteria than other gold nanoparticles and reduced graphene oxide.

Escherichia coli**,** ***Staphylococcus aureus*****,** ***Salmonella paratyphi***

CRaNP > HAaNP > PSaNP; CRarGO > HAarGO; CRaNC > HAaNC

Bacillus subtilis

CRaNP > PSaNP > HAaNP; CRarGO > HAarGO; HAaNC > CRaNC

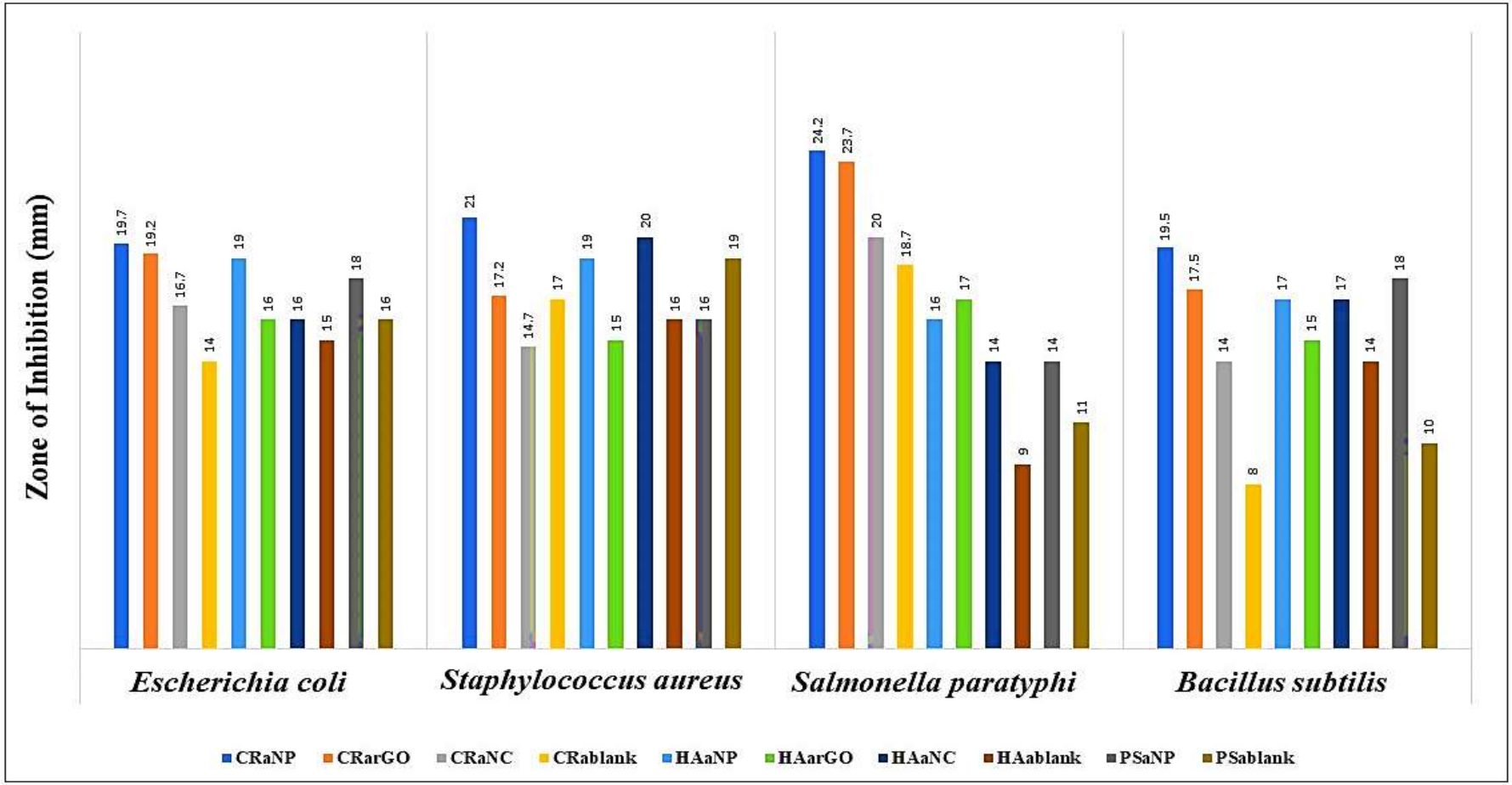

Figure 36. Graphical representation of comparisons of inhibition zone of prepared samples

The results of the antibacterial activity of prepared samples show good inhibition activity against two gram-negative (*Escherichia coli* and *Salmonella paratyphi*) and two gram-positive (*Staphylococcus aureus* and *Bacillus subtilis*) bacteria. The results of this study reveal the significant antibacterial potential of the prepared AuNPs, rGO and AuNPs-rGO composite. In this study, prepared AuNPs show higher ZOI than rGO and AuNPs-rGO composite. The higher inhibition occurs by the rise of metal ions from the surface of gold nanoparticles and penetrates through the bacteria cell membrane due to its nano-size compared to rGO. The accumulation of nanoparticles in the cell membrane leads to cell metabolism disorder, release toxic elements while gold nanoparticles are trapped in biofilm, and finally attain complete cell death **(Syukri *et al*., 2020)**. Hence the less interaction of rGO and composite with bacteria is responsible for this minimum ZOI. This less interaction may be due to the larger size of rGO and less rate of release of rGO and composite.

4.7.2 Anticancer potential of prepared AuNPs, rGO and AuNPs-rGO composite

The anticancer potential was tested for prepared gold nanoparticles (CRaNP, HAaNP and PSaNP), reduced graphene oxides (CRarGO and HAarGO), nanocomposite (CRaNC and HAaNC) and blank (CRablank, HAablank and PSablank). Doxorubicin (standard) and normal cell (HEK-293) were also tested to compare the results. In this study, the percentage of cell viability, the surface morphology of treated and untreated cells and apoptosis analysis were carried out.

4.7.2.1 MTT assay and morphometric studies of AuNPs, rGO and AuNPs-rGO composite

4.7.2.1.1 Cell viability and surface analysis of synthesized CRaNP, HAaNP and PSaNP treated A431 and HEK-293 cell lines

The cell viability of prepared gold nanoparticles is given in **Table 26**. AuNPs shows excellent toxicity against skin cancer cell line. At a lower concentration of 50 µg/mL, the prepared nanoparticles show less toxicity on both cancer and normal cells. With increases in gold nanoparticles concentration from 50 to 100 µg/mL, the maximum A431 cell viability was observed from ~90 to 30%. The percentage of cell viability of 21, 23 and 19% was observed for CRaNP, HAaNP and PSaNP against A431 respectively. At 250 µg/mL, the cell viability 67, 71, 68% on the HEK-293 cell line was observed by treating the cell line with CRaNP, HAaNP and PSaNP, respectively.

Table 26. Cell viability of synthesized CRaNP, HAaNP and PSaNP treated cell lines

S.No	Concentration (µg/mL)	Cell viability (%)					
		CRaNP		HAaNP		PSaNP	
		HEK-293	A431	HEK-293	A431	HEK-293	A431
1	50	95	96	94	93	95	93
2	100	75	32	86	39	87	33
3	150	70	28	81	33	81	31
4	200	68	26	79	27	73	25
5	250	**67**	21	**71**	23	**68**	19

Figure 37a-39a shows the concentration-dependent cell viability of gold nanoparticles treated cell lines. With an increase in the concentration of AuNPs from 50–250 µg/mL, the cell viability of skin cancer cells decreases from 96 to 21% for CRaNP, 93 to 23% for HAaNP and 93 to 19% for PSaNP. In the case of HEK-293 normal cell line, the cell viability shows 95 to 67% for CRaNP, 94 to 71% for HAaNP and 95 to 68% for PSaNP. From the lower concentration to higher concentration of AuNPs, the higher toxicity was observed in A431 skin cancer cell lines than HEK-293 normal cell lines. The samples show less-toxicity on normal cells and higher toxicity on cancer cell lines. The surface texture of nanoparticles treated normal and skin cancer cell lines are given in **Figure 37b-39b** and **Figure 37c-39c** respectively.

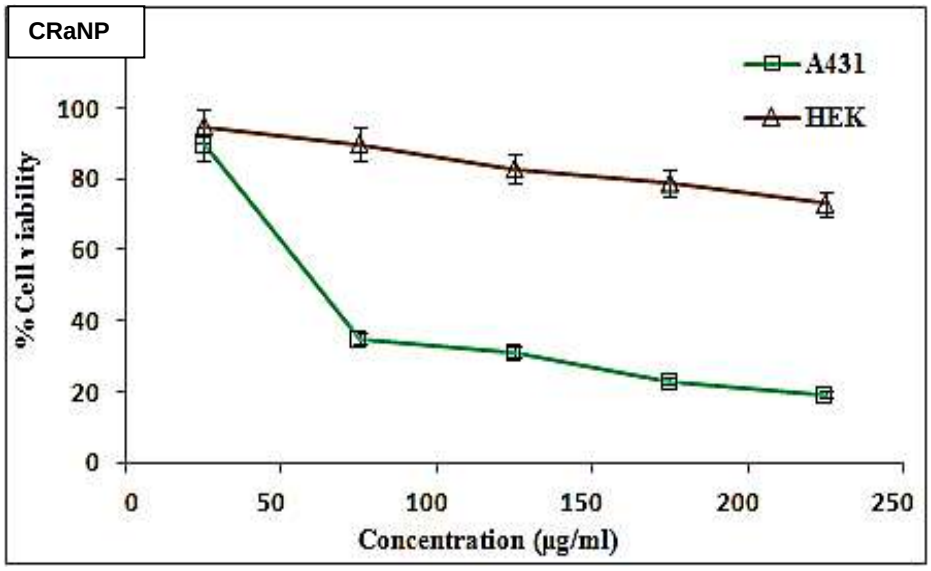

Figure 37a. Percentage of cell viability of synthesized CRaNP treated cell lines

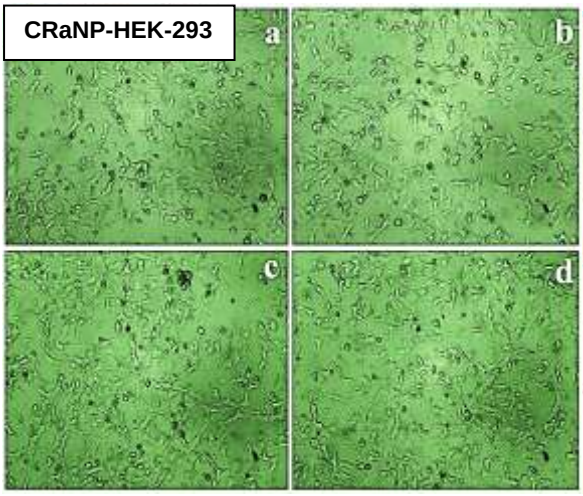

Figure 37b. Surface morphology of CRaNP treated HEK-293 cell line

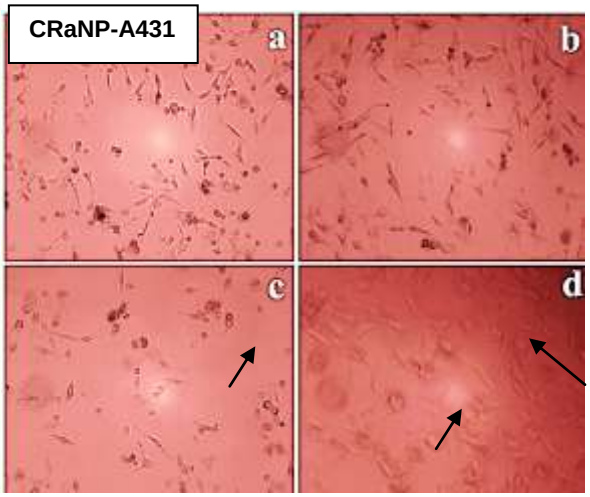

Figure 37c. Surface morphology of CRaNP treated A431 cell line

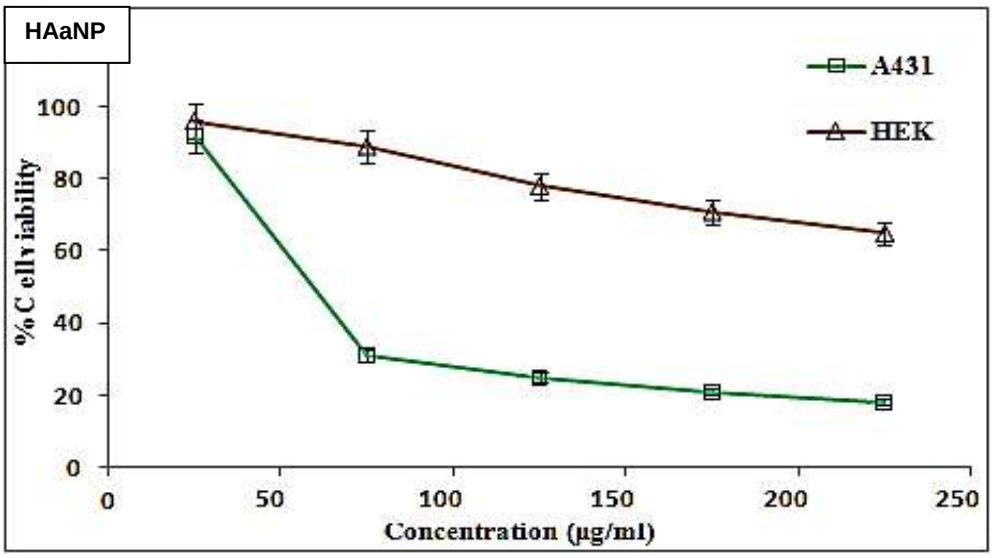

Figure 38a. Percentage of cell viability of synthesized HAaNP treated cell lines

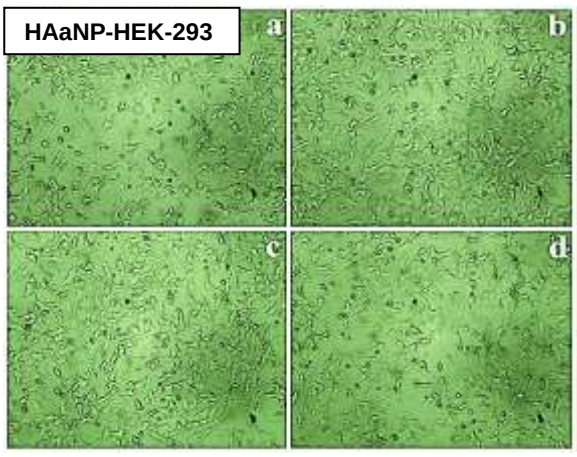

Figure 38b. Surface morphology of HAaNP treated HEK-293 cell line

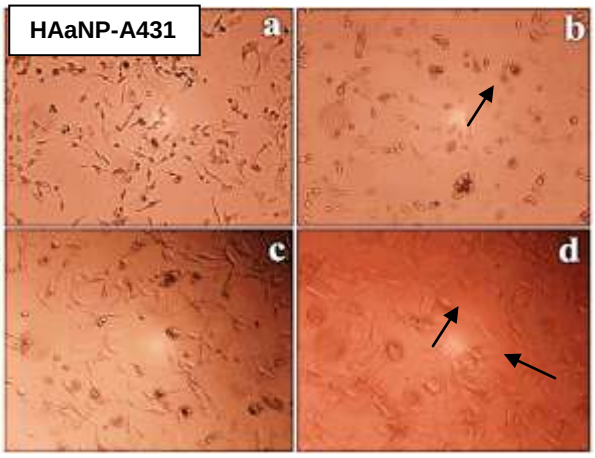

Figure 38c. Surface morphology of HAaNP treated A431 cell line

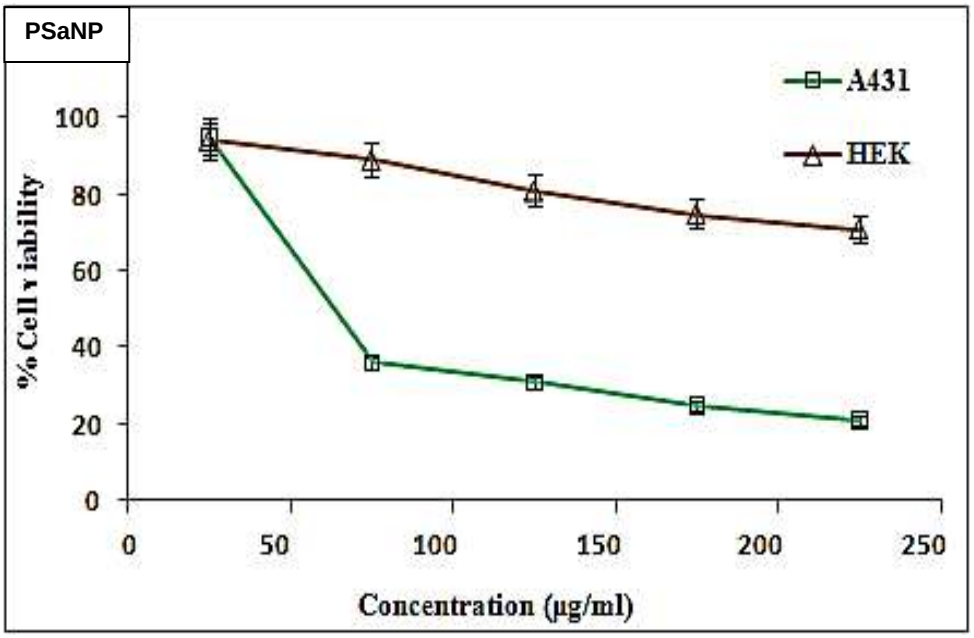

Figure 39a. Percentage of cell viability of synthesized PSaNP treated cell lines

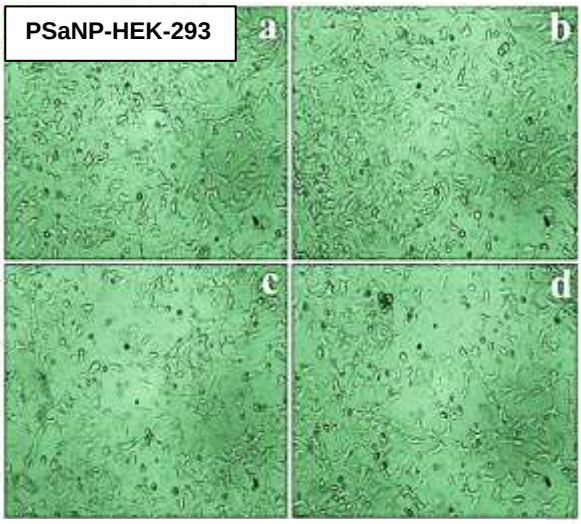

Figure 39b. Surface morphology of PSaNP treated HEK-293 cell line

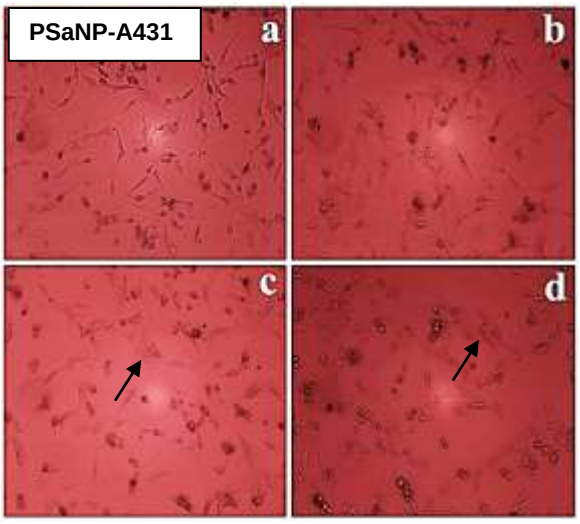

Figure 39c. Surface morphology of PSaNP treated A431 cell line

In **Figure 37b-39b** and **Figure 37c-39c,** the code (a) representing untreated normal, and cancer cell lines and b-d represents the nanoparticle treated cell lines. Morphological changes were observed in cancer cell lines after 24h treatment with dead cells. The damage in cell lines occurs by the interaction of gold nanoparticles with cell line structure which is noted by shrinkage (indicated by arrows) and death of cells in a major portion of the cell culture medium.

4.7.2.1.2 Cell viability and surface analysis of synthesized CRarGO and HAarGO treated A431 and HEK-293 cell lines

The cell viability of CRarGO and HAarGO (µg/mL) was evaluated on normal and cancer cell lines. The viability of skin cancer cell lines decreases by treating the cancer cell line with prepared reduced graphene oxide and the results are given in **Table 27**.

The percentage of cell viability of CRarGO and HAarGO shows the highest viability of 95 and 94% on HEK-293 cell lines respectively. Cell viability 90 and 95% were observed for CRarGO and HAarGO treated A431 cell lines respectively. Suddenly cancer cell death increased (~5 to 70%) by increases the concentration 50 to 100 µg/mL but this did not occur in the normal cell line. At lower concentrations, lower cell death was observed in the A431 skin cancer cell line. At higher concentration (250 µg /mL) both rGO shows excellent cancer cell inhibition activity and 81% A431 cell death observed for CRarGO and 79% for HAarGO. Less HEK-293 cell line death was observed using CRarGO (27%) and HAarGO (29%). The percentage cell viability of selected cell lines vary by varying the concentration of rGO and the results are given in **Figure 40a and 41a**.

Table 27. Cell viability of synthesized CRarGO and HAarGO treated cell lines

S. No	Concentration (µg/mL)	Cell viability (%)			
		CRarGO		HAarGO	
		HEK-293	A431	HEK-293	A431
1	50	95	90	94	95
2	100	90	35	89	36
3	150	83	31	81	31
4	200	79	23	75	25
5	250	**73**	19	**71**	21

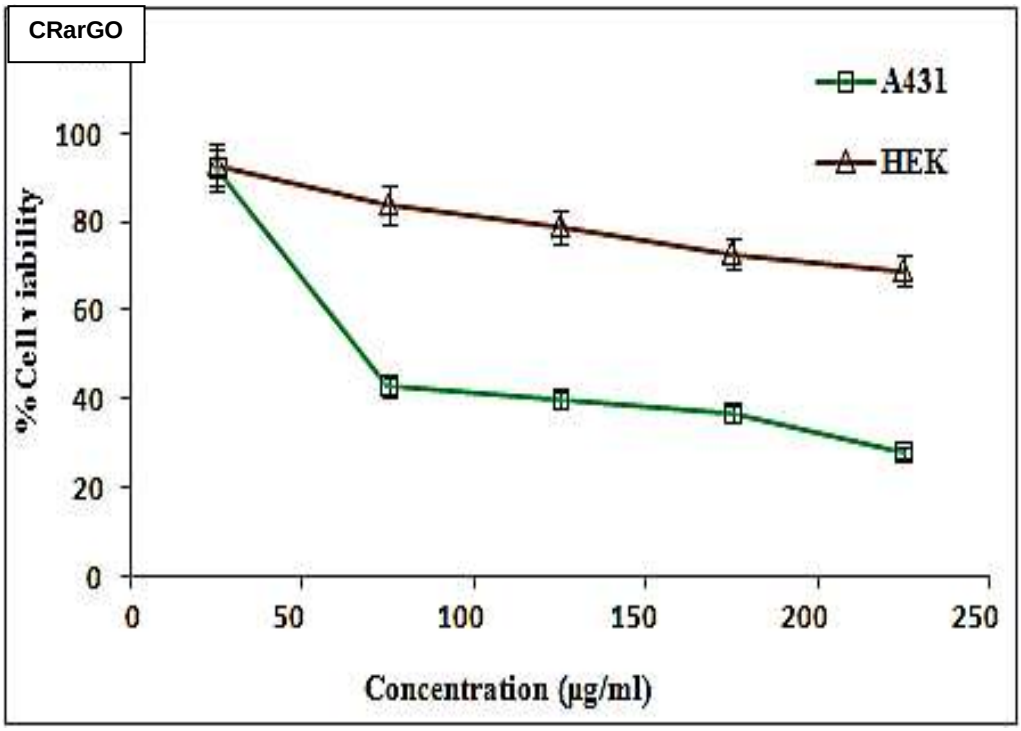

Figure 40a. Percentage of cell viability of synthesized CRarGO treated cell lines

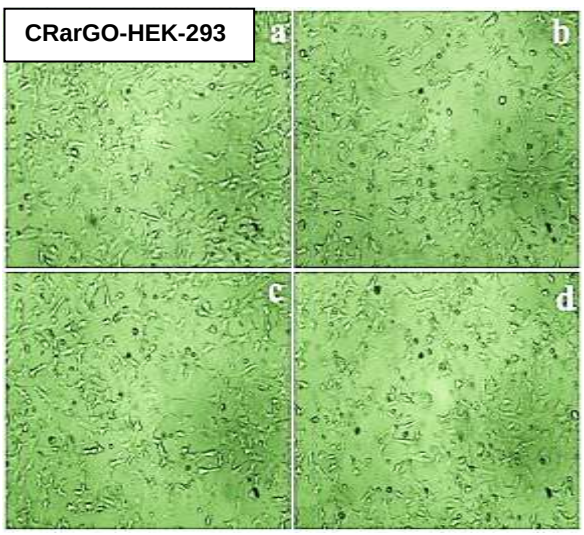

Figure 40b. Surface morphology of CRarGO treated HEK-293 cell line

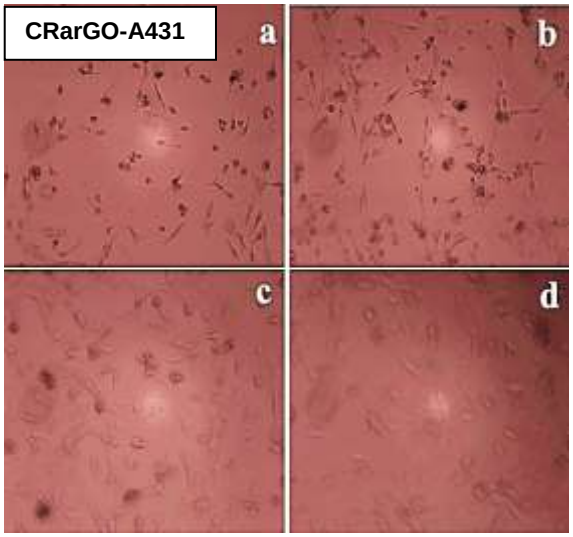

Figure 40c. Surface morphology of CRarGO treated A431 cell line

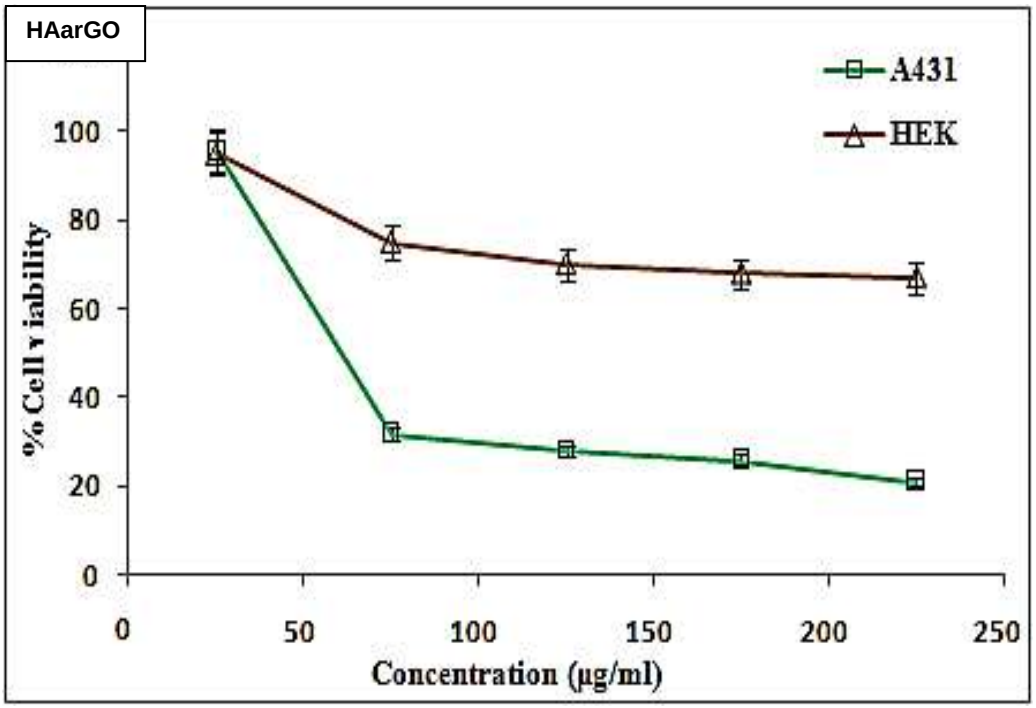

Figure 41a. Percentage of cell viability of synthesized HAarGO treated cell lines

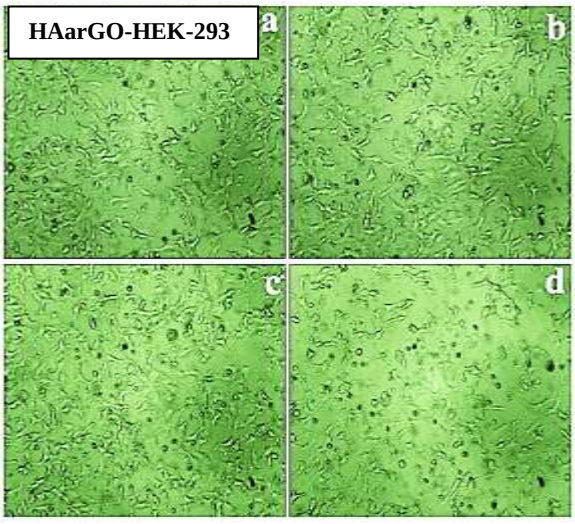

Figure 41b. Surface morphology of HAarGO treated HEK-293 cell line

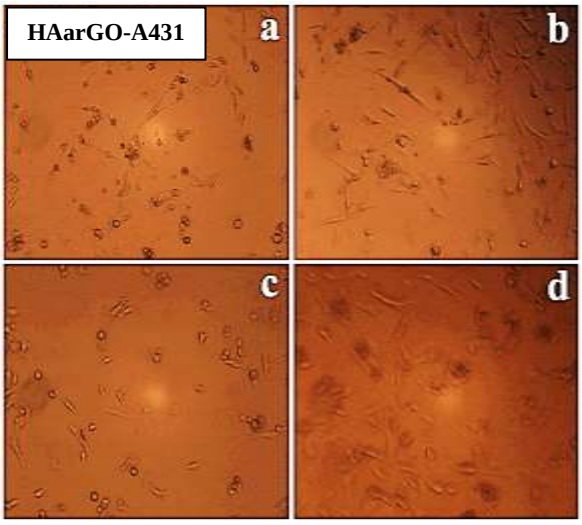

Figure 41c. Surface morphology of HAarGO treated A431 cell line

Treatment of CRarGO and HAarGO with normal cell lines shows minimum inhibition (**Figure 40b (b-d)** and **41b (b-d))**. With an increase in the concentration of the rGO, major cell deaths occur and were seen in rGO treated cancer cell lines. The cell death was confirmed by observing the shrinkage and loss of cell volume in rGO treated

A431 cell medium (**Figure 40c and 41c**). Phytoconstituents (Alkaloids, flavonoids, phenolic compounds, anthraquinone derivatives, *etc*) are naturally available bioactive compounds with anticancer potential, and it involves in increasing antioxidants, inhibiting proliferation, carcinogen inactivation, cell cycle arrest induction and involve apoptosis activity **(Amit *et al*., 2020)**. rGO also possesses excellent cytotoxicity activity against cancer cell lines. This study confirms several important constituents (discussed in 4.1) such as alkaloids, flavonoids, phenols *etc*., in CRablank and HAablank and which are embedded with prepared rGO. Hence, the phytoconstituents embed rGOs (CRarGO and HAarGO) are involved in cell damage and cell death activity in skin cancer cell lines.

4.7.2.1.3 Cell viability and surface analysis of synthesized CRaNC and HAaNC treated A431 and HEK-293 cell lines

The gold nanoparticle-reduced graphene oxide composite was tested using an MTT assay to determine the cell viability of A431 and HEK-293 cell lines. Valuable components in AuNPs and rGO create effective cell inhibition activity against A431 skin cancer cell lines. Cell viability of 92% is observed for CRaNC and HAaNC against the A431 cancer cell line. Comparing this activity, the nanocomposites show 96 and 93% cell viability on HEK-293 cells at 50 µg/mL.

At 250 µg/mL, CRaNC shows 18% cell viability (82% toxicity) and HAaNC shows 15% (85% toxicity) cell viability against A431 cell lines (**Table 28**). In the normal cell line, 65% cell viability (35% cell toxicity) was observed in CRaNC and 74% cell viability (26% cell toxicity) in HAaNC. With an increase in the concentration of nanocomposites of CRaNC and HAaNC, the viability decreases for both cell lines, as shown in Figures **42a and 43a**. This graph shows a decrease in cell viability against A431 skin cancer cell lines and sequential changes observed in HEK-293 cell lines. The morphological changes of cell shrinkage, damages and cell loss were observed in **Figures 42b-c and 43b-c**.

Table 28. Cell viability of synthesized CRaNC and HAaNC treated cell lines

S. No	Concentration (µg/mL)	Cell viability (%)			
		CRaNC		HAaNC	
		HEK-293	A431	HEK-293	A431
1	50	96	92	93	92
2	100	89	31	87	43
3	150	78	25	81	25
4	200	71	21	79	19
5	250	**65**	18	**74**	15

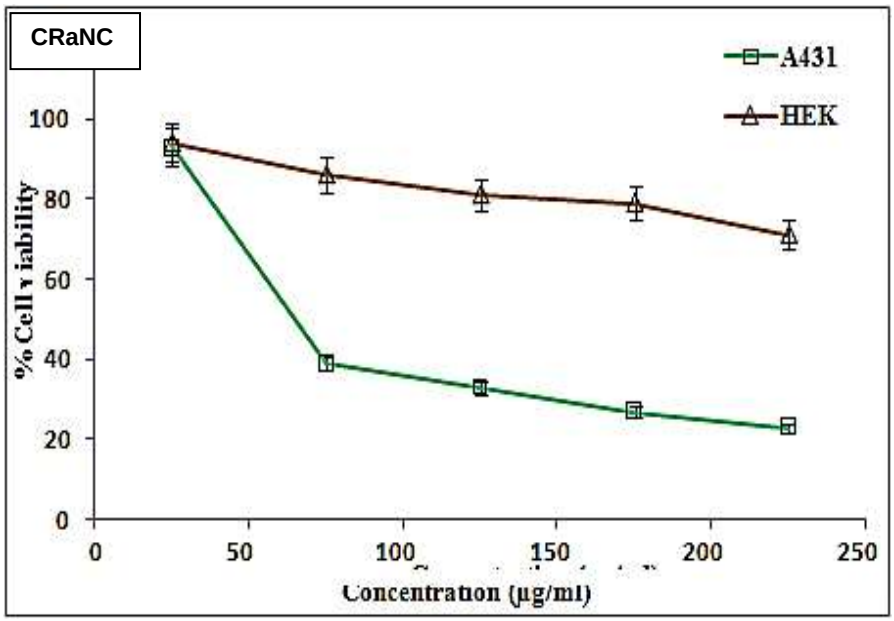

Figure 42a. Percentage of cell viability of synthesized CRaNC treated cell lines

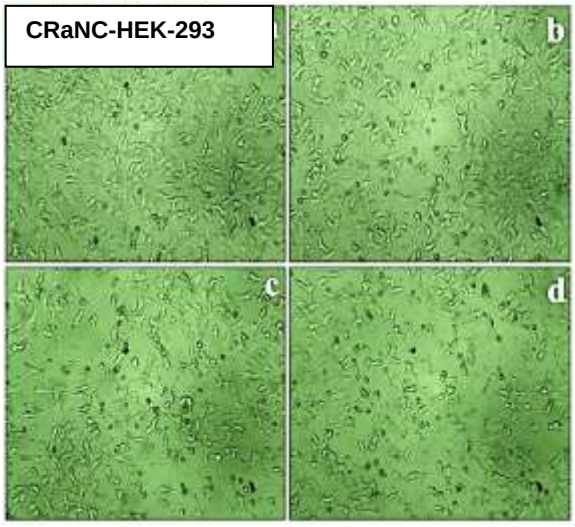

Figure 42b. Surface morphology of CRaNC treated HEK-293 cell line

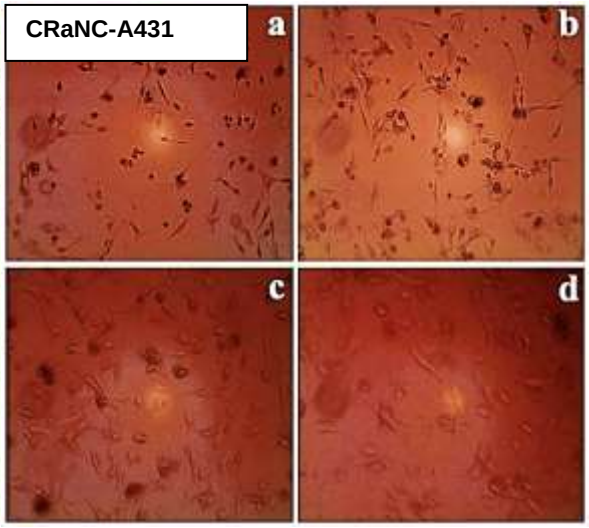

Figure 42c. Surface morphology of CRaNC treated A431 cell line

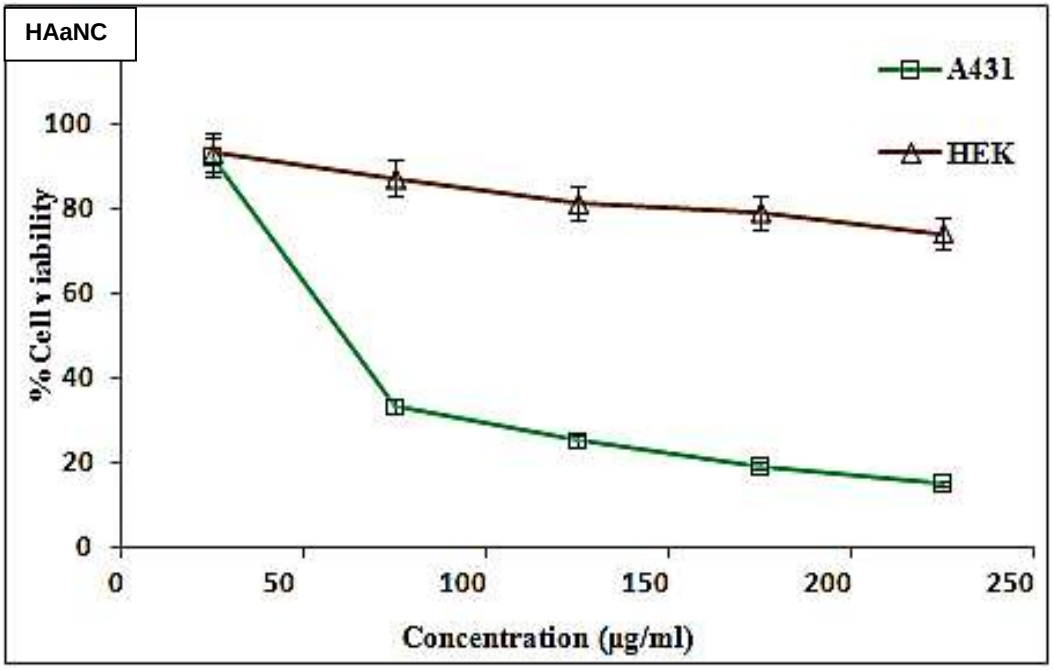

Figure 43a. Percentage of cell viability of synthesized HAaNC treated cell lines

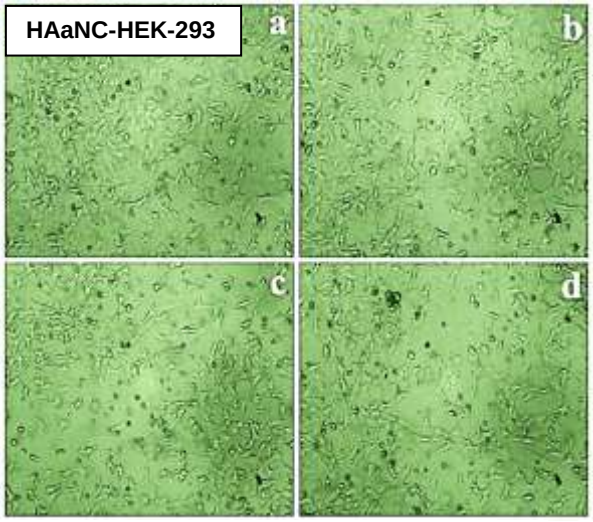

Figure 43b. Surface morphology of HAaNC treated HEK-293 cell line

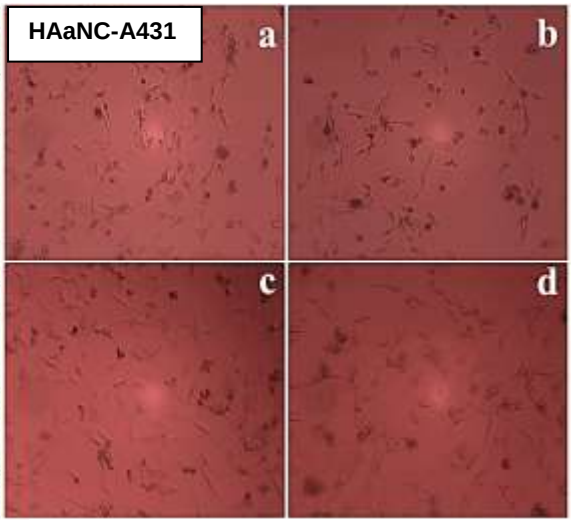

Figure 43c. Surface morphology of HAaNC treated A431 cell line

4.7.2.1.4 Cell viability and surface analysis of synthesized CRablank, HAablank and PSablank treated A431 and HEK-293 cell lines

The cell viability of CRablank, HAablank and PSablank were tested and compared with prepared nanoparticles. CRablank, HAablank and PSablank show significant toxicity on skin cancer and normal cell lines (**Figure 44a-46a**). Comparatively, the blank samples show less toxicity against both cell lines. The percentage cell viability of CRablank, HAablank and PSablank treated selected cell lines are given in **Table 29**.

Table 29. Cell viability of synthesized CRablank, HAablank and PSablank treated cell lines

S. No	Concentration (µg/mL)	Cell viability (%)					
		CRablank		HAablank		PSablank	
		HEK-293	A431	HEK-293	A431	HEK-293	A431
1	50	93	92	95	96	95	91
2	100	58	56	70	64	68	65
3	150	55	49	42	38	53	51
4	200	48	41	40	38	45	43
5	250	**31**	36	**32**	27	**33**	34

CRablank treated HEK-293 cell lines shows 93% viability at 50 µg/mL. HAablank and PSablank treated HEK-293 cell lines shows 95% viability at lower concentration (50 µg/mL). The percentage of cell viability 92, 96 and 91 were observed at 50 µg/mL on skin cancer cell lines using CRablank, HAablank and PSablank, respectively. The cell viability started to decreases by the concentration increase from 50–250 µg/mL. At higher concentrations (250 µg/mL) CRablank, HAablank and PSablank showed 31, 32 and 33% against HEK-293 cell lines, respectively. The cell viability of 36% (64% toxicity), 27% (73% toxicity) and 34% (66% toxicity) against the skin cancer cell line (A431) was observed for CRablank, HAablank and PSablank, respectively.

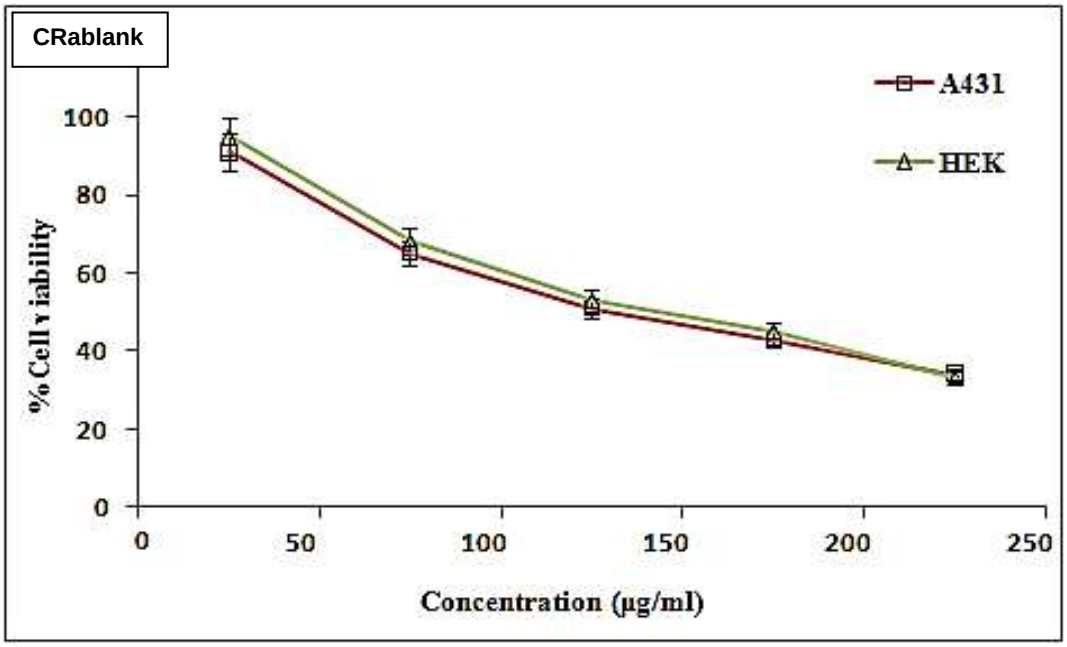

Figure 44a. Percentage of cell viability of CRablank treated cell lines

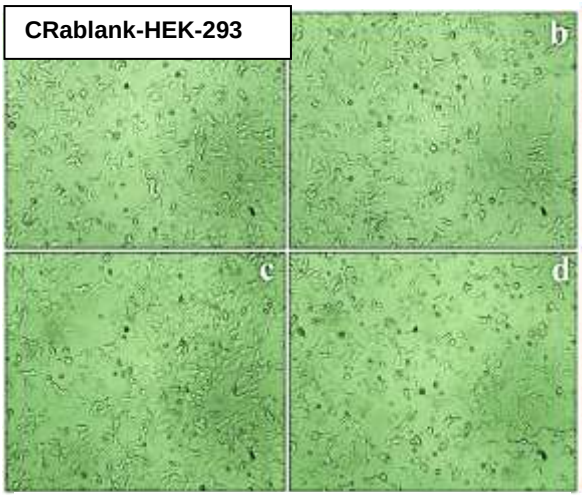

Figure 44b. Surface morphology of CRablank treated HEK-293 cell line

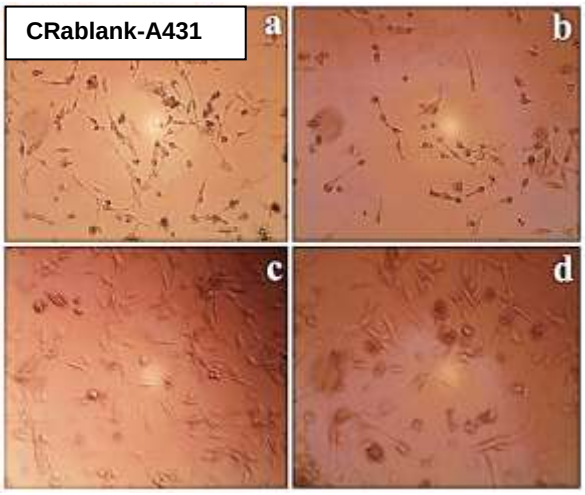

Figure 44c. Surface morphology of CRablank treated A431 cell line

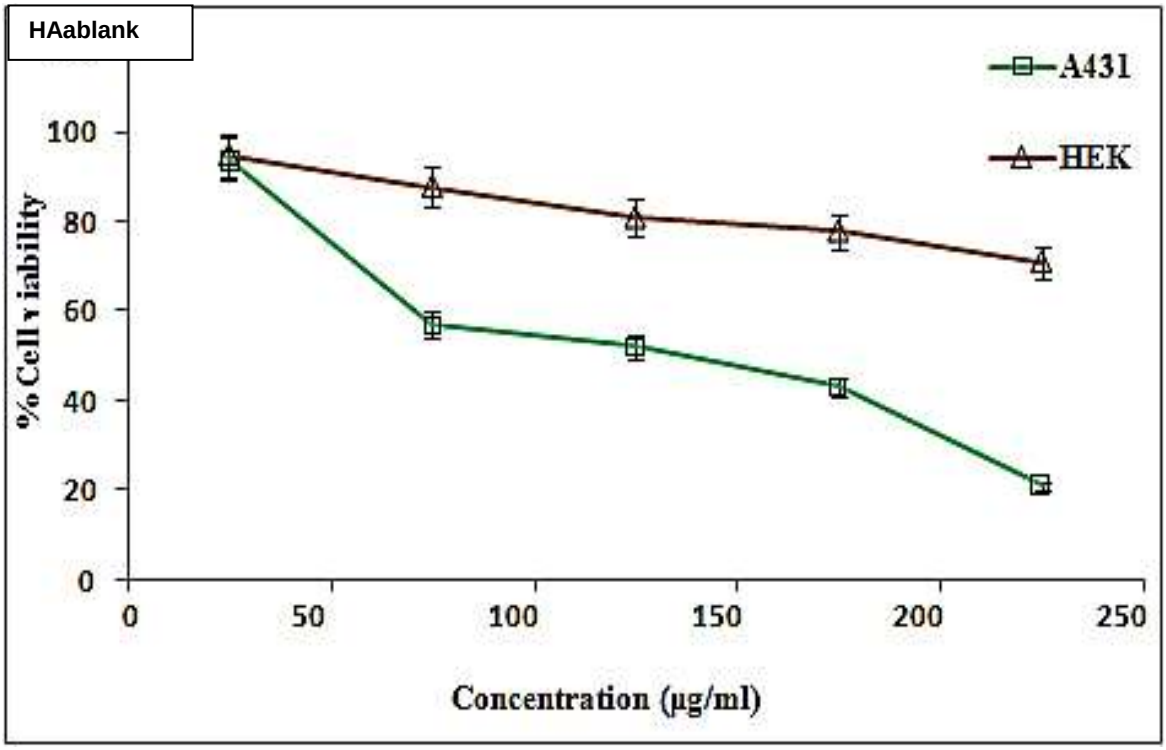

Figure 45a. Percentage of cell viability of HAablank treated cell lines

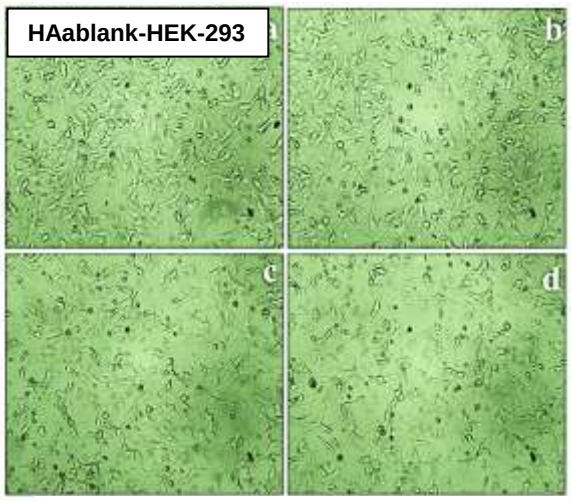

Figure 45b. Surface morphology of HAablank treated HEK-293 cell line

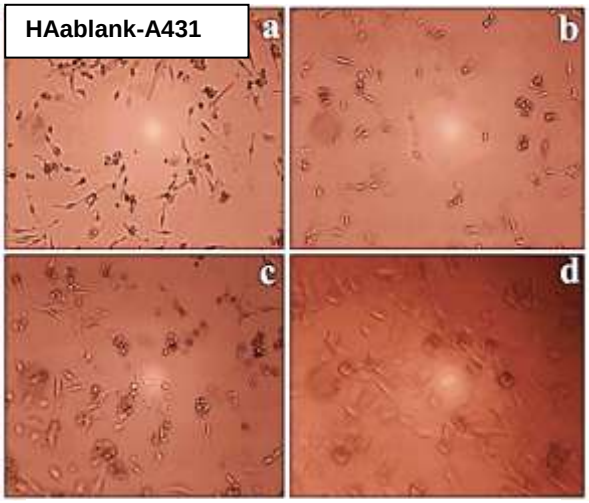

Figure 45c. Surface morphology of HAablank treated A431 cell line

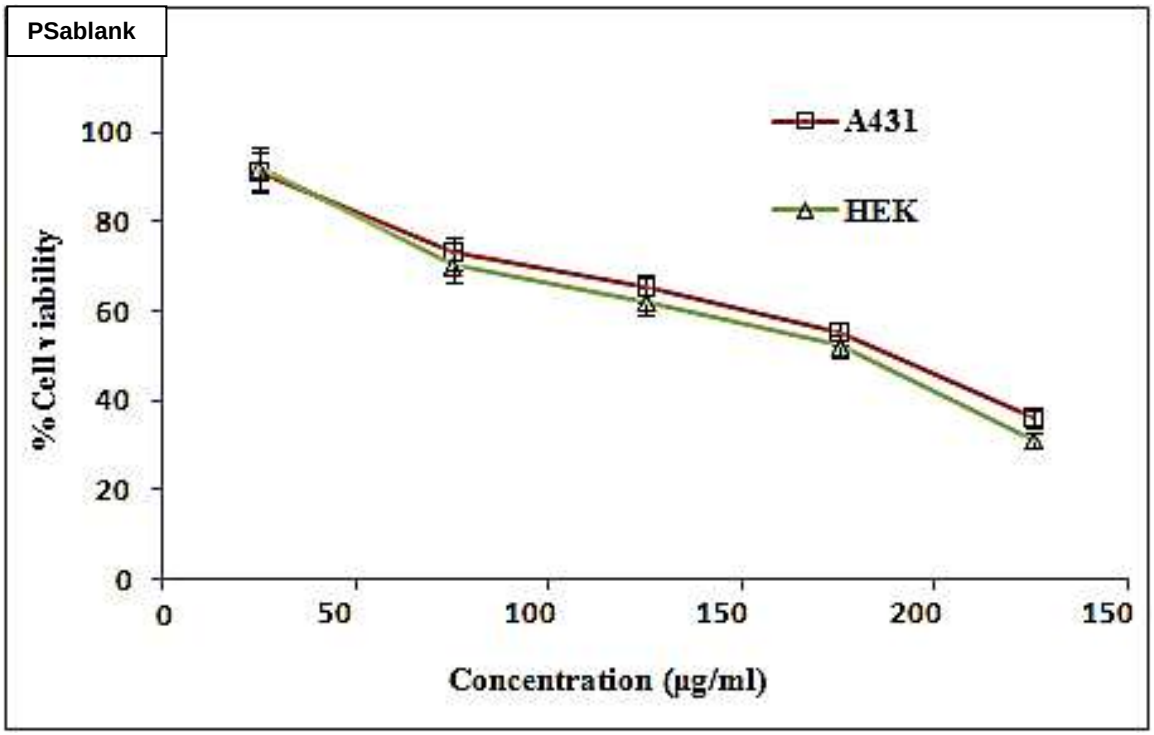

Figure 46a. Percentage of cell viability of PSablank treated cell lines

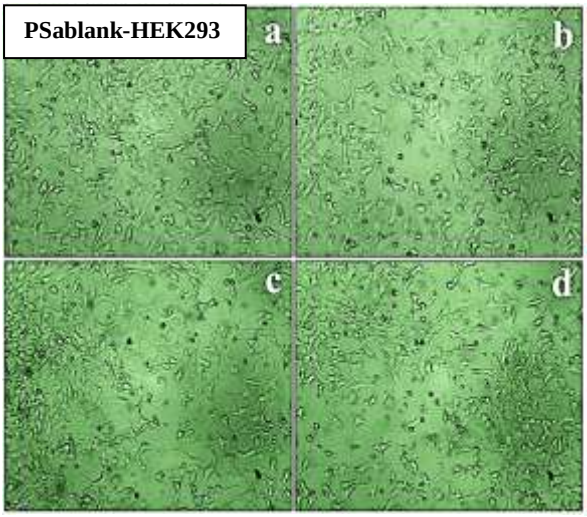

Figure 46b. Surface morphology of PSablank treated HEK-293 cell line

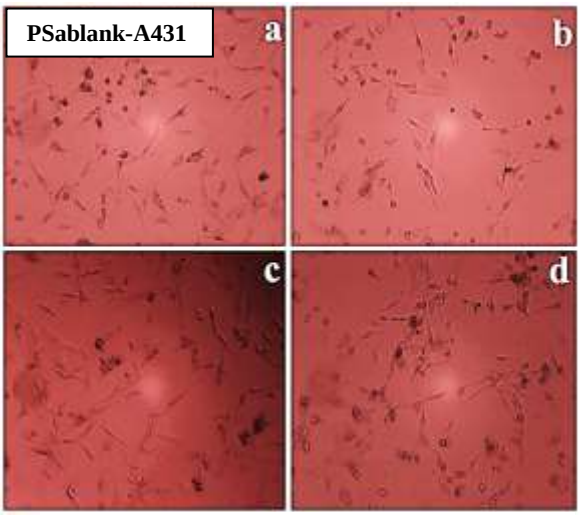

Figure 46c. Surface morphology of PSablank treated A431 cell line

The surface texture of CRablank, HAablank and PSablank treated normal cell lines clearly shows minimum cell death (**Figure 44b-46b**). Loss of cells and shrinkages were observed in samples treated with skin cancer cell lines (A431) and given in **Figure 44c-46c**. Selected blank samples show the highest toxicity on cancer cell lines and it can promote the anticancer potential of plant embeds nanoparticles. Important phytoconstituents (mentioned in 4.1) present in the CRablank and HAablank involve in this activity. The anticancer potential of pumice stone is not proven but the pumice stone consist of several metals such as Ca, Si, Mg, Al, and Ti (discussed in 4.6.6.1) involved in the anticancer activity are evidenced in the literature. Various forms of Ca **(Son and Kim, 2017; Alice and Gregory, 2018; Elizabeth *et al*., 2019)**, Ti **(Haq *et al*., 2019)**, Si **(Molnar *et al*., 2004; Susanne *et al*., 2019)** and Mg **(Shahnaz *et al*., 2018; Elham *et al*. 2019; Sungrae *et al*., 2020)** involve in cytotoxicity activity against cancer cell lines. In this study, the presence of elements (Ca, Si, Mg, Al, and Ti) with a high amount in the pumice stone may be responsible for this cancer cell death.

4.7.2.2 Comparison of IC_{50} value of synthesized AuNPs, rGO and AuNPs-rGO composite

The *in vitro* anticancer assessment was carried out for synthesized gold nanoparticles, reduced graphene oxide and gold nanoparticles-reduced graphene oxide composite. SPSS software (17.0 version) was used for statistical calculations. The graphical representations of the IC_{50} value of the respective samples are given in **Figure 47**. Selected samples are divided into 3 groups based on the number of samples

and their nanoparticles used. Group 1- CRaNP, CRarGO, CRaNC and CRablank; Group 2 – HAaNP, HAarGO, HAaNC and HAablank; Group 3- PSaNP and PSablank.

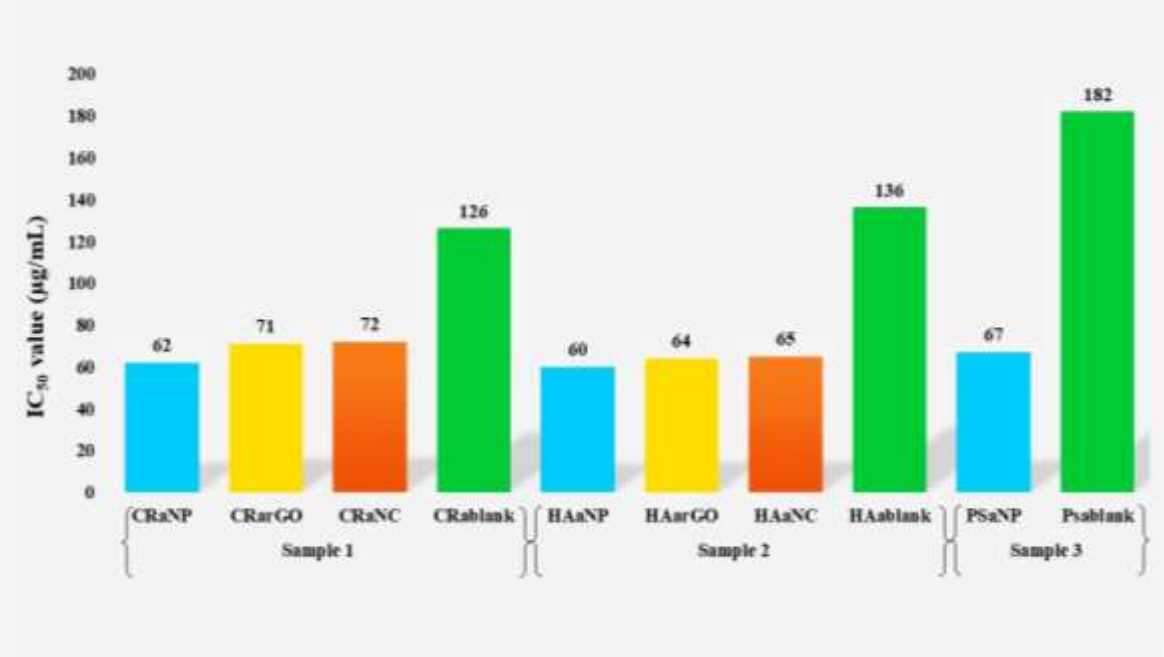

Figure 47. Graphical representation of IC_{50} value of synthesized samples against A431 cell lines

The IC_{50} values of CRaNP, CRarGO, CRaNC and CRablank were obtained at 62, 71,72 and 126 µg/mL respectively. The respective IC_{50} values 60, 64, 65 and 136 µg/mL were obtained for HAaNP, HAarGO, HAaNC and HAablank. In group 3, PSaNP shows IC_{50} at 67 µg/mL and PSablank at 182 µg/mL. In all groups, blank samples show an IC_{50} value at a higher concentration than prepared nanoparticles. Gold nanoparticles using *Cyperus rotundus*, *Hemigraphis alternata* and pumice stone showed 50% cell inhibition at a lower concentration than other samples.

4.7.2.3 Apoptotic cell Inhibition of synthesized nanoparticles

Based on the results of 4.7.2.1 and 4.7.2.2, the apoptotic cell inhibition was carried out for CRaNP, HAaNP and PSaNP using AO/EtBr and PI staining method. In apoptosis analysis changes in cell structure, cell death, cell disintegration, cell damage, cell swelling and nuclear fragmentation were noted. The detection of alive and death of cancer cells was seen in fluorescence microscopy.

4.7.2.3.1 AO/EtBr staining of gold nanoparticles treated A431 cell lines

In AO/EtBr staining, **Figure 48a (Figure 48a inside a)** indicates (given in green colour) the untreated alive skin cancer cell lines and there is no cell death observed in

untreated cell culture. With an increase in the concentration of CRaNP, HAaNP and PSaNP from 50-200 µg/mL the cell death also increased (**Figure 48a-c inside b-d)**. The changes in cell structure and cell death of the A431 cancer cell line was observed and denoted by arrows. This result confirms the initial stage of apoptotic cancer cell death.

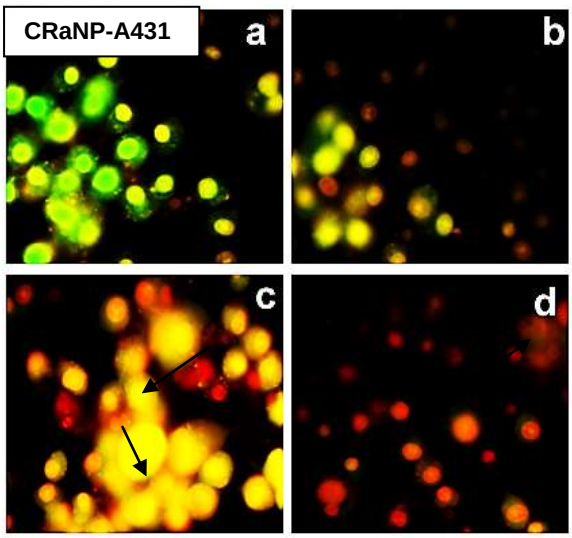

Figure 48a. AO/EtBr staining of CRaNP treated A431 cell line

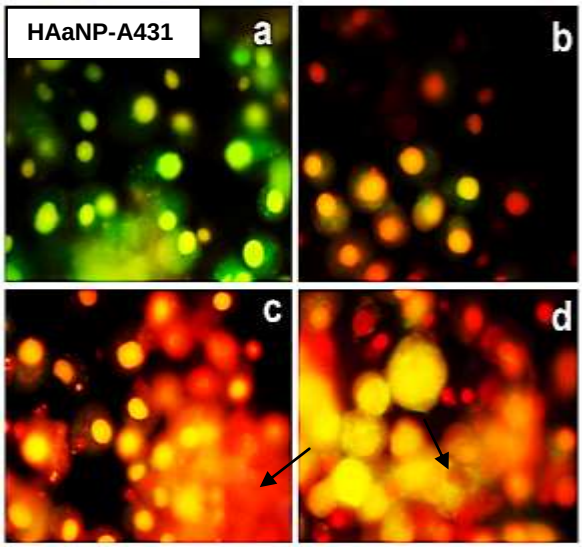

Figure 48b. AO/EtBr staining of HAaNP treated A431 cell line

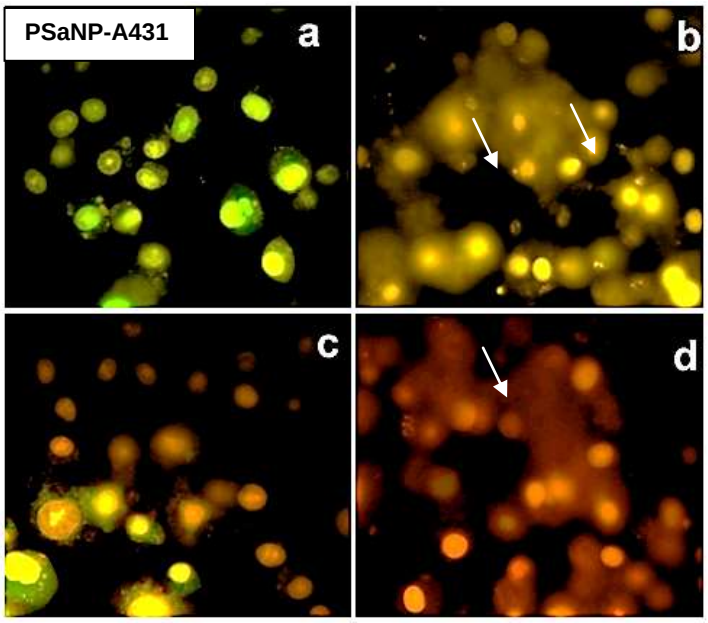

Figure 48c. AO/EtBr staining of PSaNP treated A431 cell line

Figure 48a-c. Apoptosis analysis of synthesized gold nanoparticles (CRaNP, HAaNP and PSaNP) against A431 cell line using AO/EtBr staining

4.7.2.3.2 PI Staining of gold nanoparticles treated A431 cell lines

Propidium Iodide (PI) staining is the next stage of confirmation of apoptosis cell death by the nuclear level interaction. No cell death was observed in **Figure 49a-c** (**Figure 49a-c inside a**) for the untreated cell line. Few apoptotic cell damages were noted in all cultures at a minimum concentration (**Figure 49a-c inside b**). **Figure 49a-c** (**Figure 49a-c inside c and d**) shows complete nuclear fragments in nanoparticle treated A431 cell lines indicated by arrows. The anticancer activity of CRaNP, HAaNP and PSaNP shows concentration-dependent cytotoxicity activity against skin cancer cell lines. Initially, prepared gold nanoparticles are observed on the cell surface then it attracts and penetrates through the cell membrane. The nanoparticles target the nucleus of the cells which results in fragmentation and cell death.

The inhibition efficiency of the gold nanoparticles mainly depends on the concentration **(Brocato *et al*., 2018)** and size **(Sonavane *et al*., 2008)** of the particles. The treatment efficiency increases with an increase in the amount of gold nanoparticles on the targeted cancer cells. Small-sized gold nanoparticles are capable of accumulating largely and easily than big-sized gold nanoparticles. In the present study, smaller sized gold nanoparticles (<50 nm) were obtained using *Cyperus rotundus*, *Hemigraphis alternata* and pumice stone which is confirmed using XRD and FESEM analysis. CRaNP, HAaNP and PSaNP are enhancing the anticancer activity against skin cancer (A431) cell line.

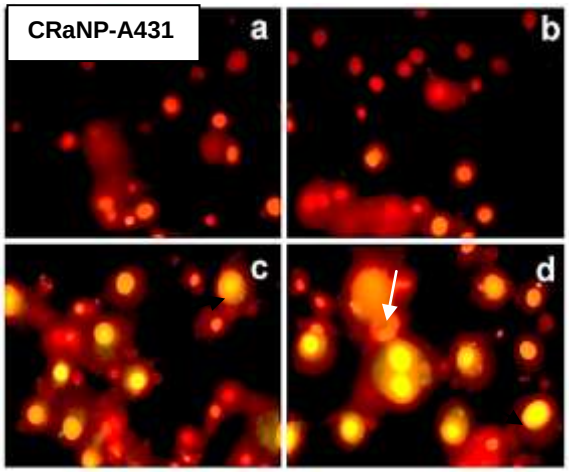

Figure 49a. PI staining of CRaNP treated A431 cell line

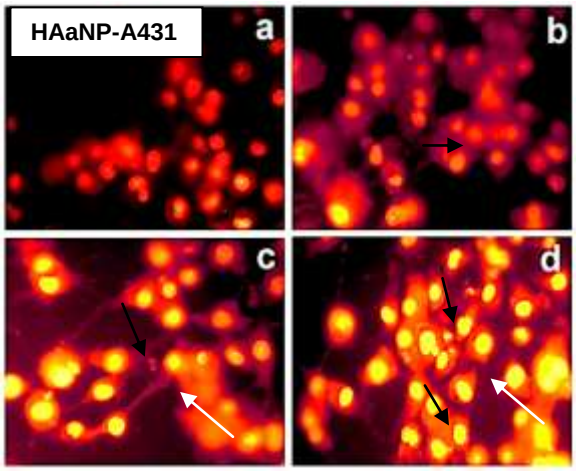

Figure 49b. PI staining of HAaNP treated A431 cell line

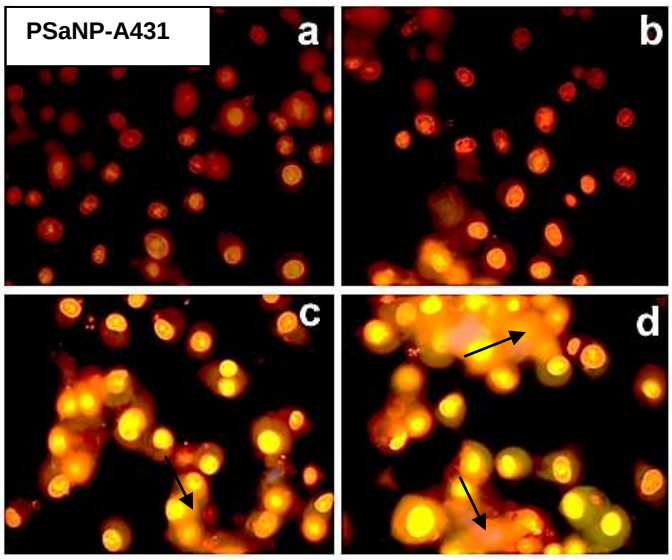

Figure 49c. PI staining of PSaNP treated A431 cell line

Figure 49a-c. Apoptosis and nuclear fragmentation of synthesized gold nanoparticles (CRaNP, HAaNP and PSaNP) against A431 cell line using PI staining

Phase II

Formulation of Depilatory Creams and Biological Activities

4.8 Standardization results of *in vitro* fabricated depilation tester

An *in vitro* depilation tester was fabricated using simple glass apparatus to measure the depilation time of hair based on **Harvey and Roberta, 1968** with some modifications. Fabricated Depilation Tester (FDT) was initially standardized with commercially available samples (Std(V) and Std (F)). The breaking time was noted with the standard time mentioned in the commercial depilatories. With an increase in the weight of commercial depilatories (Std (V) and Std (F)) from 1 to 5 mg, the depilation time decreases from 6 to 3 min. Meanwhile, the depilation time increases with the increased coated area (hair length) from 1 to 3 cm. The sample concentration of 5 mg shows the depilation time within 3 min in the minimum coated area (1 cm). FDT exactly working with the standard depilation time mentioned in commercial depilatory creams. These results reveal the depilation to depend on the concentration of cream and coating area. The triplicate results were taken.

Table 30 show the depilation activity of Std (V) and Std (F) with varying cream concentration and coating area. These results were given pictorially in **Figure 50** and

Figure 51. The overall comparison of these standardization results is represented in **Figure 52**. The FDT is a suitable *in vitro* depilation tester from this study to evaluate the depilation time of prepared depilatory samples.

Table 30. Results of depilatory action of commercially available depilatory creams in FDT

HBT-Hair Breaking Time**; HL-**Hair Length**; FDT-**Fabricated Depilation Tester; **WOC-**Weight of the Cream

S. No	HL (cm)	FDT			
		Std (V)		Std (F)	
		WOC (mg)	HBT (min)	WOC (mg)	HBT (min)
1	1	1.11 ± 0.19	4.73 ± 0.60	1.11 ± 0.09	4.15 ± 0.97
	2	1.17 ± 0.10	6.16 ± 0.80	1.13 ± 0.11	4.95 ± 0.50
	3	1.04 ± 0.02	6.85 ± 0.89	1.09 ± 0.05	5.07 ± 0.10
2	1	2.09 ± 0.16	4.16 ± 1.03	2.11 ± 0.02	4.05 ± 0.66
	2	2.17 ± 0.02	4.80 ± 0.25	2.20 ± 0.13	4.85 ± 0.81
	3	2.26 ± 0.04	5.16 ± 0.50	2.16 ± 0	4.90 ± 0.26
3	1	3.37 ± 0.24	3.45 ± 0.42	3.11 ± 0.07	3.92 ± 0.03
	2	3.09 ± 0.07	4.12 ± 0.89	3.07 ± 0.05	4.67 ± 0.61
	3	3.10 ± 0.04	4.92 ± 1.68	3.05 ± 0.05	4.70 ± 0.59
4	1	4.11 ± 0.09	3.39 ± 0.31	4.17 ± 0.08	3.70 ± 0.62
	2	4.2 ± 0.13	3.51 ± 0.94	4.08 ± 0.03	4.47 ± 0.47
	3	4.25 ± 0.18	4.1 ± 0.66	4.12 ± 0.10	4.48 ± 0.87
5	1	5.29 ± 0.09	**2.79 ± 1.41**	5.14 ± 0.15	**3.47 ± 0.46**
	2	5.25 ± 0.25	**3.00 ± 0.77**	5.08 ± 0.07	**3.78 ± 0.78**
	3	5.07 ± 0.04	**3.91 ± 1.42**	5.15 ± 0.00	**4.35 ± 0.33**

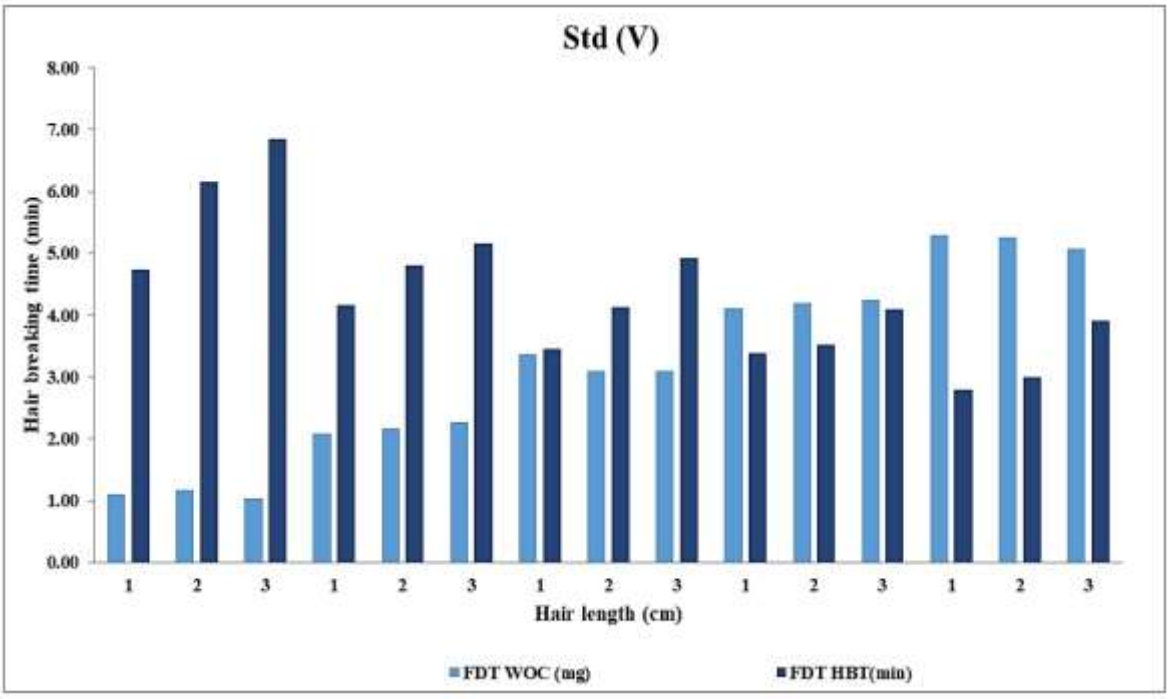

Figure 50. Graphical representation of breaking time of hair samples using Std (V) in FDT

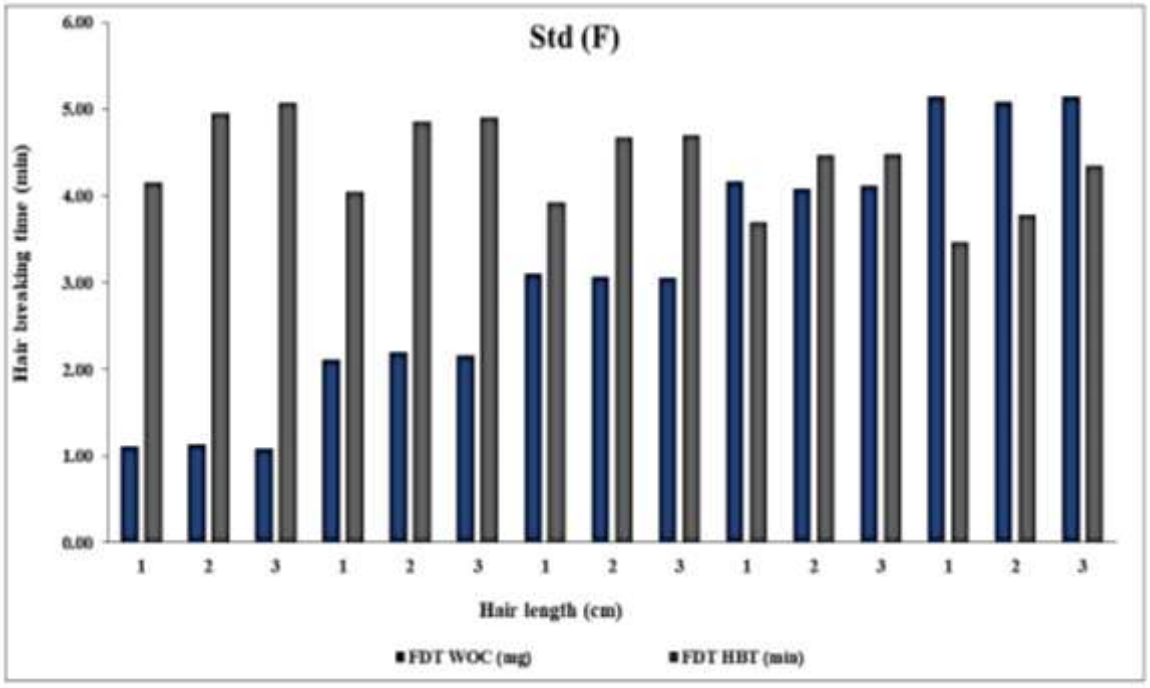

Figure 51. Graphical representation of breaking time of hair samples using Std (F) in FDT

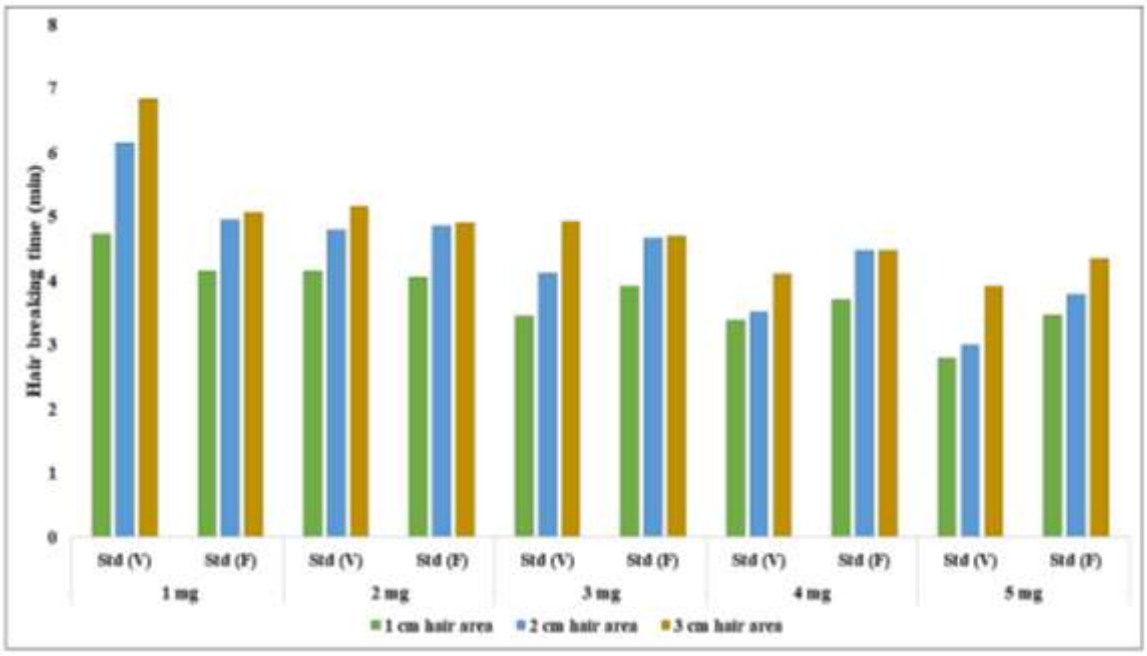

Figure 52. Comparison of depilatory action of commercially available depilatory creams Std (V) and Std (F) using FDT

4.9 Formulation of depilatory creams and testing

4.9.1 Test results of prepared depilatory creams

Depilatory creams $CAMM_2$, CAMMCRa, CAMMPSb, CAMMCRPS, CAMMCRPSHA, CAMMCRaNP, CAMMCRaNP(A) and CAMMPSaNP was prepared by the procedure mentioned in 3.10. The physical parameters such as colour, odour, appearance, pH, loss on drying, spread-ability, EDS and stability analysis was evaluated for the prepared depilatory samples, and their results are given in **Table 31**.

4.9.1.1 Test for colour and odour

Multani mitti naturally has sandalwood colour and it makes the prepared sample possess sandalwood colour. During the addition of plant extracts, the colour of CAMMCRa and CAMMCRPSHA was changed from sandalwood to brown. This colour change was not observed in other samples. The photographs of prepared depilatory samples are given in **Figure 53**.

No unpleasant odour was observed in prepared samples compared with Std (V) and Std (F). Std (V) shows an unpleasant sulphur smell, and Std (F) shows a rose petal smell, but Std (F) shows an unpleasant sulphur smell during contact with water. This unpleasant odour due to sulphur-containing compounds like salts of thioglycolates causes many health issues.

The addition of plant extracts makes the cream (CAMMCRa, CAMMCRPS, and CAMMCRPSHA) hydrated than $CAMM_2$, CAMMPSb, CAMMCRaNP, CAMMCRaNP (A) and CAMMPSaNP. This observation reveals that the plant extracts act as hydrating agents in CAMMCRa, CAMMCRPS, and CAMMCRPSHA.

Figure 53. Photographs of prepared depilatory cream samples

4.9.1.2 pH test

The pH was determined for prepared depilatory samples, and the results are given in **Table 31**. Sodium and calcium hydroxide increases the pH and lead the skin to burrow **(Park *et al*., 2019)**. Human skin can only tolerate the pH of 3.5-8.5 and depilatory cream should not exceed 12.5. Lowering the pH level of depilatories, the time of depilation also increases **(Moghimi *et al*., 2013)**. In this study, the pH of prepared depilatory samples lies between 11-12, and it is present in the recommended range.

4.9.1.3 Results of Loss on drying

The prepared samples were tested for their drying capacity by the loss on drying method. The LOD showed higher for CAMMPSb (51.4%) due to removing moisture present in the samples. This higher LOD obtained for CAMMPSb may be due to the addition of PS, which acts as a thickener in this formulation. The less LOD obtained for CAMMCRa (40%) and the LOD values of other prepared samples are given in **Table 31**. The results of this study reveal the samples showed significant LOD value and the CRablank aided depilatory samples capable of reducing the fast drying of creams and it may help maintain the cream stability.

4.9.1.4 Results of Spread-ability test

Spread-ability is one of the important factor used to differentiate the emulsifying properties of the samples **(Mettu *et al*., 2017)**. **Table 31** shows the spread-ability results by travelling area (diameter (mm)) of prepared samples. CAMMCRa (26.6 mm) showed

the highest spread-ability, and $CAMM_2$ (16 mm), CAMMPSb (16 mm) and CAMMPSaNP are (16.6 mm) showed less spread-ability than other samples. The spread-ability of prepared samples showed comparable results with the commercially available standards.

The CRa aided depilatory samples (CAMMCRa, CAMMCRPSHA, CAMMCRPS) show higher spread-ability values than Std (V) and Std (F) due to the presence of saponins in the aqueous extract of *Cyperus rotundus* tuber. Saponin is a potential emulsion stabilizer due to their surface-active properties and it exhibit high interfacial activity **(Jarzebski *et al*., 2019)**. It improves the stability of the emulsion and it also acts as surfactants or foaming agents **(Nadjia and Nadji, 2020)** because it contains both hydrophobic aglycone backbone and hydrophilic sugar molecules in their structure **(Dorota *et al*., 2017)**. During the preparation of *Cyperus rotundus* aided depilatory samples, the formation of foams was noticed due to the presence of saponins and it enhances the emulsifying properties of the prepared depilatory samples.

4.9.1.5 Results of stability tests

The centrifugation test was carried out for prepared samples to evaluate the separation of constituents from the formulation. The observation of this study reveals minimum separation of water. The visual comparison between cooling and room temperature effect for prepared samples for storing was carried out. This testing was comprised to evaluate colour, odour, and appearance for 30 days. The consolidated results of this study are given in **Table 32.** Hence, these results confirm that the sample's colour, odour, and appearance will be stable for up to 30 days.

4.9.1.6 Elemental analysis of prepared depilatory creams

The identification and mentioning the toxic metals or chemicals in hair removal products are an essential responsibility of cosmetic companies. Few hair removal products contain Cu, Cr, Co, Ni, Zn, As, Bi, Cd, Hg and Pb. These may damage the skin surface and produce rashes and allergic actions **(Qurat and Iftikhar, 2013)**.

EDS analysis of prepared samples is shown in **Figure 54a-j**. No toxic elements are seen in prepared depilatory samples. Very few percentages of Cobalt were detected in CAMMCRa, CAMMCRPS, and CAMMCRPSHA (**Figure 54d, f and g**). These may be due to the presence of *Cyperus rotundus* plant extract and it contains Cobalt. The toxicity studies of depilatory samples using *Cyperus rotundus* aqueous extract show significantly less cell inhibition on normal cell lines after 24h treatment (given in section 4.11.4). These results show that prepared samples may not show any severe toxicity on human normal

cell lines. The Std (V) and Std (F) contains a high amount of Potassium, Calcium, and Sulphur. This is due to the presence of Potassium and Calcium hydroxide and salts of thioglycolates.

The minimum amount of Sulphur (0.39%) was detected only in CAMMCRa. The detected Carbon, Silica and Sodium are due to Cetyl alcohol, Multani mitti and Sodium hydroxide in prepared samples respectively. Other metals such as Al, Mo, Fe, Mg, K and Ca be due to Multani mitti in prepared samples. The EDS analysis confirms no toxic metals in prepared depilatory samples.

Table 31. Results of testing of prepared depilatory samples

S. No	Sample code	Sample details	Colour	Odour		Appearance	pH		Loss on Drying (%)	Spread ability (mm)
				Odour	Effect		pH	T (^oC)		
1	Std (V)	Commercially available standard	Milky white	Unpleasant	Head ache	Cream	10.9	31.1	32.9±0.28	19.6±0.05
2	Std (F)	Commercially available standard	Pale pink	Rose petal	Head ache (on washing)	Cream	11.3	30	28.96±0.26	19.3±0.1
3	$CAMM_2$	Blank	Sandalwood	Ammonia with soil	Nil	Cream	11.4	29.4	47.02±8.39	16±0
4	CAMMCRa	Blank + CRa	Brown	Soil	Nil	Cream with slight liquefied	11.3	28.5	40.03±5.82	26.6±0.05
5	CAMMPSb	Blank + PS	Sandalwood	Soil	Nil	Cream	11.3	30	51.41±7.52	16±0
6	CAMMCRPS	Blank + CRa + PS	Sandalwood with brown	Soil	Nil	Cream with slight liquefied	11.3	29.3	45.6±4.94	20.6±0.2
7	CAMMCRPSHA	Blank + CRa + PS + HAa	Brown	Soil	Nil	Cream with slight liquefied	11.3	29.5	45.28±5.54	21.6±0.11
8	CAMMCRaNP	Blank + CRaNP (0.0043%)	Sandalwood	Ammonia with soil	Nil	Cream	11.4	29.2	44.78±6.5	18.3±0.05
9	CAMMCRaNP (A)	Blank + CRaNP (0.017%)	Sandalwood	Ammonia with soil	Nil	Cream	11.3	28.8	48.49±9.48	17.6±0.15
10	CAMMPSaNP	Blank + PSaNP	Sandalwood	Soil	Nil	Cream	11.3	28.9	46.42±11.1	16.6±0.05

Table 32. Testing results of prepared depilatory samples

C-**C**olour; **O**-**O**dour; **A**-**A**ppearance; **CE**-**C**ooling **E**ffect; **RTE**-**R**oom **T**emperature **E**ffect; **NC**-**N**o **C**hange; **SSW**-**S**light **S**eparation of **W**ater; **SS**-**S**mall **S**olidification; **NL**-**N**o **L**iquification; **LL**-**L**ess **L**iquification of Water, **LAS**-**L**ess **A**mmonia **S**mell

Test name		Time interval	Sample code							
			$CAMM_2$	CAMMCRa	CAMMPSb	CAMMCRPS	CAMMCRPSHA	CAMMCRaNP	CAMMCRaNP(A)	CAMMPSaNP
Centrifuge		**0**	SSW	SSW	SSW	SSW	SSW	SSW	SSW	SSW
Initial	**C**	**0**	Sandalwood	Brown	Sandalwood	Sandalwood with brown	Brown	Sandalwood	Sandalwood	Sandalwood
	O		Pleasant	Pleasant	Pleasant	Pleasant	Pleasant	Pleasant	Pleasant	Pleasant
	A		NL	LL	NL	LL	LL	NL	NL	NL
CE	**C**	**10 days**	NC	NC	NC	NC	NC	NC	NC	NC
	O		LAS	NC	NC	NC	NC	Nil	Nil	NC
	A		SSW	SSW	SSW	SSW	SSW	SSW	SSW	SSW
RTE	**C**		NC	NC	NC	NC	NC	NC	NC	NC
	O		LAS	NC	NC	NC	NC	Nil	Nil	NC
	A		SSW	SSW	SSW	SSW	SSW	SSW	Nil	Nil
CE	**C**	**20 days**	NC	NC	NC	NC	NC	NC	NC	NC
	O		LAS	NC	NC	NC	NC	NC	NC	NC
	A		SSW	SSW, LL	SS	SSW, LL	SSW, LL	SSW	SSW	SSW
RTE	**C**		NC	NC	NC	NC	NC	NC	NC	NC
	O		LAS	NC	NC	NC	NC	NC	NC	NC
	A		SSW	SSW, LL	SS	SSW, LL	SSW, LL	SSW	SSW	SSW
CE	**C**	**30 days**	NC	NC	NC	NC	NC	NC	NC	NC
	O		LAS	NC	NC	NC	NC	NC	NC	NC
	A		SSW	SSW, LL	SS	SSW, LL	SSW, LL	SSW	SSW	SSW
RTE	**C**		NC	NC	NC	NC	NC	NC	NC	NC
	O		LAS	LAS	LAS	LAS	LAS	LAS	LAS	LAS
	A		SSW	SSW, LL	SS	SSW, LL	SSW, LL	SSW	SSW	SSW

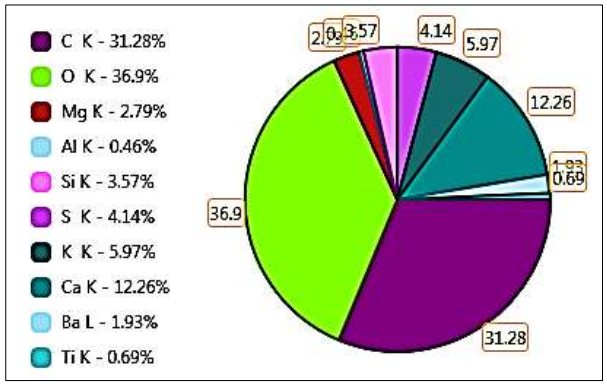

Figure 54a. EDS spectrum of Std (V)

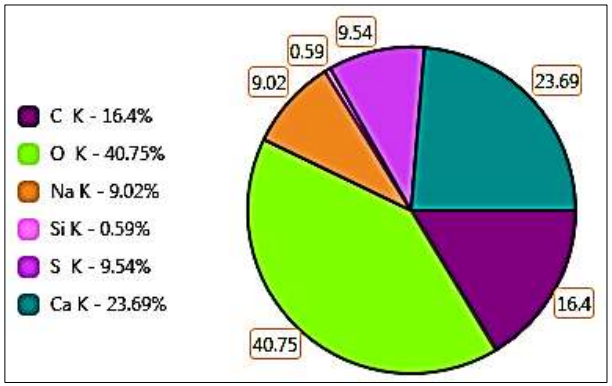

Figure 54b. EDS spectrum of Std (F)

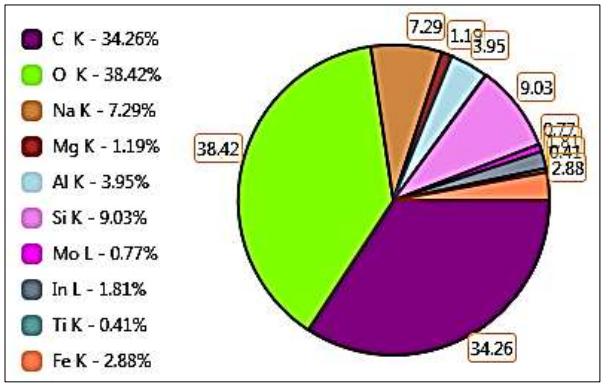

Figure 54c. EDS spectrum of $CAMM_2$

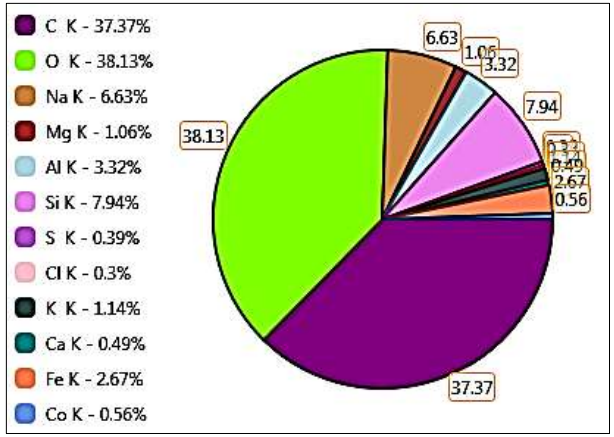

Figure 54d. EDS spectrum of CAMMCRa

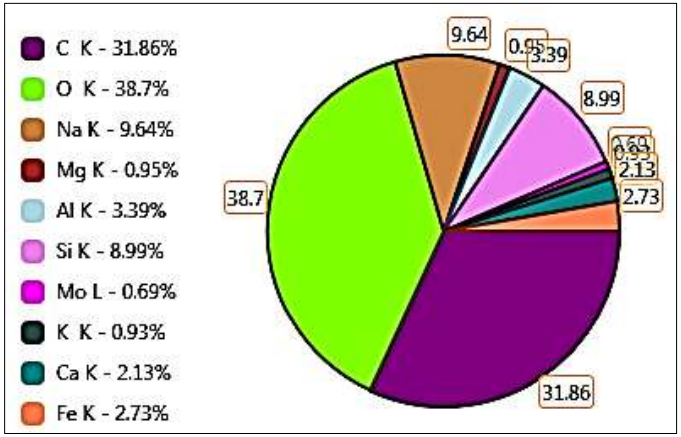

Figure 54e. EDS spectrum of CAMMPSb

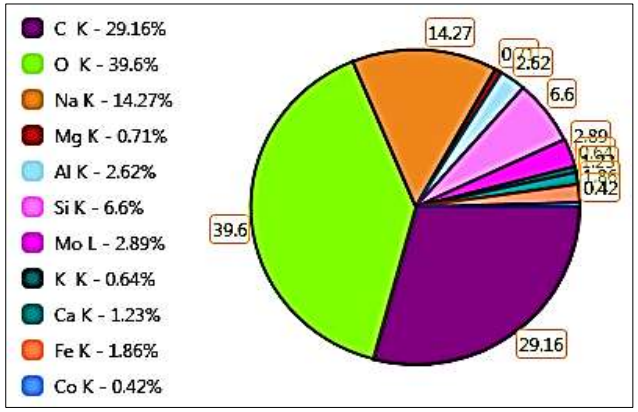

Figure 54f. EDS spectrum of CAMMCRPS

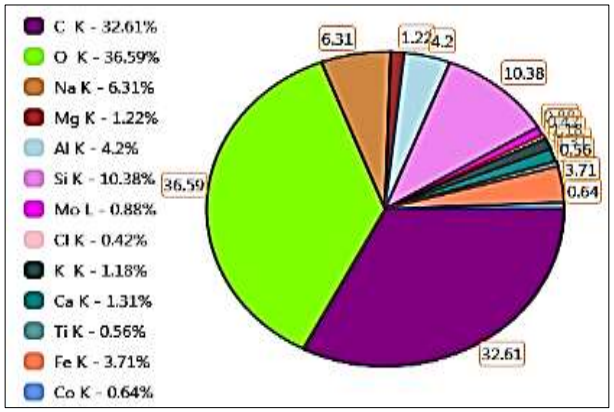

Figure 54g. EDS spectrum of CAMMCRPSHA

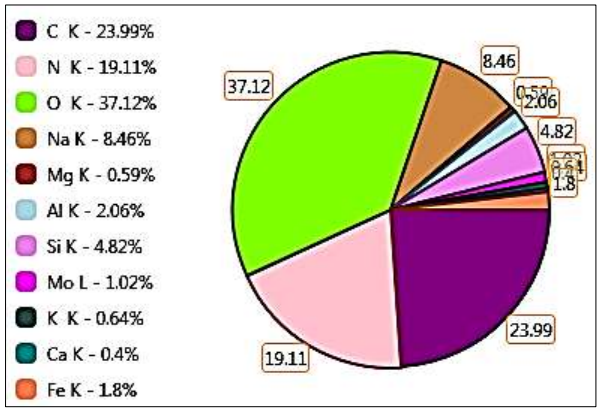

Figure 54h. EDS spectrum of CAMMCRaNP

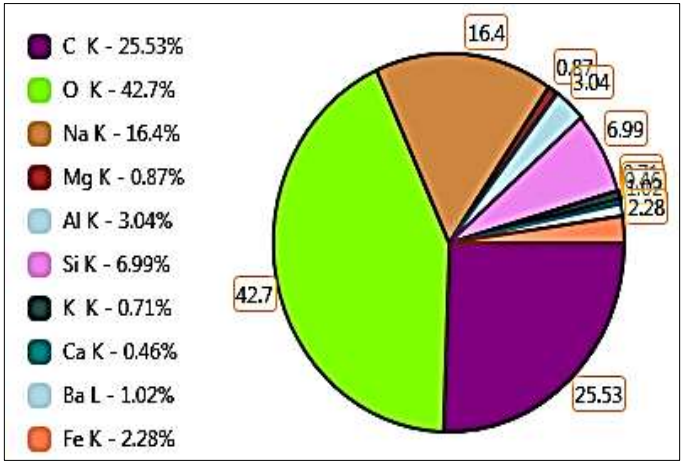

Figure 54i. EDS spectrum of CAMMCRaNP (A)

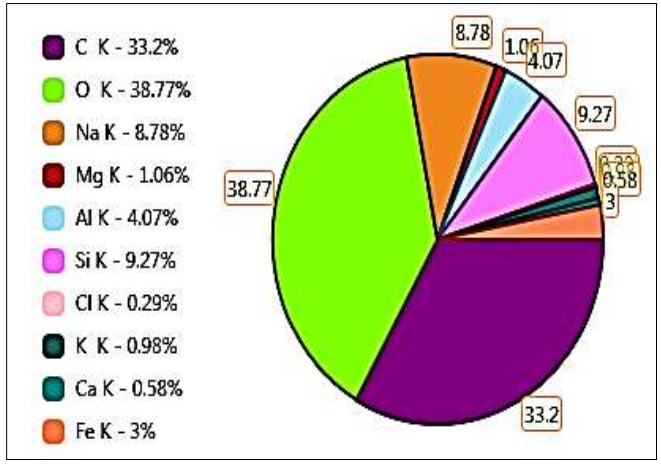

Figure 54j. EDS spectrum of CAMMPSaNP

Figure 54a-j. EDS spectrum of prepared depilatory cream samples

4.10 Results of depilation activity of prepared depilatory samples

The depilation activity of prepared samples was carried out using *in vitro* fabricated depilation tester (**Figure 55**). The commercial creams showed the depilation time between 3-6 minutes, and $CAMM_2$ showed 3-8 minutes. Plant extract and pumice stone aided samples were showed 3-6 minutes and nano-aided samples showed 3-4 minutes. The efficiency of the depilatory cream strongly depends on the hair type, colour, hair strength, hair coarseness and treatment time **(Jyothi *et al*., 2012)**. In this study, after treating depilatory samples, the hair colour changes from black into brown with shrinkages (**Figure 56**). This change indicated the weakening of hair. The hair breakdown occurred in the cream coated hair area. Depilatory creams are prepared using *Cyperus rotundus*, pumice stone and their nanoparticles enhance the hair breaking time. In this study, hair weakening (**Figure 56**) and degradation occurred without any thioglycolates or hair destroying agents and toxic chemicals.

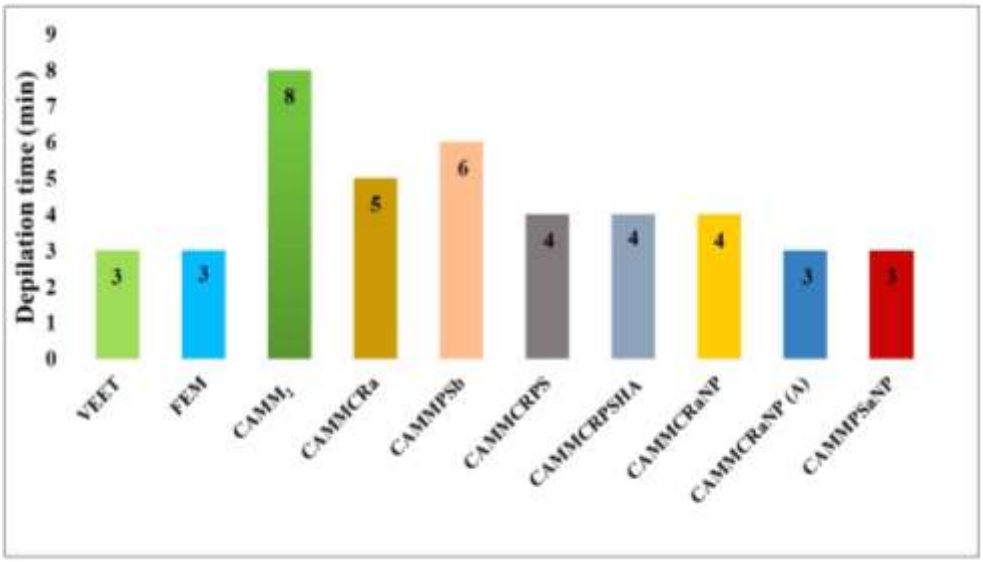

Figure 55. Breaking time of hair samples using prepared depilatories

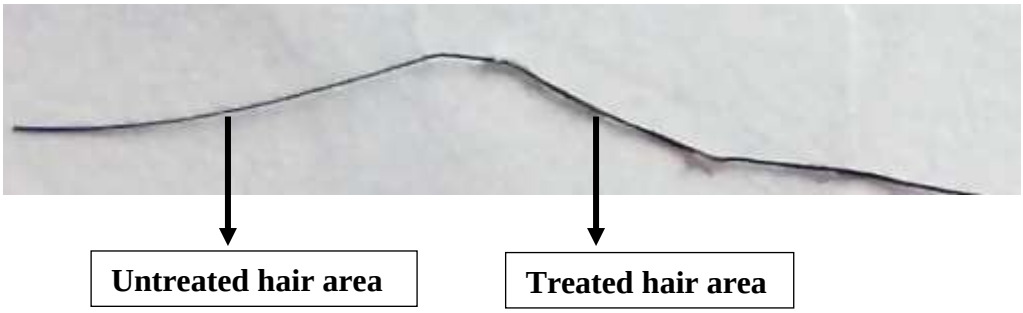

Figure 56. Photograph of prepared depilatory samples treated and untreated hair area

In this study, sodium hydroxide was used to increase the pH and weakening the hair primarily. Depilatory agents in depilatory creams are effectively involved in trans-epidermal drug delivery. This is caused by reducing the stratum corneum's resistivity, but the actual depilation mechanism remains unknown **(Lee *et al*., 2008)**.

The abrasive behaviour of pumice stone may be involved in abrasing the hair shaft resulting in breaking the hair. The gold nanoparticle contains plant embeds, and due to the larger surface area, it can easily penetrate the hair follicles and quickly weaken the hair shaft after opening the disulphide bond in cystine. This study used Multani mitti as a binding and base material, reducing the cream's toxicity.

The existence of androgen is (Androgenic hair) depends entirely on sexual hair growth. The Egyptian *Cyperus rotundus* essential oil is an active agent in axillary hair and hirsutism removal without affecting serum testosterone **(Evans *et al*., 1995)**. The essential oil in *Cyperus rotundus* contains flavonoids which are involved in the hair reduction process. The combination of *Cyperus rotundus* oil and the Alexandrite laser did not show any side effects, and it acts as an effective treatment for reducing the growth of hair (white and black) **(Ghada, 2014)**. The flavonoids of *Cyperus rotundus* involved anti-androgenic activity on Androgenic hair **(El-kaream, 2012)**.

The tuber portion of *Cyperus rotundus* contains important flavonoids such as Kaempferol, Quercetin and Myricetin (**Krishna and Renu, 2013)**. This study confirmed the presence of flavonoids in aqueous extract of *Cyperus rotundus* by phytochemical assessment test, and it may be responsible for this depilation activity of the prepared samples.

4.10.1 Results of depilation stability on cooling and room temperature condition

To compare the suitable condition to store the prepared cream samples, the following study was carried out. In this regard, the samples were kept at room temperature and refrigerator for 30 days. Every 10 days the depilation activity was tested and the results were given in **Figure 57**. The samples under room temperature reduce the depilation efficiency of the samples than refrigerated samples. At cooling conditions, the depilation changes observed a maximum 3-8 minutes but in the case of room temperature conditions, the maximum changes were observed with 3-14 minutes. The results of this study reveal the cooling condition is preferred to store prepared depilatory samples.

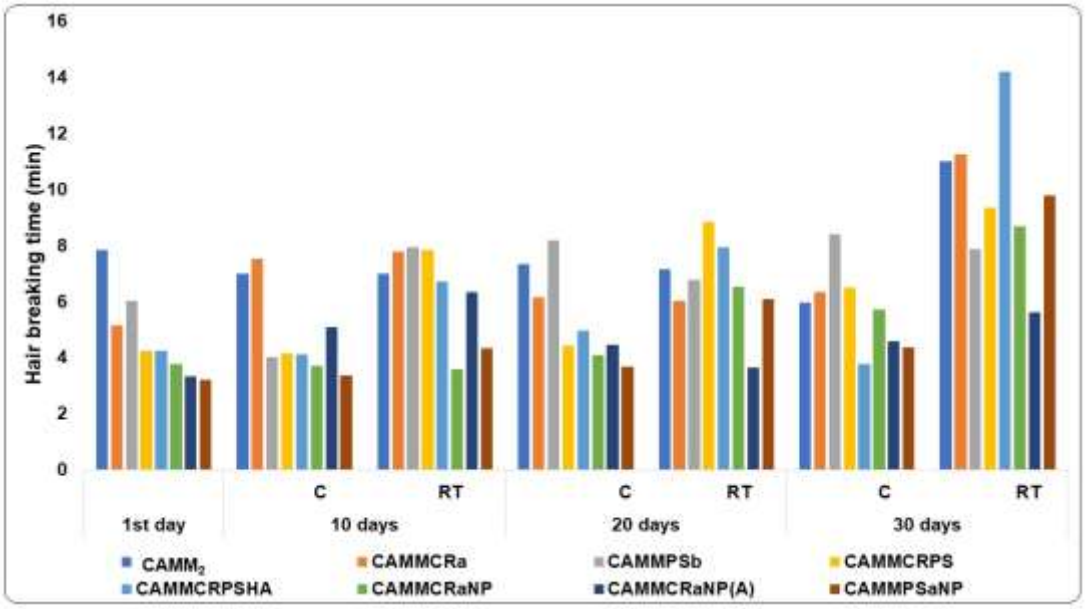

Figure 57. The changes in depilation activity of prepared depilatories under room temperature and cooling condition

4.10.2 Surface morphology of depilatories treated and untreated hair samples

The degradation of the hair samples by prepared depilatory creams was confirmed using surface morphological analysis. The FESEM analysis indicated the complete decomposition of the hair shaft. **Figures 58a, b and c, d** indicate the untreated healthy hair surfaces and their edges, respectively. **Figure 58e-g** shows the prepared depilatory samples treated hair samples. Hair damages were not noticed in untreated hair samples. Hair opening, hair breaking and complete hair damage were seen in treated hair (**Figure 59a-h**). The surface morphological study confirms the active participation of depilatory cream in the hair damage and degradation process.

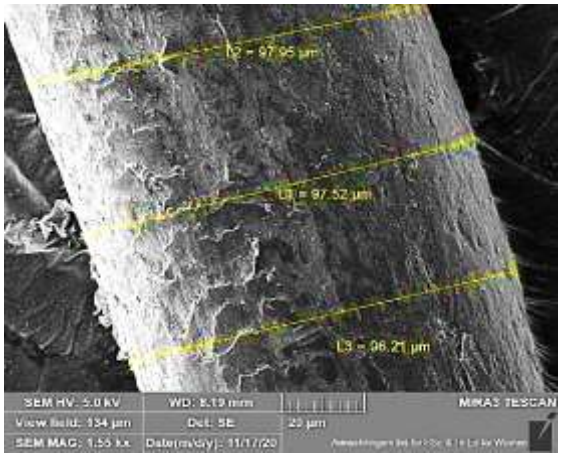

Figure 58a. FESEM image of untreated normal hair surface

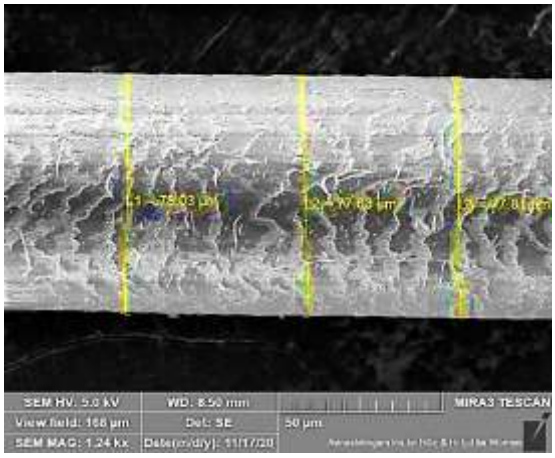

Figure 58b. FESEM image of untreated normal hair surface

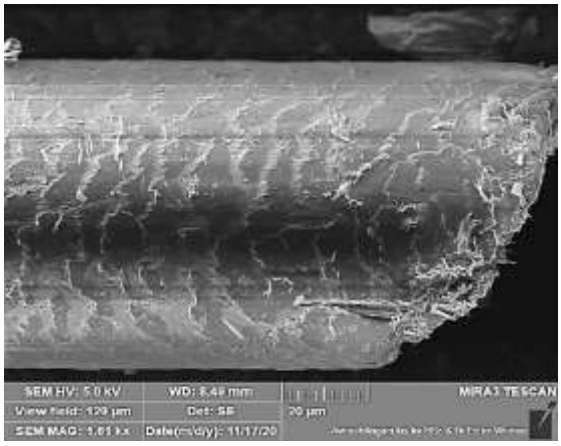

Figure 58c. FESEM image of untreated normal hair edges

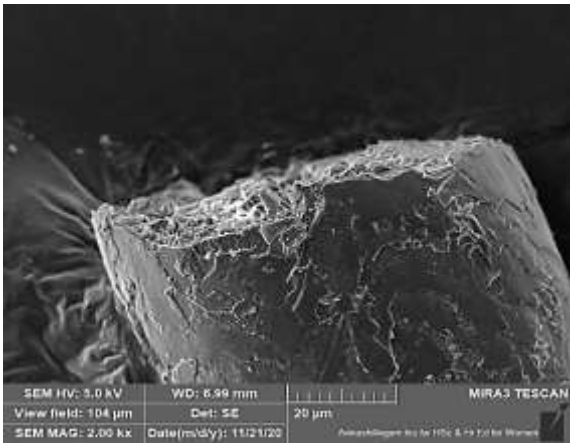

Figure 58d. FESEM image of untreated normal hair edges

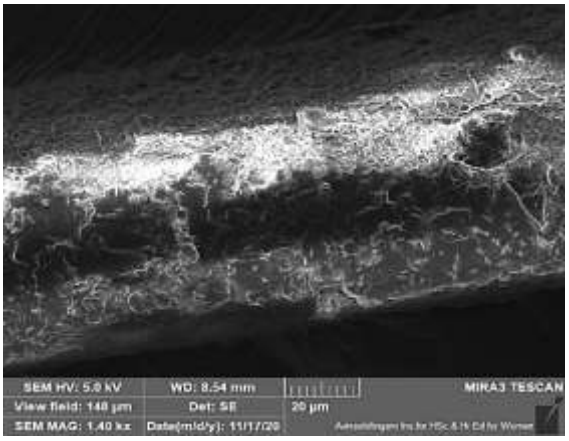

Figure 58e. FESEM image of damaged hair surface

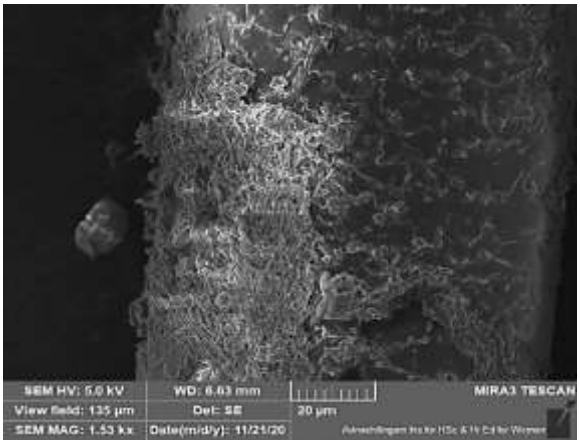

Figure 58f. FESEM image of damaged hair surface

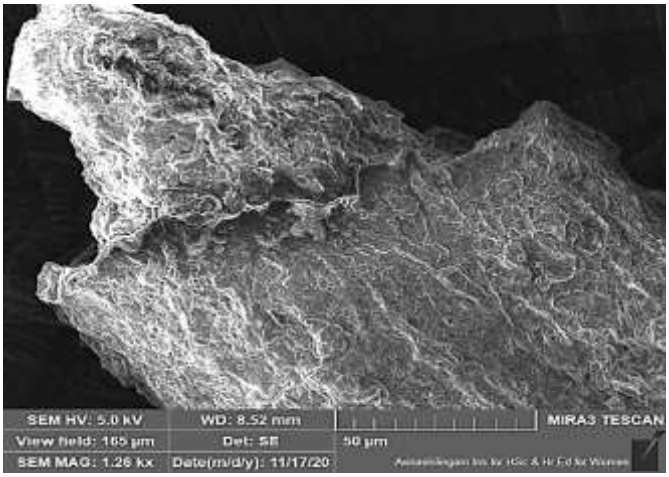

Figure 58g. FESEM image damaged hair surface

Figure 58a-g. FESEM images of prepared depilatory samples treated and untreated hair samples. a) and b) untreated normal hair surface, c) and d) untreated hair edges, e-g) damaged hair surface by prepared depilatory samples

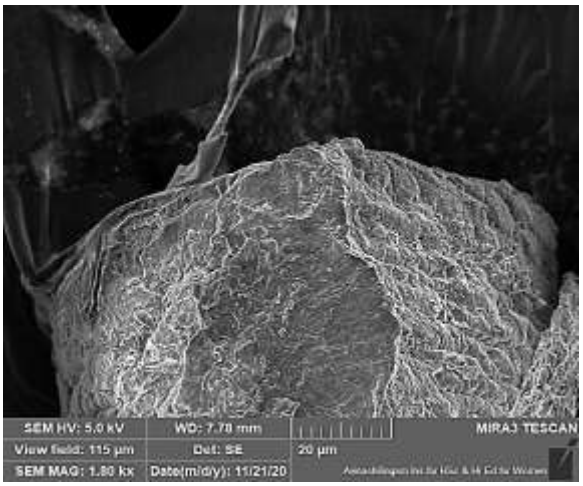

Figure 59a. FESEM image of damaged hair edges

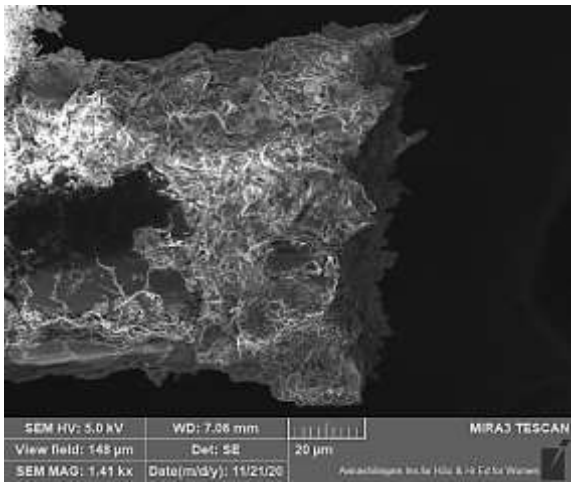

Figure 59b. FESEM image of damaged hair edges

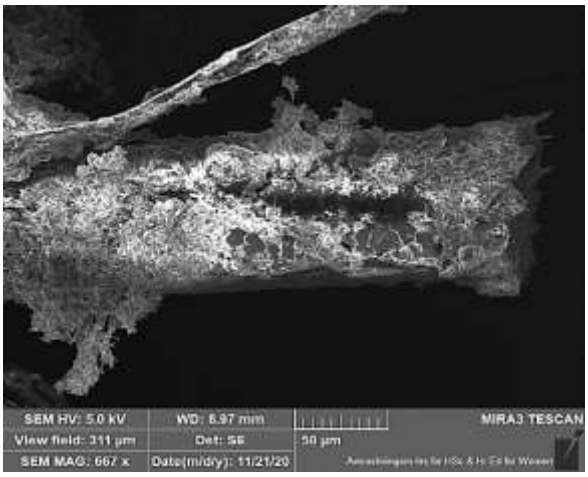

Figure 59c. FESEM image of damaged hair edges

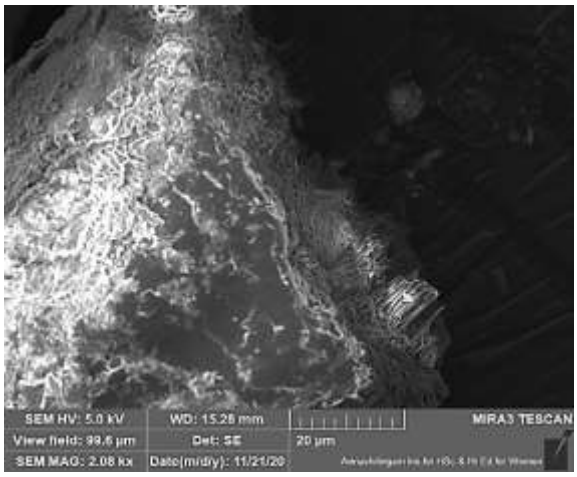

Figure 59d. FESEM image of damaged hair edges

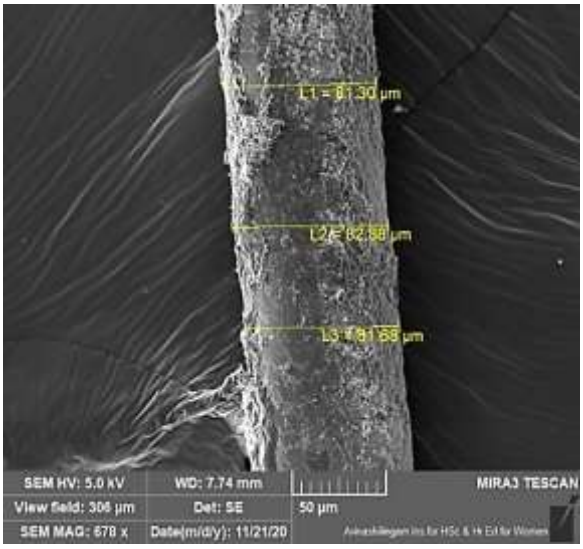

Figure 59e. FESEM image of damaged hair surface

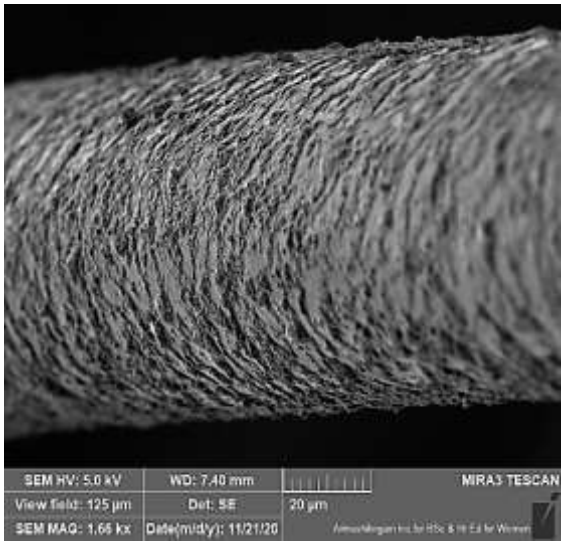

Figure 59f. FESEM image of damaged hair surface

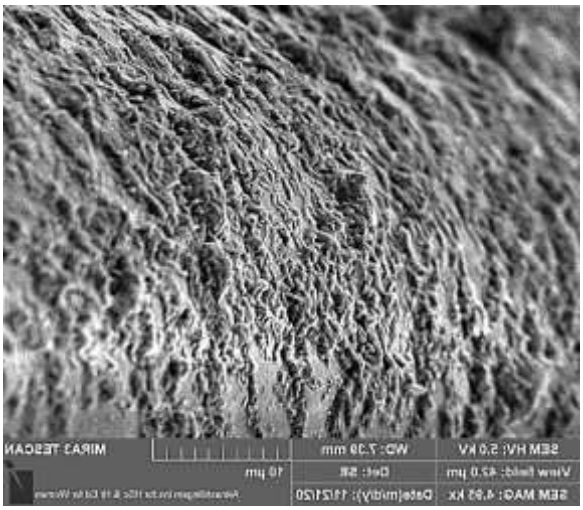

Figure 59g. FESEM image of damaged hair surface

Figure 59h. FESEM image of damaged hair surface

Figure 59a-h. FESEM images of prepared depilatory samples treated hair samples. a-d) damaged hair edges and e-h) damaged hair surface by prepared depilatory samples

4.11 Results of Biological activities of prepared depilatory samples

4.11.1 Results of antioxidant activity of prepared depilatories

Depilatory products are composed of more chemicals that may deliver toxic substances to the skin. This may lead the skin problems which causes by the free radicals. Free radicals are involved in a chain reaction in the skin and are responsible for

skin pigmentation, wrinkling, elastosis, photoaging and drying **(Kusumawati and Indrayanto, 2013)**. The antioxidant potential of prepared depilatory creams was carried out using a DPPH assay (**Figure 60**). DPPH was treated with five different concentrations (0.5, 1.5, 2.5, 3.5 and 5 mg/mL) of prepared samples.

The free radical inhibition decreases by increases in the concentration (0.5-5 mg/mL) of the samples. At minimum concentration (0.5 mg/mL), the samples show good inhibition activity. *Cyperus rotundus* (CAMMCRa-39%; CAMMCRPS-28%) and pumice stone aided depilatory samples (CAMMPSb-31%) showed better inhibition activity than $CAMM_2$ (28%). Gold nanoparticle aided depilatory creams (CAMMCRaNP (46%), CAMMCRaNP (A) (44%) and CAMMPSaNP (43%)) showed the highest inhibition than other samples. In this study, the prepared depilatory creams show significant radical inhibition activity compared with Std (V) (53%) and Std (F) (70%) in a lower concentration.

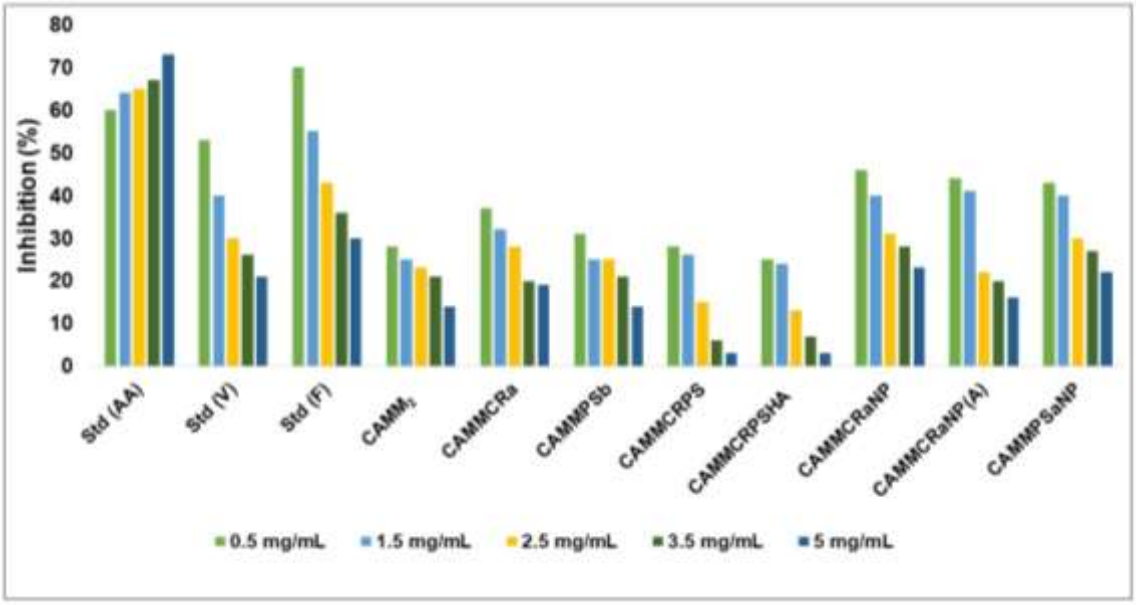

Figure 60. Results of DPPH radical scavenging activity of prepared depilatory samples

4.11.2 Results of antibacterial activity of prepared depilatories

The antibacterial activity of prepared depilatories carried out against *Escherichia coli*, *Salmonella paratyphi*, *Staphylococcus aureus* and *Bacillus subtilis* is given in **Figure 61** and **Figure 62**. The inhibition against selected bacteria increased in a dose-dependent manner (150 µL to 250 µL). All the prepared samples show comparatively higher inhibition against *Escherichia coli* and *Salmonella paratyphi* than the other two bacteria.

CAMMPSaNP and CAMMCRaNP (A) show the highest 17 and 16 mm inhibition against *Escherichia coli*, respectively.

CAMMCRaNP (A) and CAMMCRPS are showed a zone of inhibition of 15 mm against *Salmonella paratyphi*. CAMMPSb and CAMMCRPSHA were showed an inhibition zone of 14 mm against *Salmonella paratyphi*. CAMMCRPSHA and CAMMCRaNP showed 14 mm against *Staphylococcus aureus*. CAMMCRPSHA shows the zone of inhibition (14 mm) against *Bacillus subtilis*. Other samples show the minimum area of inhibition observed between 6 to 13 mm against selected pathogens. This study reveals the prepared samples to exhibit good antibacterial activity against selected pathogens.

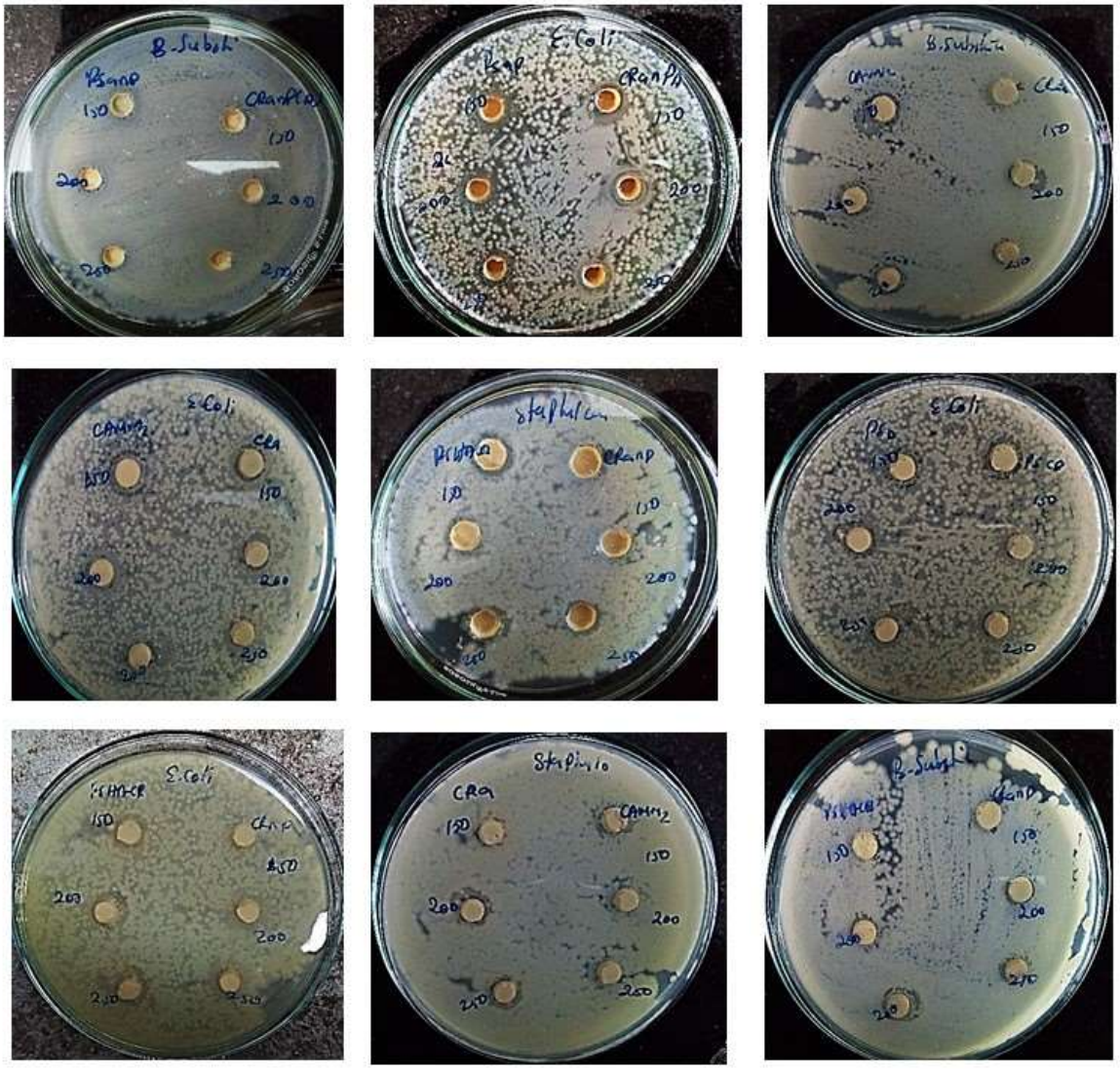

Figure 61. Photograph of antibacterial activity of prepared depilatory samples against gram-positive and negative bacteria

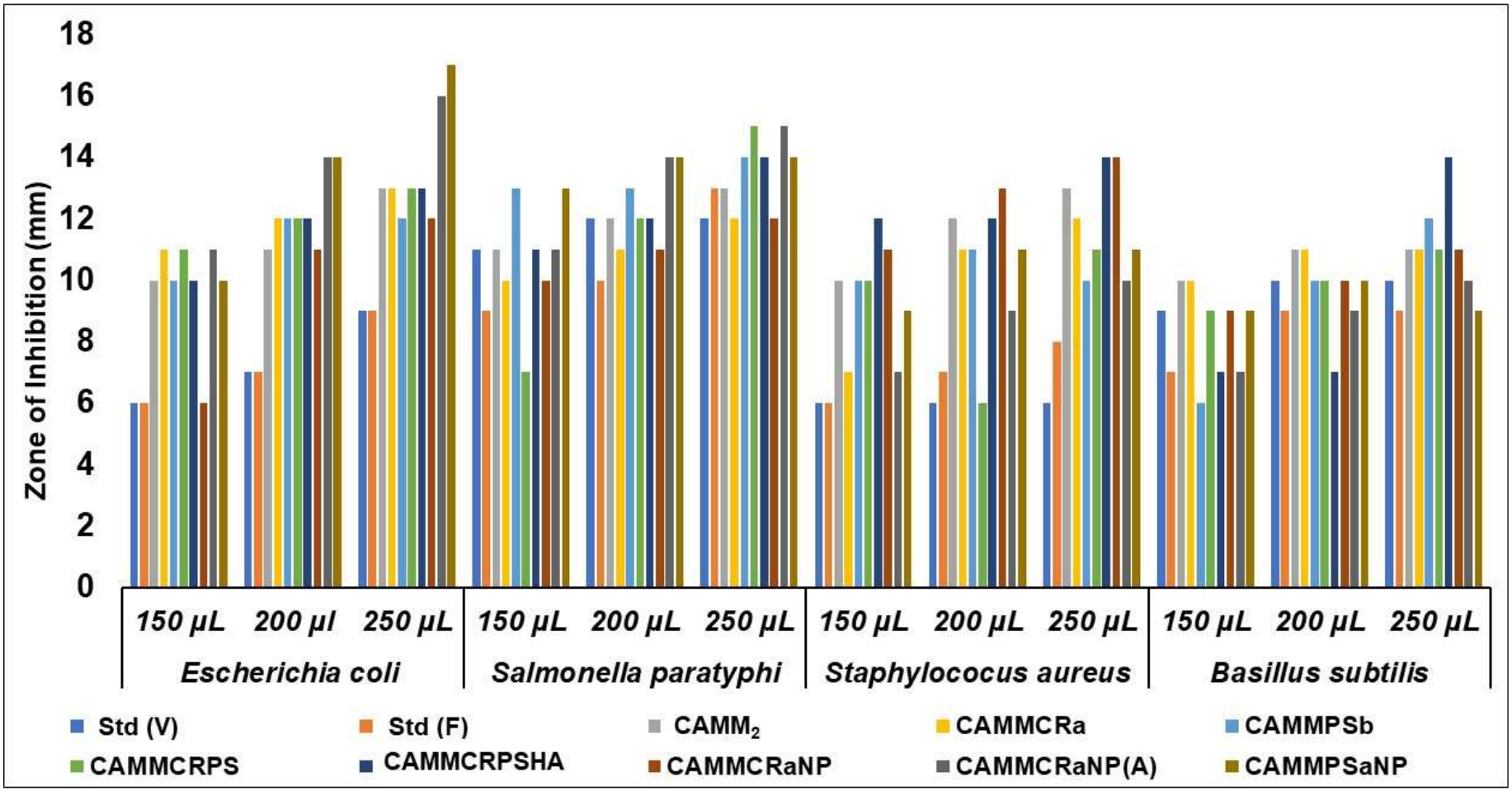

Figure 62. Zone of inhibition of prepared depilatory samples against *Escherichia coli*, *Salmonella paratyphi*, *Staphylococcus aureus* and *Bacillus subtilis*

4.11.3. Results of antifungal activity of prepared depilatories

The antifungal activity of prepared samples is given in **Figure 63 and Figure 64**. All the samples showed minimum inhibition activity against *Aspergillus fumigatus* and *Aspergillus flavus* at a lower concentration. Prepared depilatory samples $CAMM_2$ showed a zone of inhibition of 16 and 20 mm against *Aspergillus fumigatus* and *Aspergillus flavus*, respectively. CAMMCRa exhibit the highest inhibition of 17 mm against *Aspergillus fumigatus* and 16 mm against *Aspergillus flavus*. CAMMPSb and CAMMCRPSHA showed an inhibition zone of 15 mm against *Aspergillus fumigatus* and *Aspergillus flavus*. The highest inhibition of 16 and 18 mm was observed for CAMMCRaNP (A) against *Aspergillus fumigatus* and *Aspergillus flavus*, respectively. CAMMCRaNP showed 16 mm against *Aspergillus flavus*. The maximum inhibition of 17 and 18 mm was observed for CAMMPSaNP against *Aspergillus fumigatus* and *Aspergillus flavus*, respectively. With the increase in the concentration of cream, the inhibition potential against fungal pathogens also significantly increases.

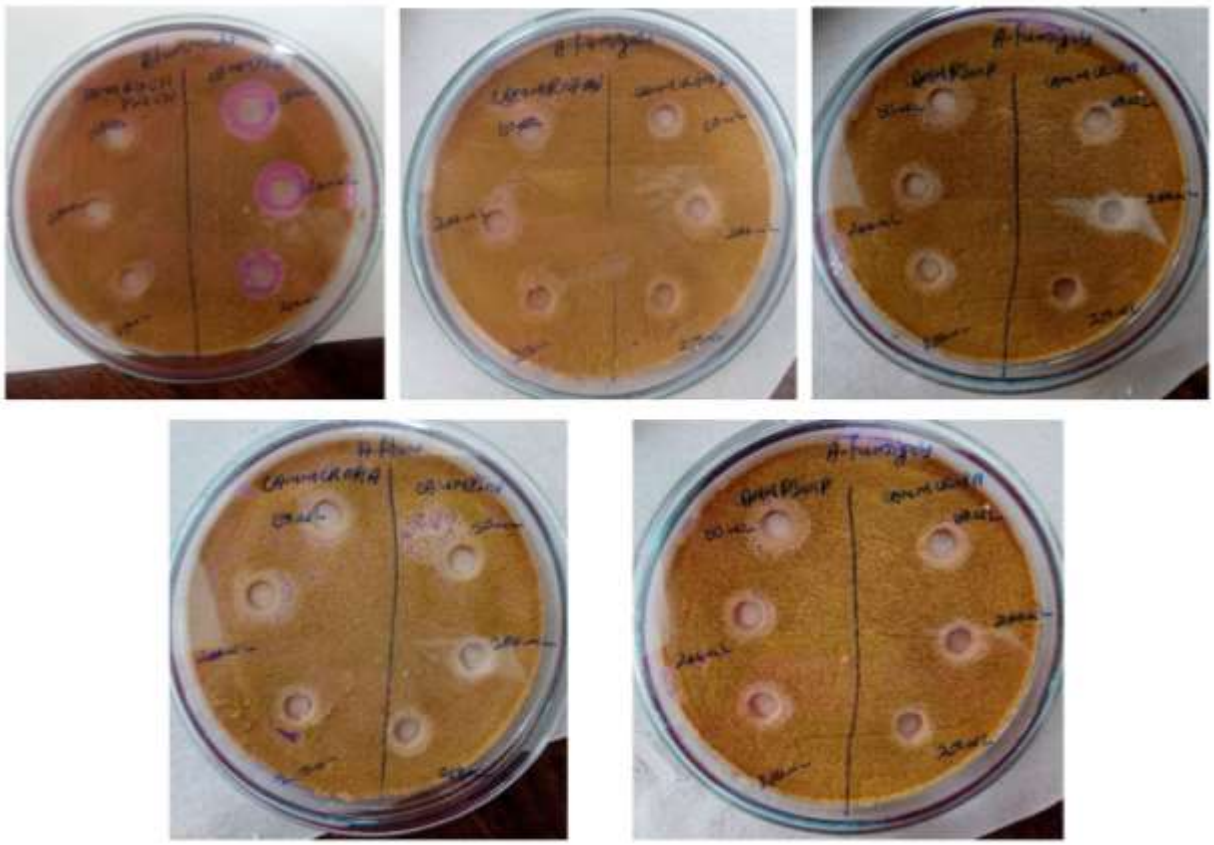

Figure 63. Photographs of ZOI of prepared depilatory samples against *Aspergillus fumigatus* and *Aspergillus flavus*

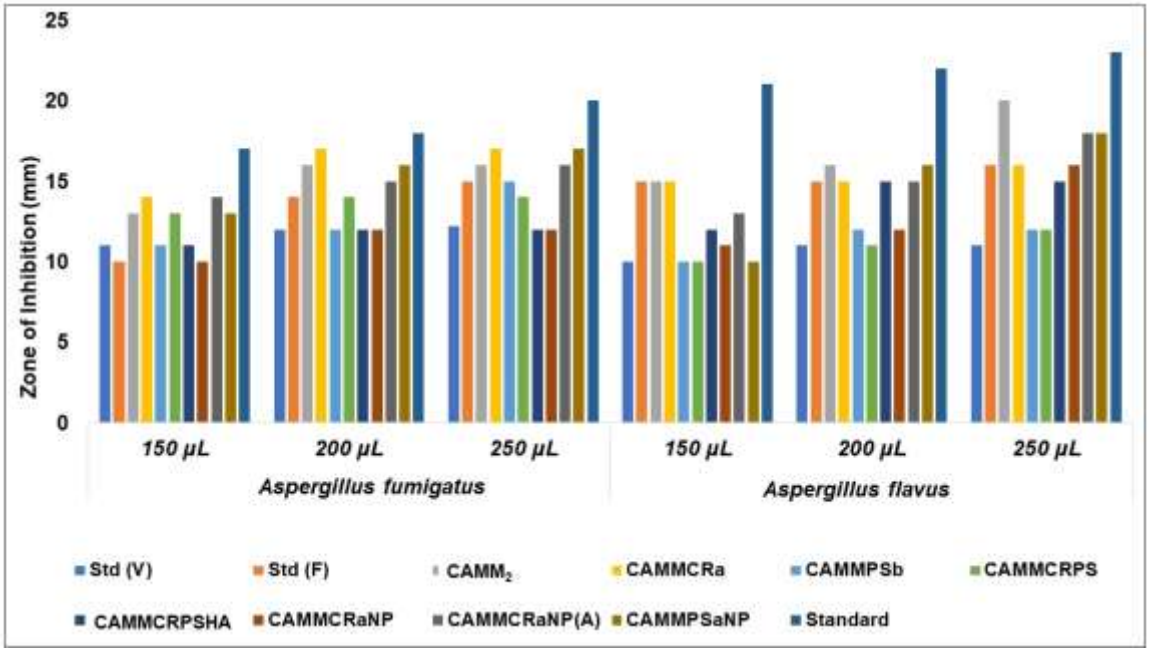

Figure 64. Antifungal activity of prepared depilatory samples against *Aspergillus fumigatus* and *Aspergillus flavus* fungal pathogens

Hair removal by various techniques (shaving, clipping, depilation, sugaring, *etc*) causes microbial infections. Comparatively, depilatory creams reduce the risk of infection than other methods (discussed in Chapters 1 and 2). In this study, the prepared depilatory creams comprise plant samples and gold nanoparticles which are well-known excellent antimicrobial agents, and these formulations release toxic substances in microbes resulting in bacterial cell death.

4.11.4 Results of cell toxicity activity of prepared depilatories

4.11.4.1 Cell viability of prepared depilatories treated HEK-293 and A375 cell lines

The toxicity of prepared depilatory samples on normal cell lines and skin cancer cell lines are given in **Figure 65a-j**. Cell viability studies of prepared samples showed significantly less toxicity on HEK 293 normal cell line and higher toxicity on the skin cancer cell line (**Table 33**). Commercial standards Std (V) and Std (F) showed cell viability from 95 to 62 and 90 to 45%, on skin cancer cell lines respectively. On treatment with HEK 293 cell line, the Std (V) and Std (F) showed 96 to 70% and 95 to 68% cell viability, respectively. More toxicity on both cancer and normal cell lines was seen at the higher sample concentration. With an increase in the concentration of prepared samples, the toxicity on the selected cell lines significantly increases.

Cell viability 96 to 74% and 97 to 28% were observed for CAMMCRa against A375 and HEK-293 cell lines respectively. CAMMPSb showed higher toxicity against A375 (78%) and HEK-293 (35%) at 250 µg/mL. CAMMCRPS and CAMMCRPSHA showed 34 and 30% cell viability against A375 skin cancer cell lines, respectively. Cell viability 67 and 70% showed on HEK-293 using CAMMCRPS and CAMMCRPSHA, respectively. Gold nanoparticles aided depilatory creams shows 95-28% (CAMMCRaNP), 94-27% (CAMMCRaNP (A)) and 94-65% (CAMMPSaNP) cell viability against A375 cell lines. Cell viability percentage 97-65% (CAMMCRaNP), 96-65% (CAMMCRaNP (A)) and cell viability 95-67% (CAMMPSaNP) observed against HEK-293 normal cell lines. With an increased concentration of prepared depilatory samples from 50 to 250 µg/mL, the cell viability decreased, and the toxicity on both normal and cancer cell lines increased.

Table 33. Cell viability of prepared depilatories treated A375 and HEK-293 cell lines

S. No	Prepared depilatories	Cell viability (%)									
		A375					HEK-293				
		Concentration of samples (µg/mL)									
		50	100	150	200	250	50	100	150	200	250
1	**Std (F)**	90	70	67	50	45	95	85	76	70	68
2	**Std (V)**	95	80	72	66	62	96	85	80	76	70
3	**$CAMM_2$**	95	44	37	25	20	94	80	75	70	68
4	**CAMMCRa**	96	83	80	78	74	97	41	38	31	28
5	**CAMMPSb**	93	38	34	26	22	96	79	73	67	65
6	**CAMMCRPS**	95	47	42	38	34	96	80	75	70	67
7	**CAMMCRPSHA**	93	46	40	34	30	96	90	78	74	70
8	**CAMMCRaNP**	95	37	35	33	28	97	78	75	70	65
9	**CAMMCRaNP (A)**	94	78	45	32	27	96	78	70	69	65
10	**CAMMPSaNP**	94	80	76	72	65	95	89	80	72	67
11	**DOX**	96	86	45	34	28	92	54	32	25	21

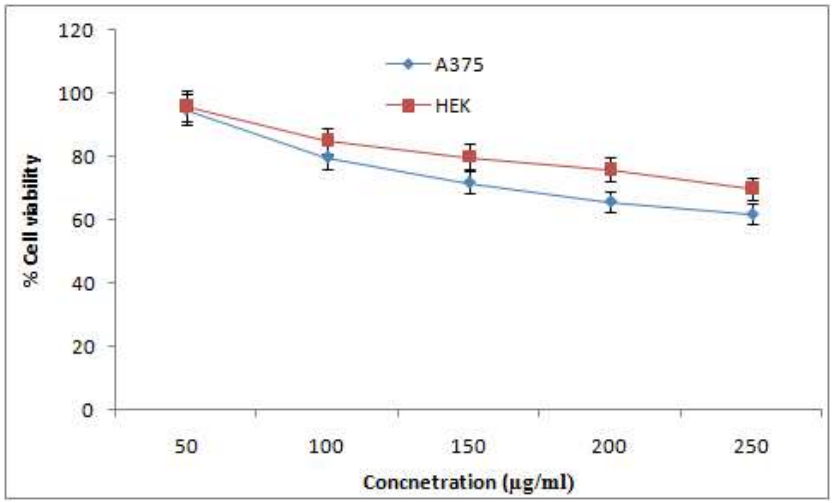

Figure 65a. Cell viability of Std (F)

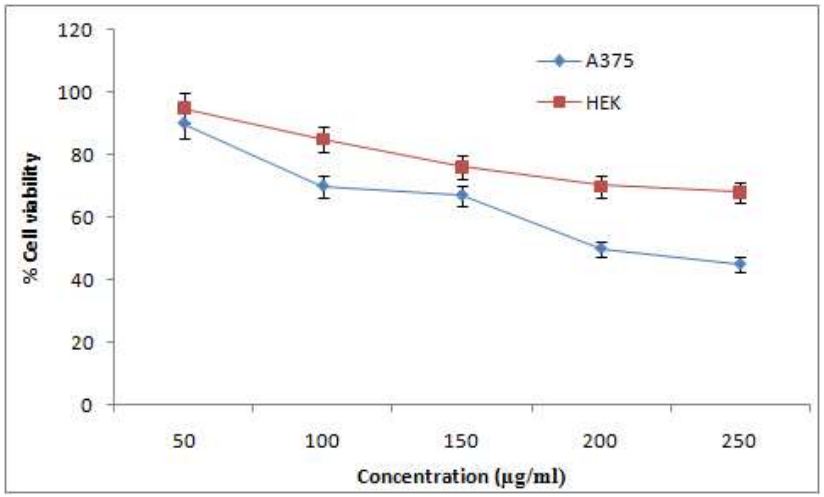

Figure 65b. Cell viability of Std (V)

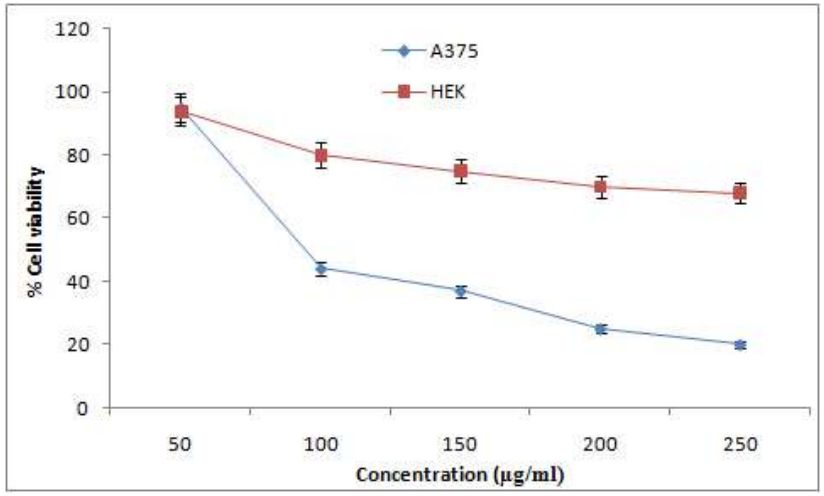

Figure 65c. Cell viability of $CAMM_2$

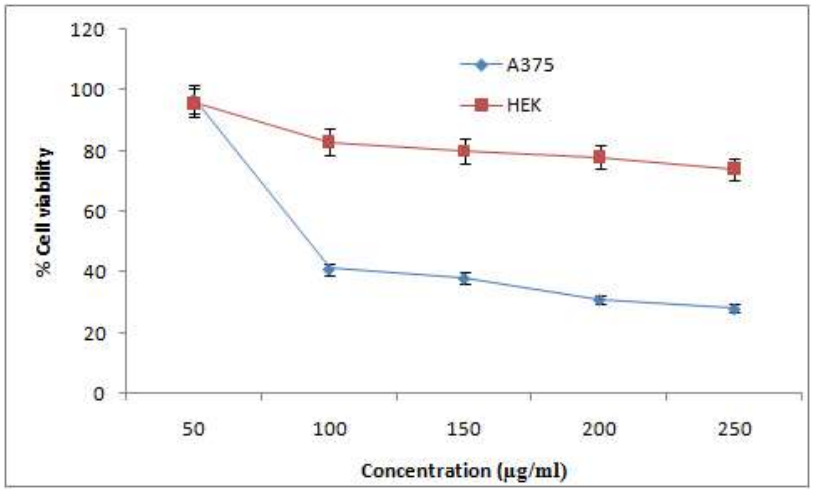

Figure 65d. Cell viability of CAMMCRa

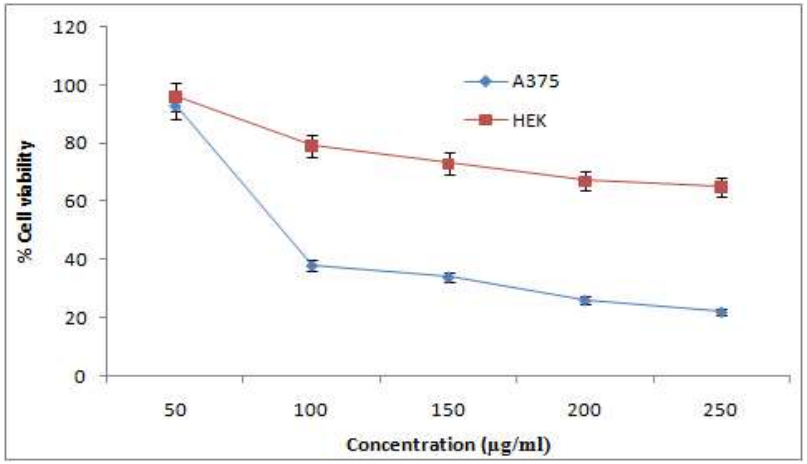

Figure 65e. Cell viability of CAMMPSb

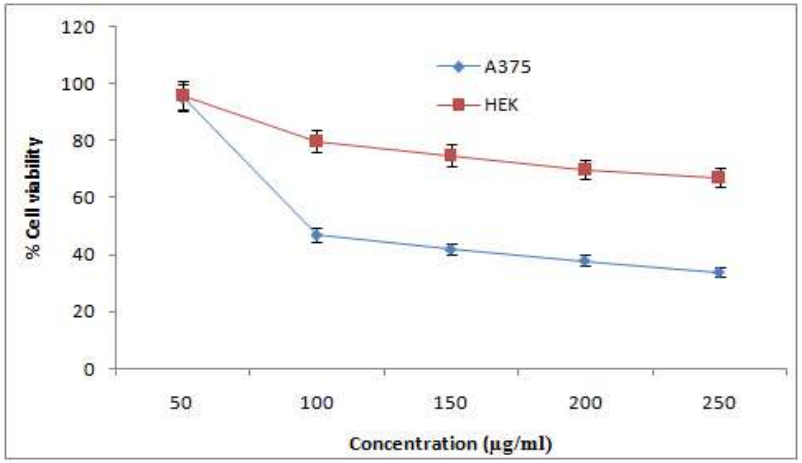

Figure 65f. Cell viability of CAMMCRPS

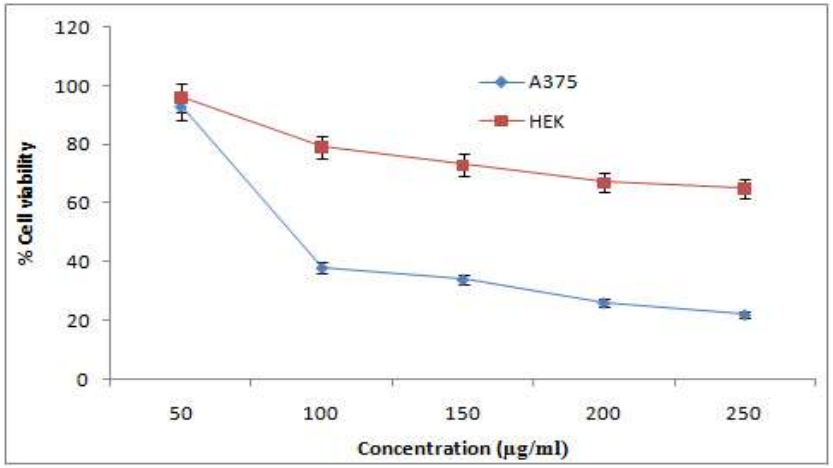

Figure 65g. Cell viability of CAMMCRPSHA

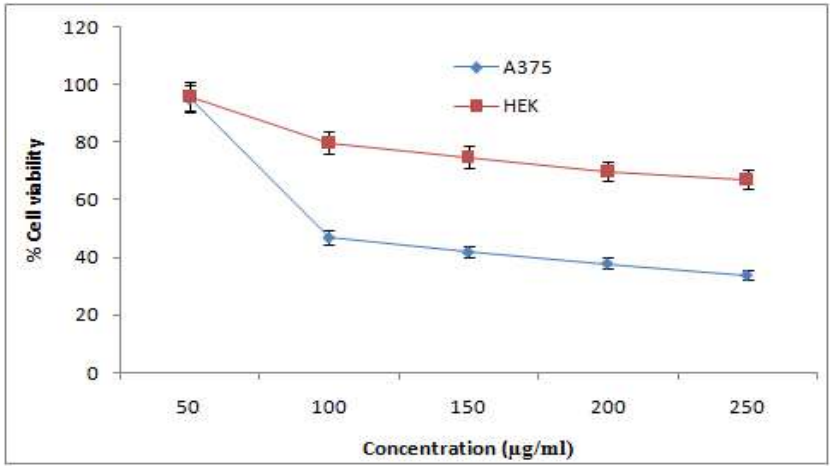

Figure 65h. Cell viability of CAMMCRaNP

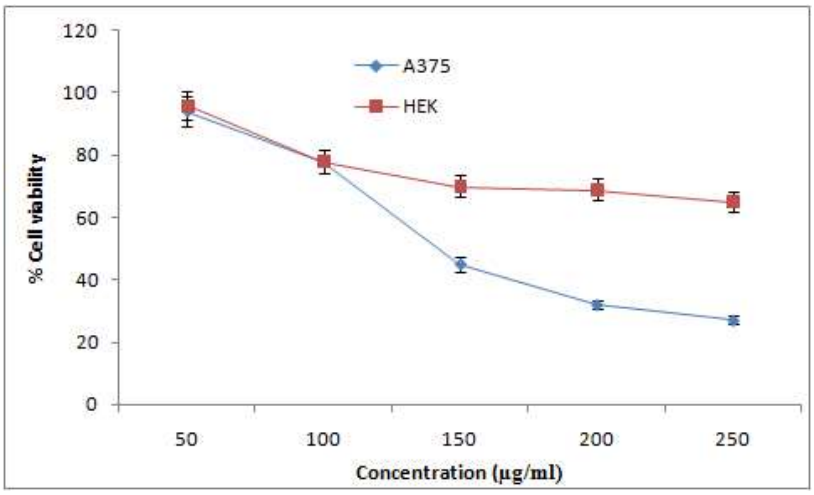

Figure 65i. Cell viability of CAMMCRaNP (A)

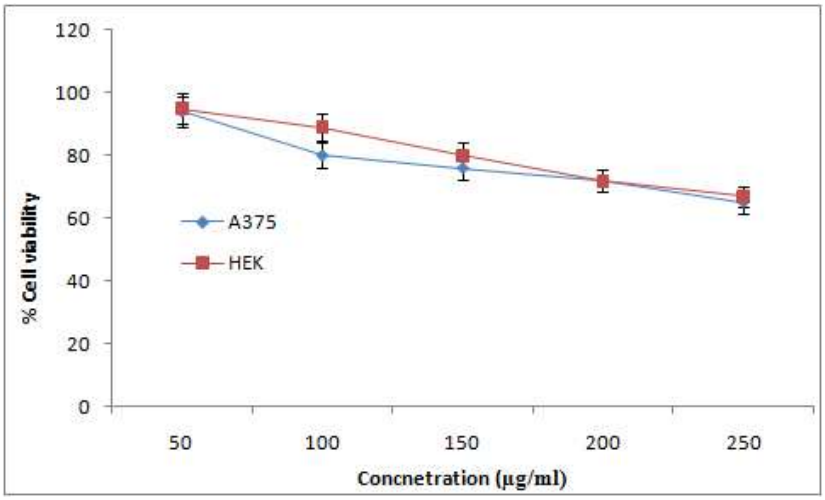

Figure 65j. Cell viability of CAMMPSaNP

Figure 65a-j. Cell viability of a) Std (F), b) Std (V), c) $CAMM_2$, d) CAMMCRa, e) CAMMPSb, f) CAMMCRPS, g) CAMMCRPSHA, h) CAMMCRaNP, i) CAMMCRaNP (A) and j) CAMMPSaNP against A375 and HEK-293 cell lines

The IC_{50} value of prepared depilatory samples is given in **Figure 66**. The IC_{50} value of CAMMCRa, CAMMPSb, CAMMCRPS and CAMMCRPSHA were obtained at 70, 64, 120 and 73 µg/mL respectively. The IC_{50} values 58, 68 and 105 µg/mL obtained for CAMMCRaNP, CAMMCRaNP (A) and CAMMPSaNP respectively. $CAMM_2$ show IC_{50} in 67 µg/mL and Std (F) show at 172 µg/mL. CAMMPSb, CAMMCRaNP, CAMMCRaNP (A) and $CAMM_2$ show 50% cell inhibition on skin cancer cell lines at lower concentrations than other samples in all groups.

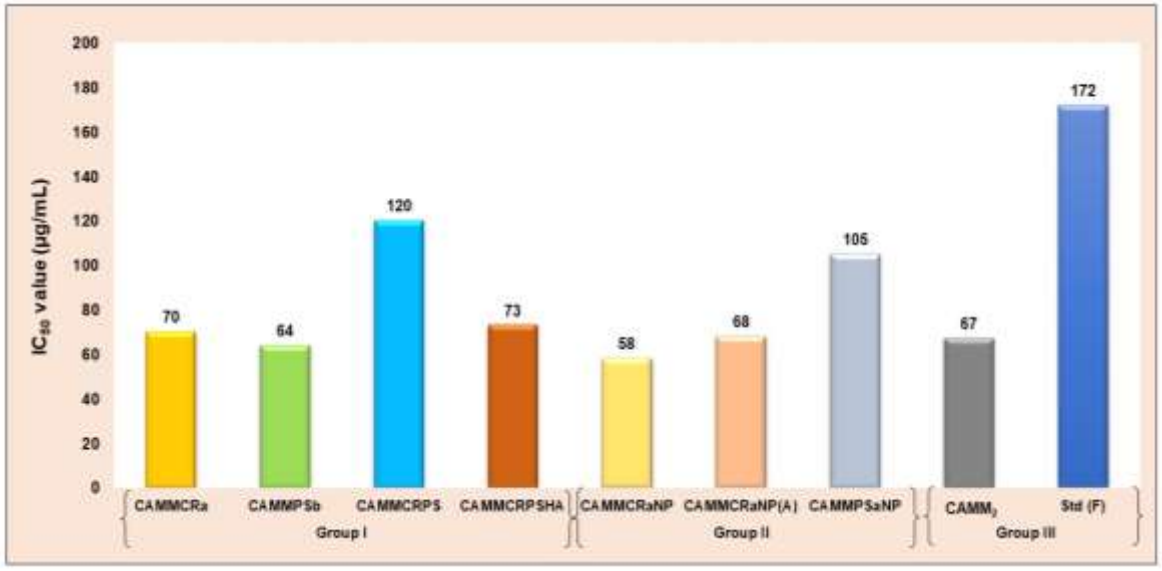

Figure 66. Graphical representation of IC_{50} value of synthesized depilatories against A375 cell lines

4.11.4.2 Apoptotic cell inhibition of prepared depilatory samples

The nuclear level interaction between prepared depilatory creams and A375 cancer cell lines are shown in **Figure 67a-c and 68a-c**. The AO and PI staining of prepared samples was carried out for depilatories treated skin cancer cell lines. Cell death and nuclear fragmentation were observed for depilatories treated skin cancer cell lines. This study reveals the prepared samples' efficacy in reducing cancer cell lines' growth and showing minimum toxicity on normal cell lines at lower concentrations.

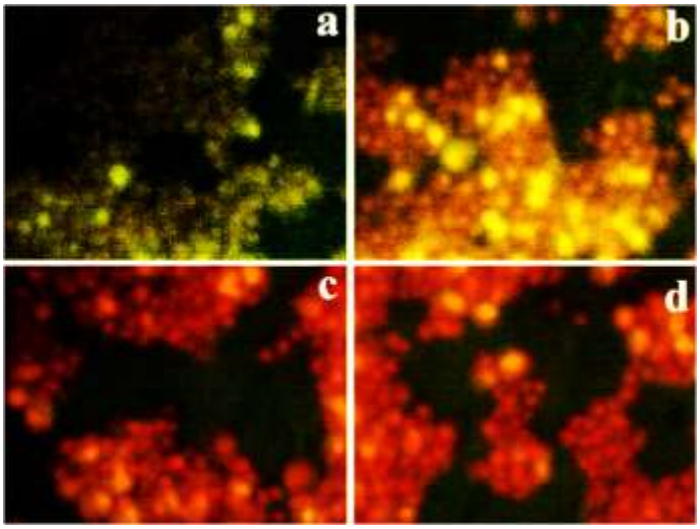

Figure 67a. AO/EtBr staining of CAMMPSb

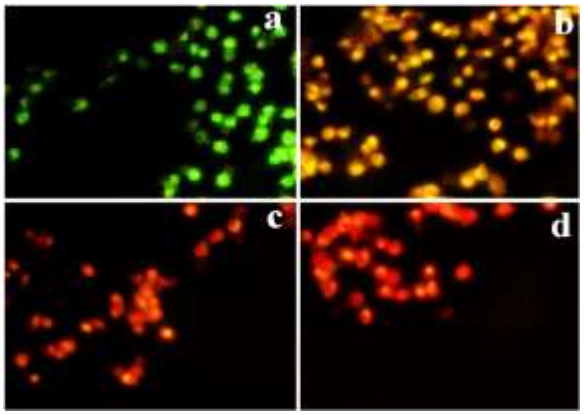

Figure 67b. AO/EtBr staining of CAMMCRaNP

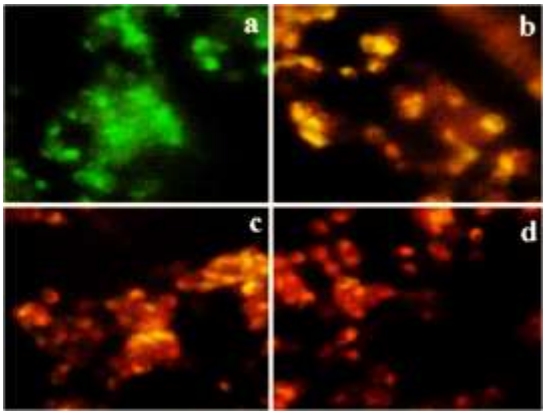

Figure 67c. AO/EtBr staining of CAMMCRaNP (A)

Figure 67a-c. Apoptosis analysis of prepared depilatory samples a) CAMMPSb, b) CAMMCRaNP and c) CAMMCRaNP (A) against A375 cell line using AO/EtBr staining

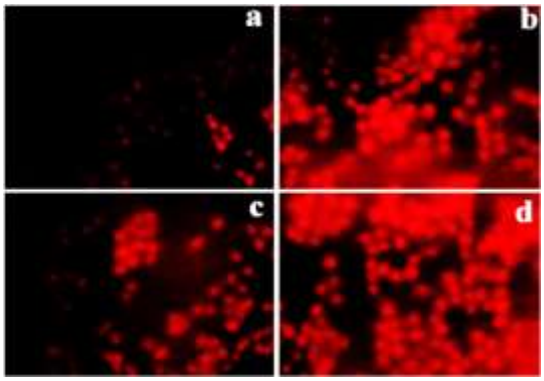

Figure 68a. PI staining of CAMMPSb

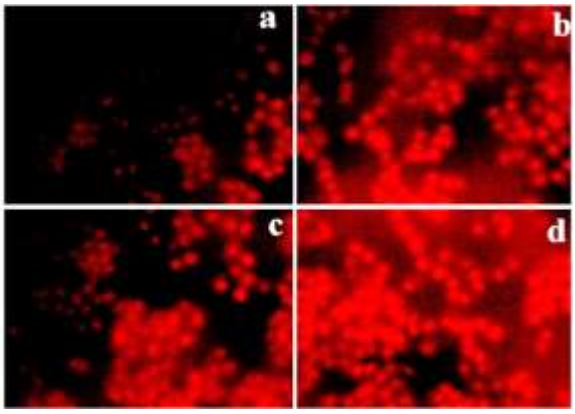

Figure 68b. PI staining of CAMMCRaNP

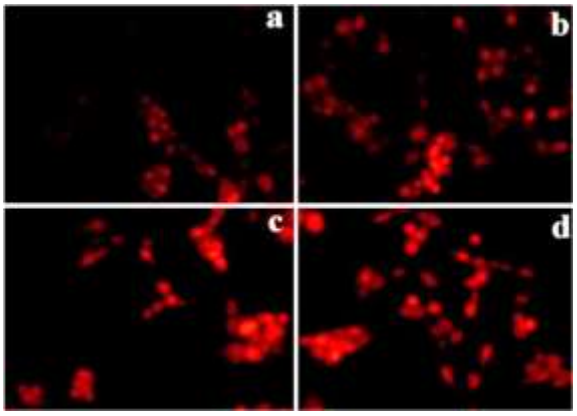

Figure 68c. PI staining of CAMMCRaNP (A)

Figure 68a-c. Apoptosis analysis of prepared depilatory samples a) CAMMPSb, b) CAMMCRaNP and c) CAMMCRaNP (A) against A375 cell line using PI staining

PHASE III

Formulation of Biodegradable Skin Substitutes and their Biological Activities

4.12 Physical and visual observation of skin substitutes

4.12.1 Results of colour, thickness and texture of prepared skin substitutes

Skin substitutes were prepared using biodegradable materials, and the details of the samples are given in **Table 34**. $SLFgNP_0$ is composed of biodegradable materials such as chitosan, gelatin, sodium alginate and fenugreek mucilage and is known as blank. Gold nanoparticles were synthesized using the tuber portion of *Cyperus rotundus* and leaves of *Hemigraphis alternata*. Metal nanoparticles are strongly enhancing wound healing activity, tissue regeneration, antibacterial activity and drug delivery **(Peng *et al*., 2008; Das and Baker, 2016; Berthet *et al*., 2017; Wang *et al*., 2017)**. Gold nanoparticles have capable of passing the *stratum corneum* and spreading broadly within the dermis and epidermis **(Huang *et al*., 2010)**. Due to the advantages of gold nanoparticles for their unique properties, biocompatibility and biological activities the synthesized CRaNP and HAaNP were successfully incorporated into the $SLFgNP_0$ by the magnetic stirring method. CRaNP-aided skin substitutes are represented as $SLFgCRaNP_1$, $SLFgCRaNP_2$ and $SLFgCRaNP_3$. HAaNP-aided skin substitutes are represented as $SLFgHAaNP_1$, $SLFgHAaNP_2$ and $SLFgHAaNP_3$.

Table 34. The results of the preparation of skin substitutes and their physical observations

S. No	Sample code	Composition	Observations		
			Thickness (µm)	Colour	Flexible/ Elongate /Smooth
1	$SLFgNP_0$	Blank	64	Yellow	Flexible, Smooth and Less Elongate
2	$SLFgCRaNP_1$	$SLFgNP_0$+CRaNP (5 mg/mL)	106	Yellowish purple	
3	$SLFgCRaNP_2$	$SLFgNP_0$+CRaNP (10 mg/mL)	87		
4	$SLFgCRaNP_3$	$SLFgNP_0$+CRaNP (15 mg/mL)	114		
5	$SLFgHAaNP_1$	$SLFgNP_0$+HAaNP (5 mg/mL)	87	Yellowish brown	
6	$SLFgHAaNP_2$	$SLFgNP_0$+HAaNP (10 mg/mL)	81		
7	$SLFgHAaNP_3$	$SLFgNP_0$+HAaNP (15 mg/mL)	87		

The average thickness of the prepared skin substitutes is < 1.5 mm, and all the samples possess good flexibility, smooth texture, and less elongation. The samples were not changing their appearance, colour, texture for up to 2 years. There is no microbial contamination noted visually in skin substitutes at room temperature up to 2 years. The photograph of prepared skin substitutes is given in **Figures 69a and b**.

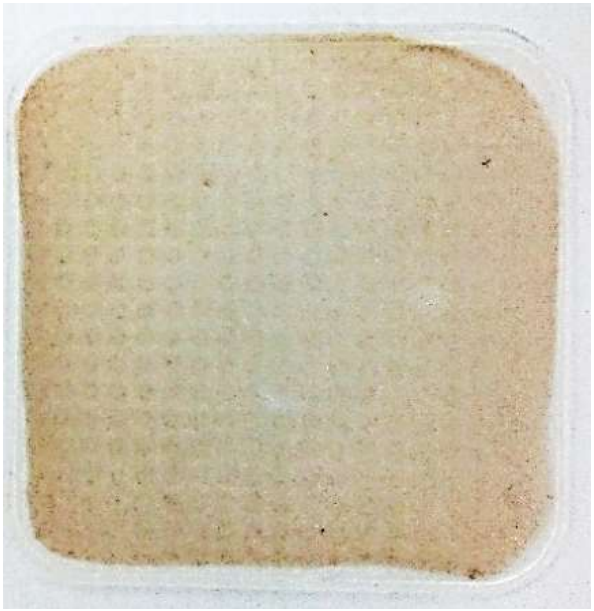

Figure 69a. Photograph of prepared skin substitute on a heat-resistant silicon rubber mat

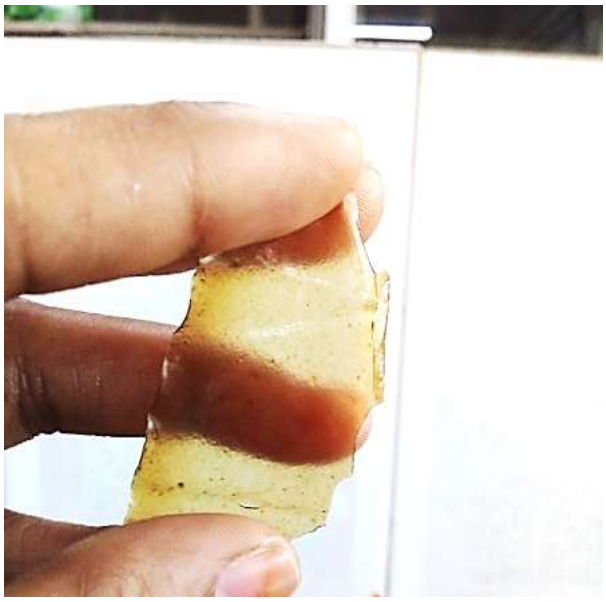

Figure 69b. Photograph of flexible and transparent prepared skin substitute

4.12.2 Results of tensile and elongation properties of the skin substitutes

The tensile strength (**Figure 70a**) and elongation properties (**Figure 70b**) of the gold nanoparticle-aided skin substitutes decrease with an increase in gold nanoparticle concentration. The tensile strength of $SLFgNP_0$ is 2.67N. The CRaNP-aided skin substitutes decrease the tensile strength from 2.52 to 1.91N. The HAaNP-aided skin substitutes decrease the tensile strength from 1.63 to 0.613N. Similarly, with increases in gold nanoparticles concentration, the elongation capacity of the CRaNP-aided skin substitutes decreases from 45.3 to 30.1%. HAaNP-aided skin substitutes show percentage of elongation 27.9, 29.1 and 10.8% for $SLFgHAaNP_1$, $SLFgHAaNP_2$ and $SLFgHAaNP_3$ respectively. All the prepared skin substitutes show less elongation than $SLFgNP_0$ (45.8%). These results indicate that plant-aided gold nanoparticle-incorporated skin substitutes show excellent binding ability with coordinated materials in a dose-dependent manner.

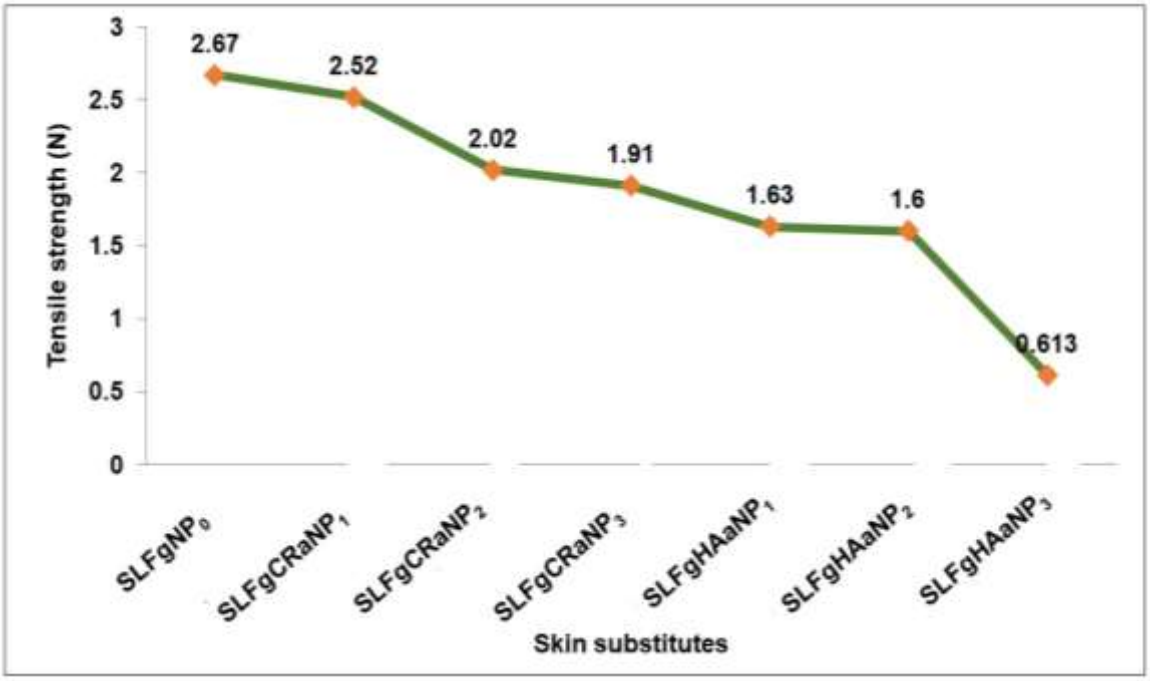

Figure 70a. The graphical representation of tensile strength of prepared skin substitutes

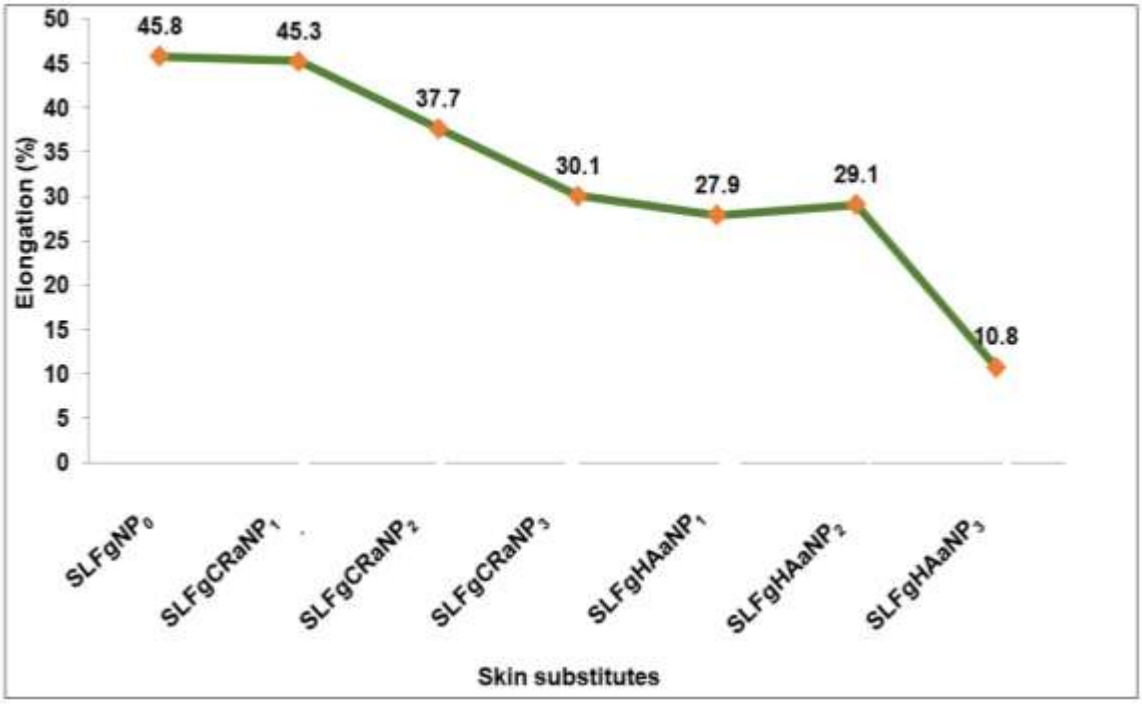

Figure 70b. The graphical representation of percentage elongation of prepared skin substitutes

4.12.3 Results of moisture content of skin substitutes

The moisture content was 75% observed for $SLFgNP_0$. The percentage of moisture content 74, 75 and 67% were observed for $SLFgCRaNP_1$, $SLFgCRaNP_2$, $SLFgCRaNP_3$ respectively. The moisture content of CRaNP-aided skin substitutes are high than HAaNP-aided skin substitutes ($SLFgHAaNP_1$ -71%, $SLFgHAaNP_2$ -65% and $SLFgHaNP_3$ -68%). At a lower concentration of gold nanoparticles, the moisture content is high (**Table 35**). This weight loss may have been due to the presence of biomaterials (chitosan, sodium alginate, gelatin, fenugreek mucilage, and plant embeds) in prepared skin substitutes. The moisture content of the skin substitutes (increasing gold nanoparticles concentration) is less than $SLFgNP_0$.

Table 35. Results of moisture content of prepared skin substitutes

S. No	Sample code	Weight (g) of the skin substitutes (1x1 cm)			Moisture content (%)
		Initial	After 24h drying	Desiccated samples	
1	$SLFgNP_0$	0.03573	0.00883	0.00721	75
2	$SLFgCRaNP_1$	0.05618	0.01437	0.01155	74
3	$SLFgCRaNP_2$	0.05235	0.01305	0.01074	75
4	$SLFgCRaNP_3$	0.05242	0.01723	0.01072	67
5	$SLFgHAaNP_1$	0.03690	0.01086	0.00886	71
6	$SLFgHAaNP_2$	0.03994	0.01229	0.00979	65
7	$SLFgHAaNP_3$	0.04459	0.01415	0.01110	68

4.12.4 Results of water uptake and water ageing ability of gold nanoparticles aided skin substitutes

The percentage of water uptake and water ageing ability of prepared skin substitutes are given in **Figure 71a and Figure 71b**. The weight difference between tested skin substitutes is given in **Table 36**. Water uptake and water ageing are essential for body fluid absorption, cell nutrients and metabolites transfer **(Parvez *et al*., 2012)**. The absorbance of water is high between 0 to 10 min time intervals. CRaNP and HAaNP incorporated skin substitutes show decreased water uptake and water ageing by the saturation time increase from 10-60 min. Comparatively, CRaNP aided skin substitutes showed less water uptake and water ageing due to the binding ability of CRaNP with other constituents. HAaNP aided skin substitutes showed higher water uptake and water ageing. The higher water uptake and water ageing ability of HAaNP aided skin may be due to the film's porosity, which may be used to hold a large number of water molecules and it can be attributed to their higher hydrophilic nature. The hydrophilicity of the prepared skin substitutes decreased with an increase in CRaNP concentration.

Table 36. Water uptake and Water ageing ability of prepared skin substitutes at different time intervals

S. No	Sample code	0 min	10 min		20 min		30 min		40 min		50 min		60 min	
		Initial	WU	WA	WU	WA	WU	WA	WU	WA	WU	WA	WU	WA
1	$SLFgNP_0$	0.0167	0.02183	0.0154	0.02130	0.0143	0.0202	0.0134	0.0198	0.0139	0.02017	0.0137	0.0192	0.0125
2	$SLFgCRaNP_1$	0.0284	0.0352	0.0289	0.0346	0.0281	0.0332	0.0265	0.0323	0.0253	0.0313	0.0248	0.0311	0.0241
3	$SLFgCRaNP_2$	0.0247	0.0304	0.0251	0.0303	0.0248	0.0295	0.0224	0.0293	0.0225	0.0288	0.0212	0.0276	0.0200
4	$SLFgCRaNP_3$	0.0246	0.0278	0.0213	0.0273	0.0215	0.0268	0.0201	0.0260	0.0202	0.0262	0.0195	0.0260	0.0203
5	$SLFgHAaNP_1$	0.0193	0.0255	0.0157	0.0237	0.0149	0.0235	0.0155	0.0227	0.0151	0.0224	0.0155	0.0221	0.0145
6	$SLFgHAaNP_2$	0.0183	0.0257	0.0162	0.0237	0.0154	0.0234	0.0158	0.0226	0.0139	0.0220	0.0132	0.0213	0.0136
7	$SLFgHAaNP_3$	0.0206	0.0296	0.0201	0.0276	0.0191	0.0272	0.0181	0.0260	0.0166	0.0256	0.0170	0.0253	0.0179

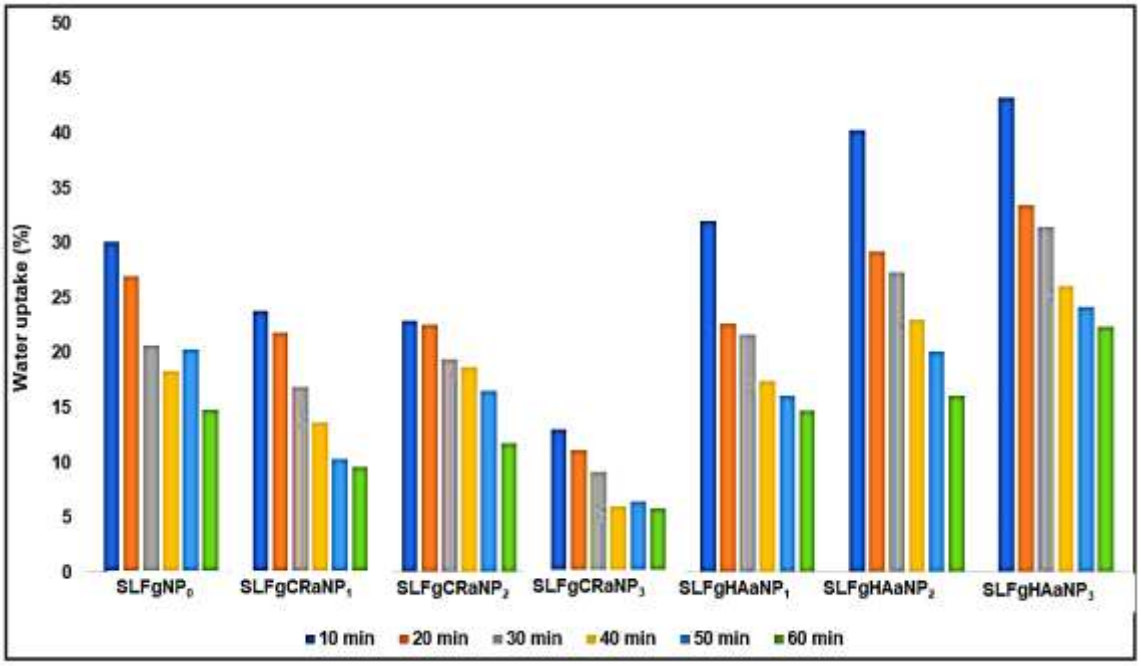

Figure 71a. The graphical representation of the percentage of the water uptake ability of prepared skin substitutes

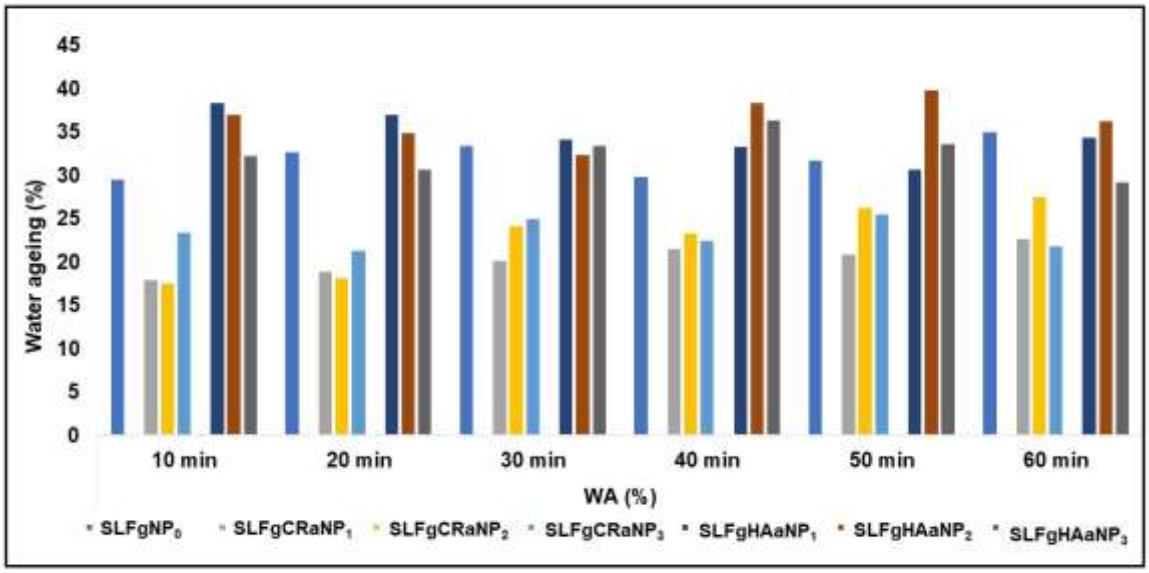

Figure 71b. The graphical representation of the percentage of the water ageing ability of prepared skin substitutes

4.13 Characterization results of prepared skin substitutes

4.13.1 FTIR spectrum of prepared skin substitutes

FTIR spectrum of synthesized skin substitutes is shown in **Figure 72 and Figure 73**. The peaks at 3325.28 and 3294.42 cm^{-1} attributed to O-H and N-H groups of polymeric materials. The peaks at 2947.23 and 2939.52 cm^{-1} are due to aliphatic C-H symmetry and 2885.51 cm^{-1} due to asymmetric vibration of aliphatic C-H in polysaccharides. The peak at 2360.81 cm^{-1} is due to the CO_2 group. Combined groups of amides and -C=O were observed at 1651.07 cm^{-1} this may be due to the N-acetyl amide group in polymers.

The peaks at 1558.48 cm^{-1} and 1550.77 cm^{-1} are due to the -N-H bending vibration in the amide II group. The peak at 1419.61 cm^{-1} is responsible for C-H bending vibrations and 1334.74 cm^{-1} due to the stretching vibration of C-F of the alkyl group. The peak at 1327.03 cm^{-1} is due to C-N stretching in the aromatic group. The peak at 1219.01 and 1226.73 cm^{-1} is responsible for -COOH group. C-O stretching in ether groups was observed at 1033.85 and 848.68 cm^{-1}. A carboxylic group of O-H was observed at 925.83 and 918.12 cm^{-1}. The peaks at 671.23 and 671.26 cm^{-1} due to the C-H bond. The FTIR results confirmed the presence of essential components of the prepared skin substitutes.

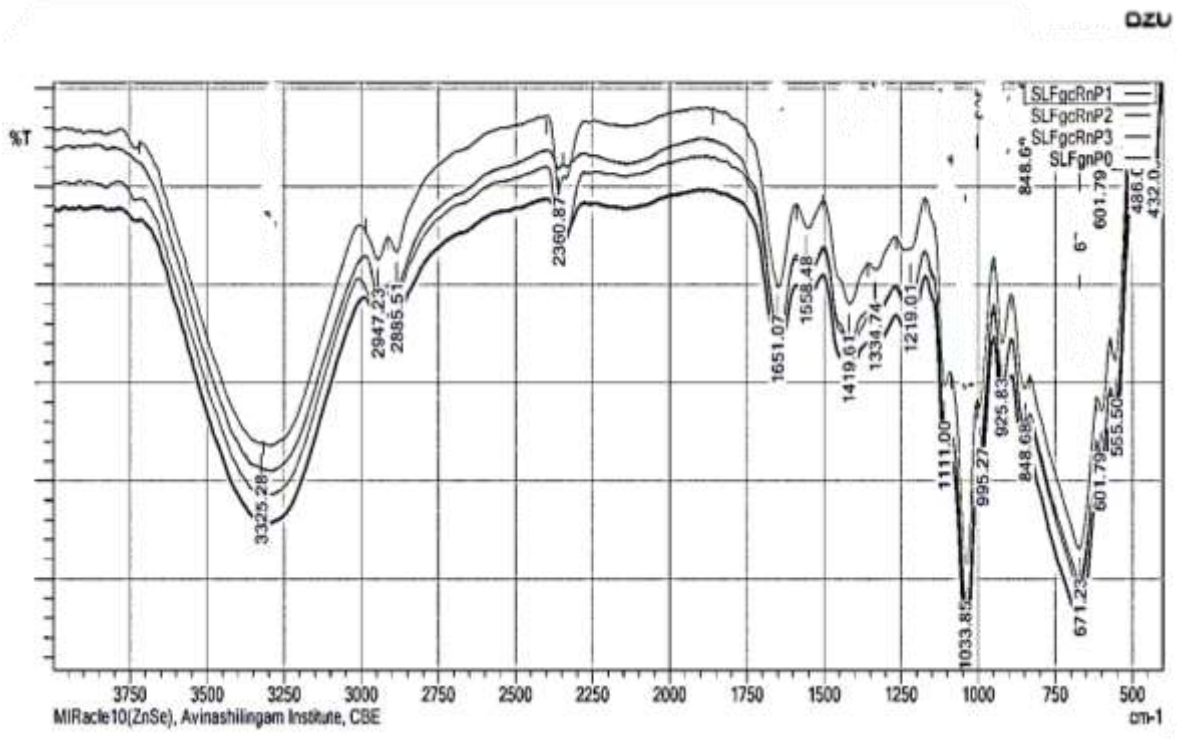

Figure 72. FTIR spectrum of $SLFgNP_0$ and CRaNP-aided skin substitutes

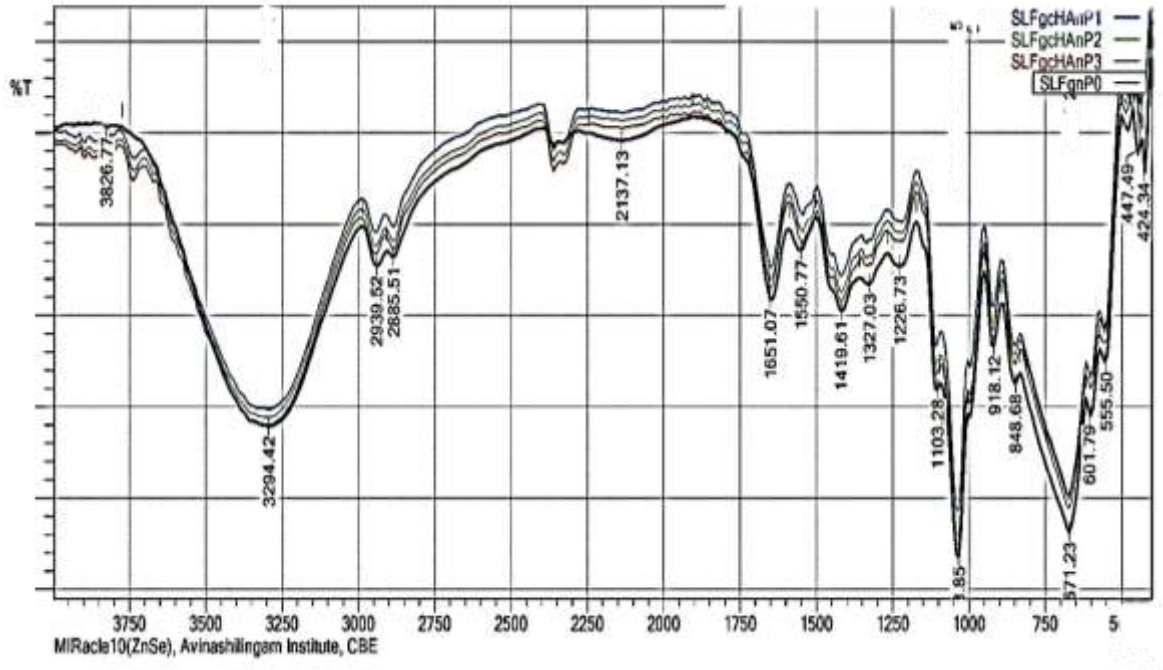

Figure 73. FTIR spectrum of SLFgNP$_0$ and HAaNP-aided skin substitutes

4.13.2 Thermogravimetric analysis of prepared skin substitutes

The DTG spectrum of prepared skin substitutes is given in **Figures 74 and 75**. The thermal decomposition of the samples is in three phases. The first phase of decomposition starts from room temperature to 100ºC. The maximum decomposition was observed at 68ºC for SLFgNP$_0$ and 63ºC for CRaNP-aided skin substitutes. At this phase, HAaNP-aided skin substitutes are (SLFgHAaNP$_1$ and SLFgHAaNP$_2$) reaches maximum decomposition at 61ºC, and 72ºC observed for SLFgHAaNP$_3$. This first phase may be due to the moisture present in polymer composite and readily volatile plant impurities. The second phase of decomposition observed between 150 to 250ºC, may be due to the break in the samples' molecular structure. The complete decomposition is seen in the third phase (250-350ºC). The maximum temperature (309-311ºC) observed for the decomposition of nanoparticles-aided skin substitutes than blank (307ºC). The thermal stability of skin substitutes is slightly increased by incorporating the gold nanoparticles.

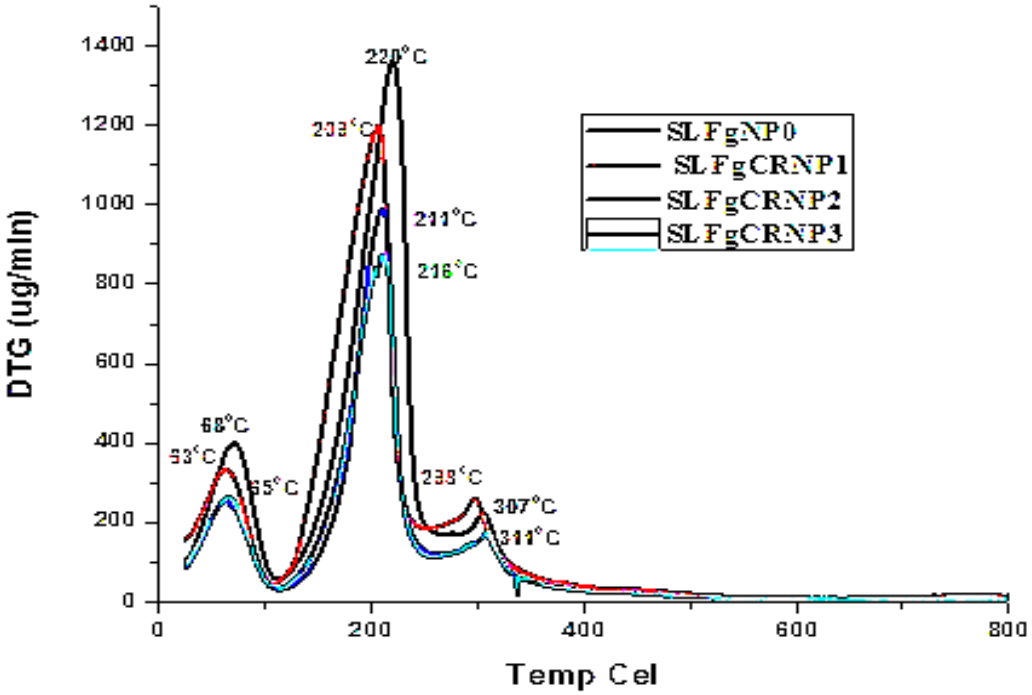

Figure 74. DTG spectrum of SLFgNP$_0$ and CRaNP-aided skin substitutes

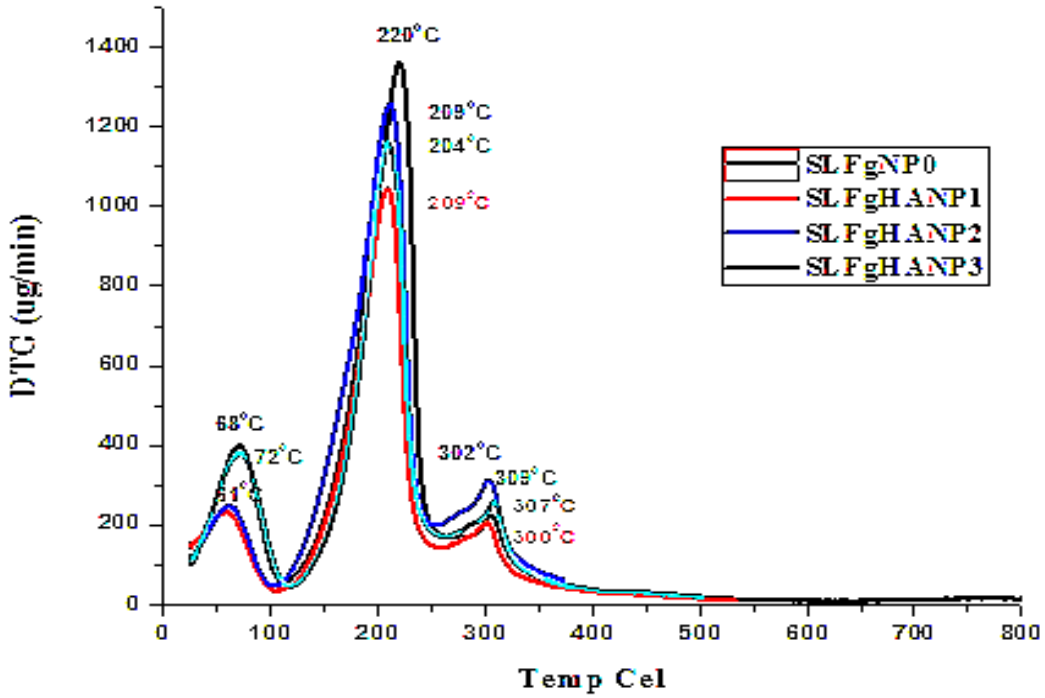

Figure 75. DTG spectrum of SLFgNP$_0$ and HAaNP-aided skin substitutes

4.13.3 Results of 3D Optical profilometry analysis of skin substitutes

The surface texture of the prepared skin substitute was noticed using a 3D Optical profilometer. The prepared skin substitutes are seen as smooth and even texture. The surface morphology is given in **Figure 76a-g**. The CRaNP-aided skin substitutes show average roughness value Ra is 0.8, 1.77 and 2.35 µm for $SLFgCRaNP_1$, $SLFgCRaNP_2$ and $SLFgCRaNP_3$, respectively. The Ra values 2.33, 1.37 and 0.61 µm were observed for $SLFgHAaNP_1$, $SLFgHAaNP_2$ and $SLFgHAaNP_3$ respectively. The $SLFgNP_0$ shows an average roughness value of 0.7530 µm. With the increase in the amount of CRaNP, the roughness of the samples also increased. With the increase in the amount of HAaNP, the roughness of the samples decreased. Higher roughness leads the higher hydrophobicity **(Shanthi *et al*., 2020)**. Thus CRaNP-aided skin substitutes decrease the nature of hydrophilicity than HAaNP-aided skin substitutes.

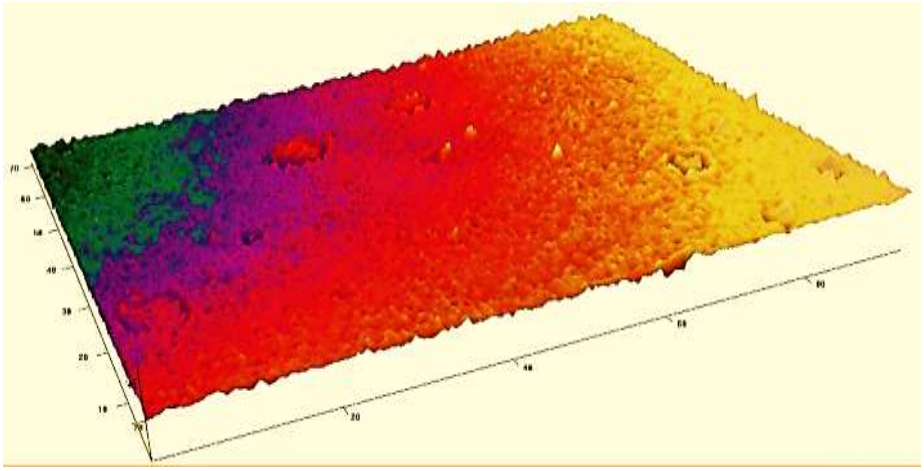

Figure 76a. 3D Optical profilometer image of $SLFgCRaNP_1$

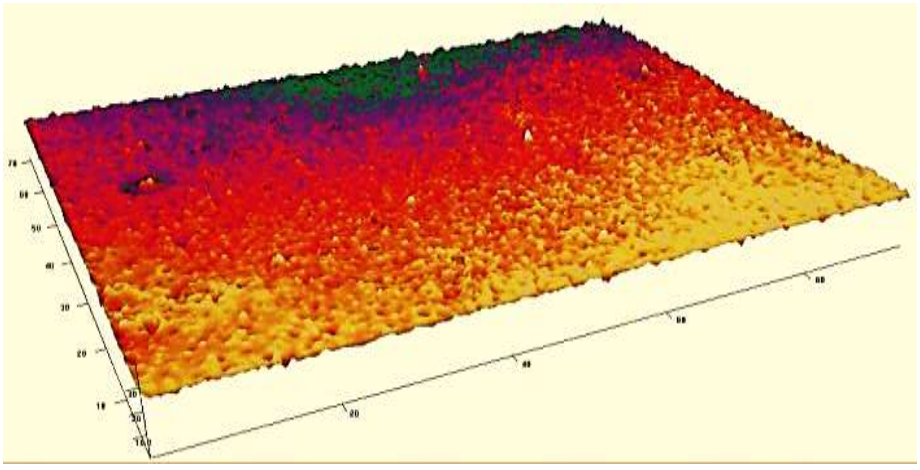

Figure 76b. 3D Optical profilometer image of $SLFgCRaNP_2$

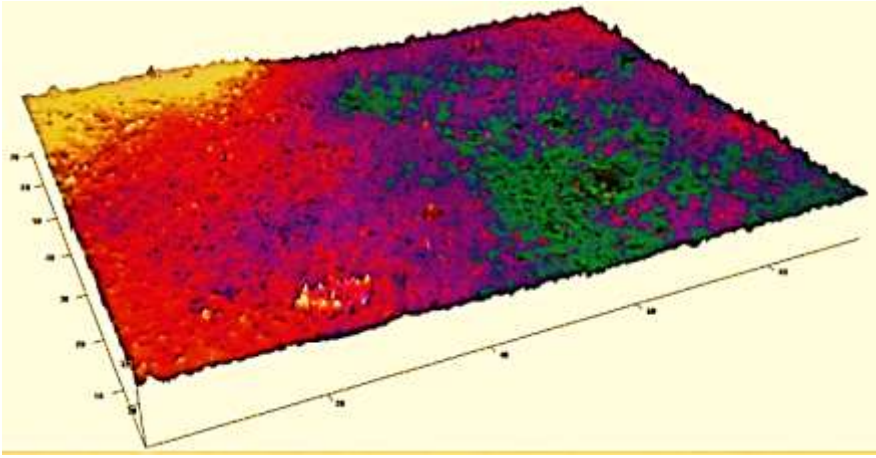

Figure 76c. 3D Optical profilometer image of SLFgCRaNP$_3$

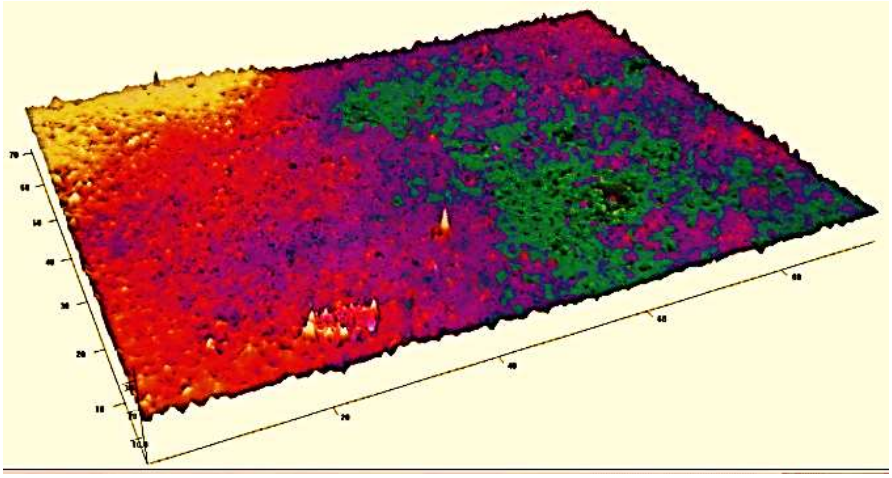

Figure 76d. 3D Optical profilometer image of SLFgHAaNP$_1$

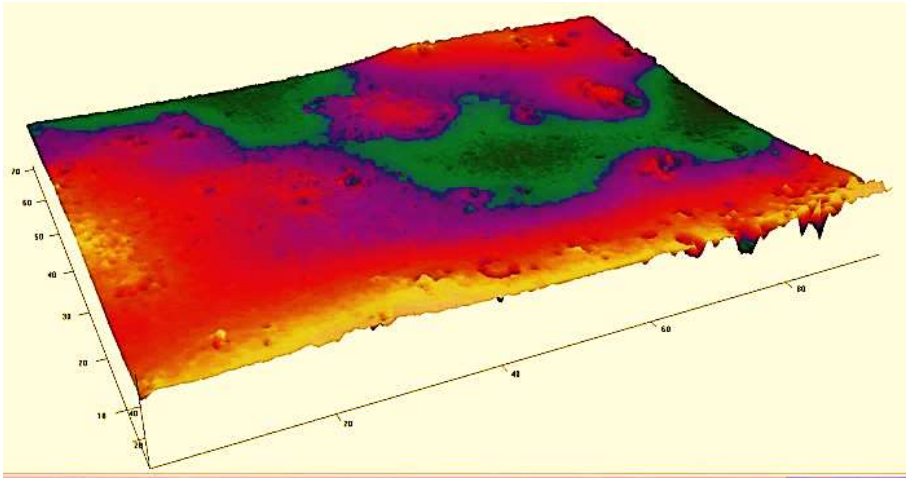

Figure 76e. 3D Optical profilometer image of SLFgHAaNP$_2$

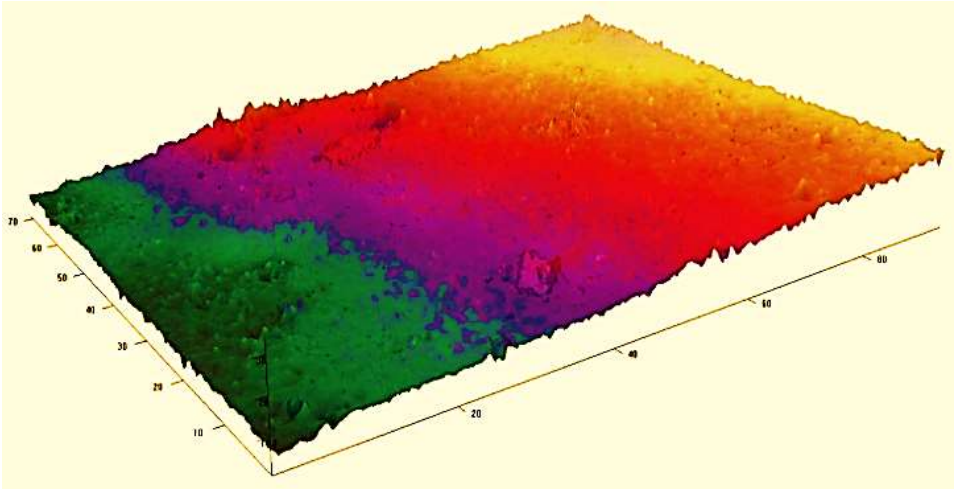

Figure 76f. 3D Optical profilometer image of SLFgHAaNP$_3$

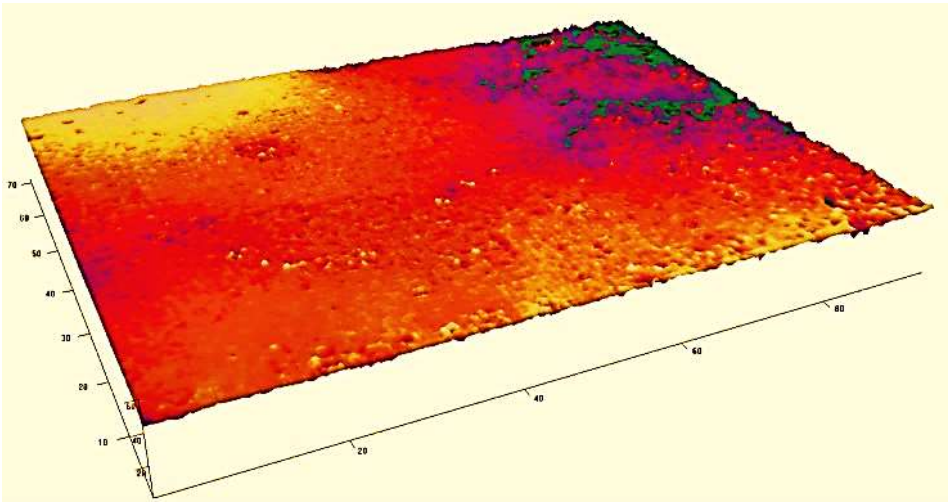

Figure 76g. 3D Optical profilometer image of SLFgNP$_0$

Figure 76a-g. 3D Optical profilometer images of prepared skin substitutes

4.13.4 FESEM images of prepared skin substitutes

The surface texture of prepared skin substitutes is shown in **Figures 77a-83a**. The SLFgNP$_0$ shows a very smooth texture with a high content of carbon and oxygen (**Figure 77a-d**). The surfaces of CRaNP treated nano skin are shown in **Figures 78a-80a**. Some swelling in the skin structure is observed in SLFgCRaNP$_3$ (**Figure 80a**). This may be due to the interaction of the beam with the plant metabolites present in the skin substitute. The uniform bubbles like texture were seen in HAaNP-treated skin substitute (**Figure 81a-83a**). Due to this bubble-like texture, HAaNP-aided

skin substitute may be responsible for more water uptake and water ageing capacity. All the skin substitutes possess high carbon and oxygen content due to the presence of carbon and oxygen chains in the polymeric structure. The gold nanoparticles are uniformly distributed in skin substitutes, which is observed in **Figure 78b-83b**.

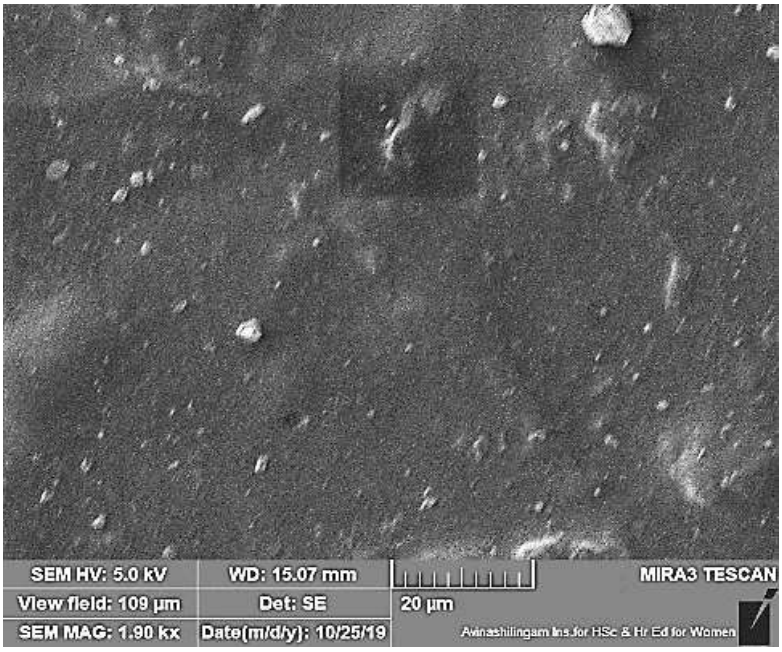

Figure 77a. FESEM image of SLFgNP$_0$

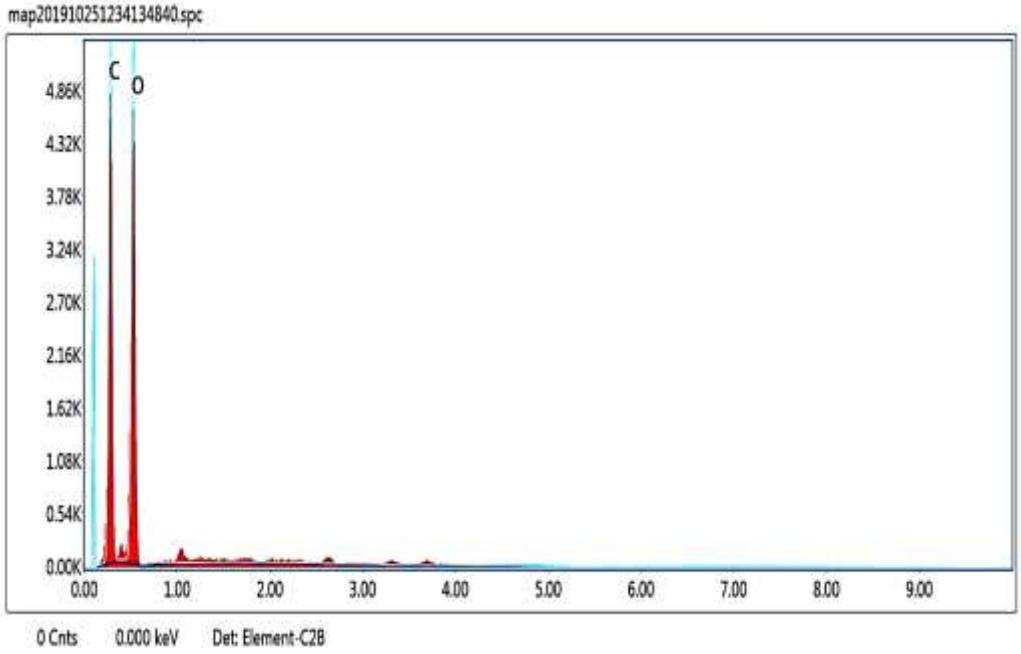

Figure 77b. EDS spectrum of SLFgNP$_0$

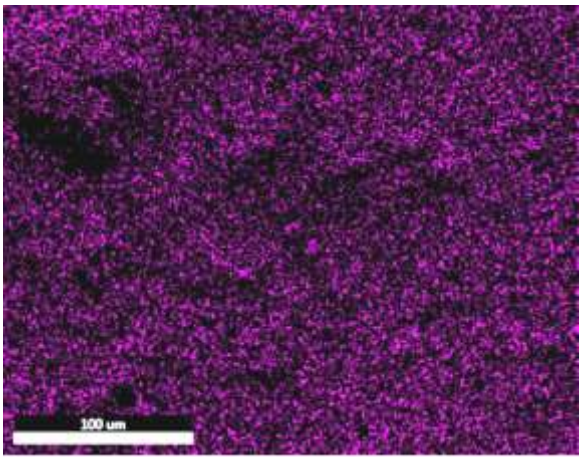

Figure 77c. Carbon distribution in $SLFgNP_0$

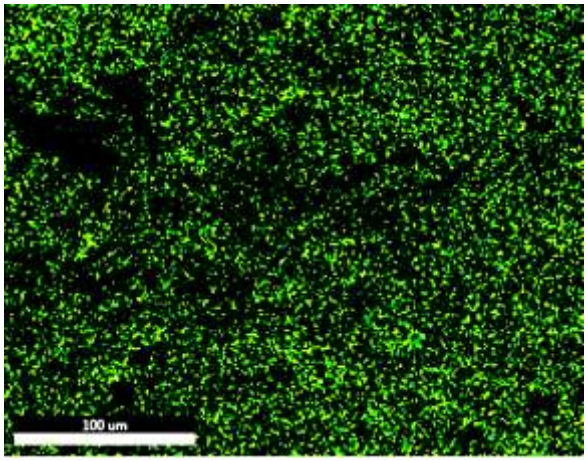

Figure 77d. Oxygen distribution in $SLFgNP_0$

Figure 77a-d. FESEM images of a) $SLFgNP_0$, b) EDS spectrum of $SLFgNP_0$, c) Mapping image of carbon distribution in $SLFgNP_0$ and d) Oxygen distribution in $SLFgNP_0$

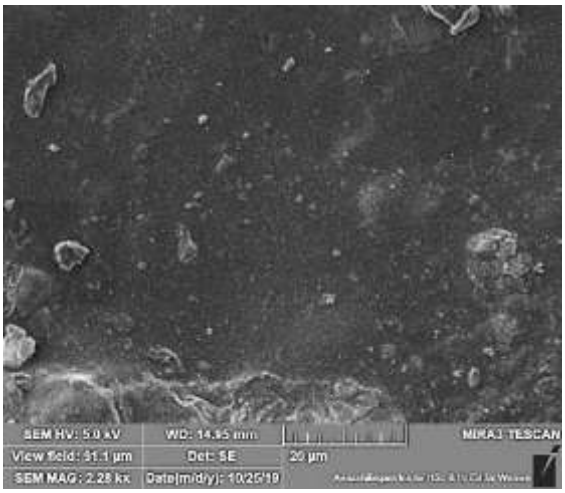

Figure 78a. FESEM image of $SLFgCRaNP_1$

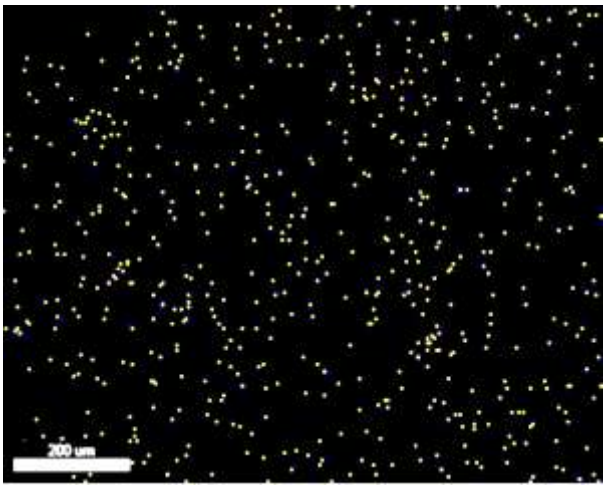

Figure 78b. Gold distribution in $SLFgCRaNP_1$

Figure 78a and b. FESEM images of a) $SLFgCRaNP_1$ and b) Mapping image of gold distribution in $SLFgCRaNP_1$

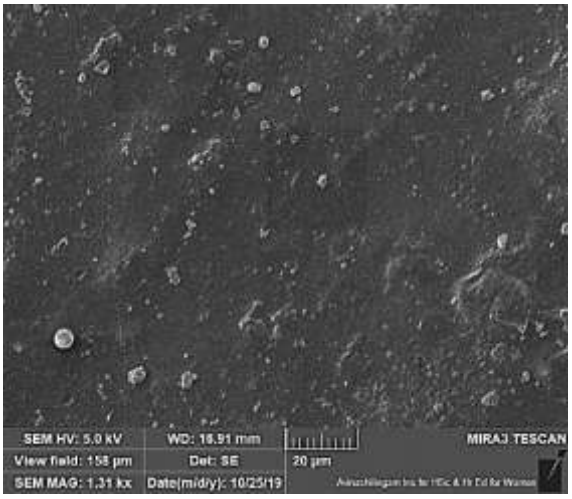

Figure 79a. FESEM image of $SLFgCRaNP_2$

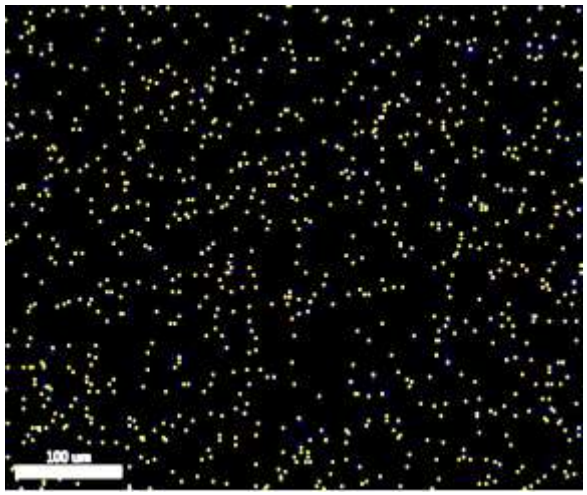

Figure 79b. Gold distribution in $SLFgCRaNP_2$

Figure 79a and b. FESEM images of a) $SLFgCRaNP_2$ and b) Mapping image of gold distribution in $SLFgCRaNP_2$

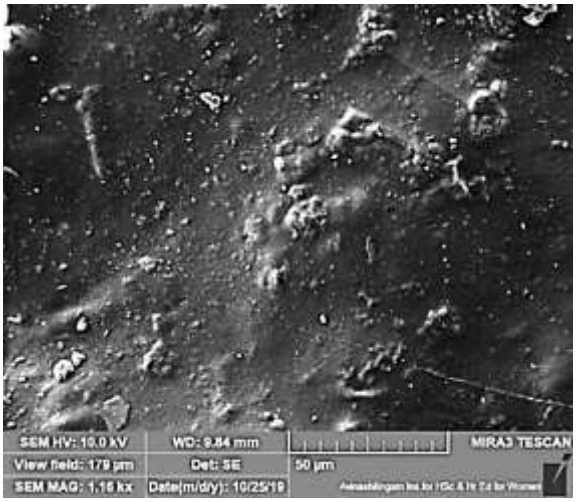

Figure 80a. FESEM image of $SLFgCRaNP_3$

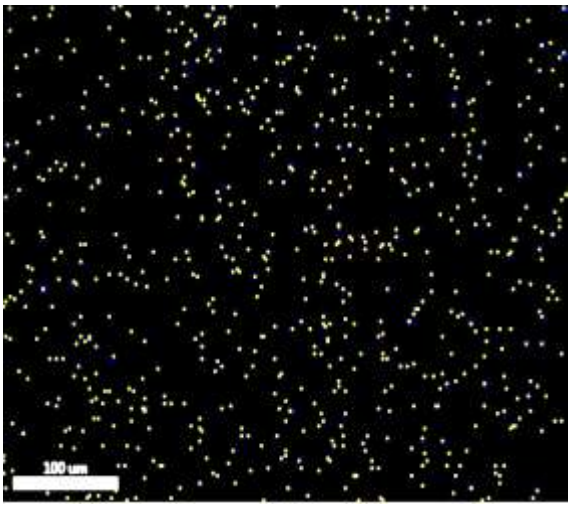

Figure 80b. Gold distribution in $SLFgCRaNP_3$

Figure 80a and b. FESEM images of a) $SLFgCRaNP_3$ and b) Mapping image of gold distribution in $SLFgCRaNP_3$

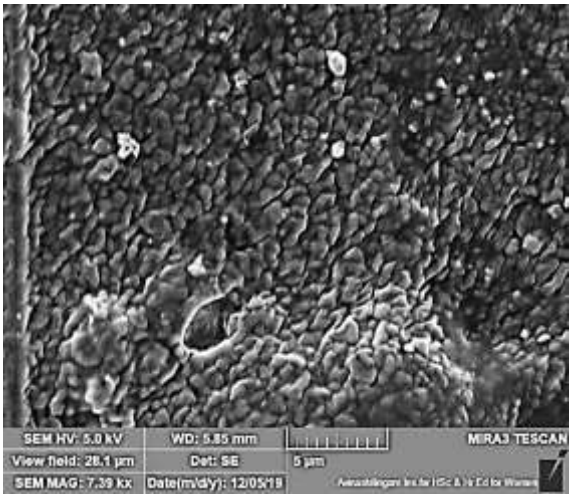

Figure 81a. FESEM image of SLFgHAaNP$_1$

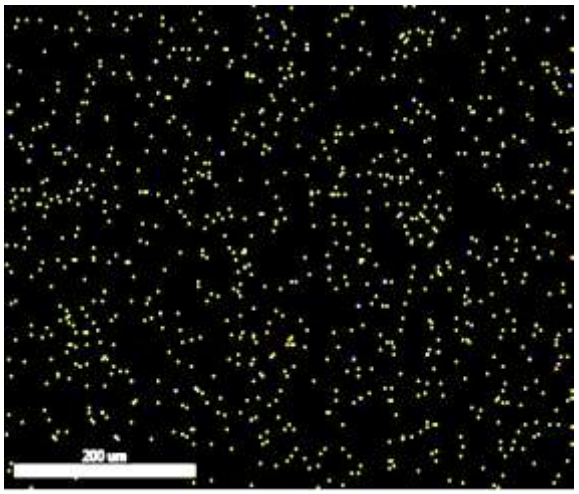

Figure 81b. Gold distribution in SLFgHAaNP$_1$

Figure 81a and b. FESEM images of a) SLFgHAaNP$_1$ and b) Mapping image of gold distribution in SLFgHAaNP$_1$

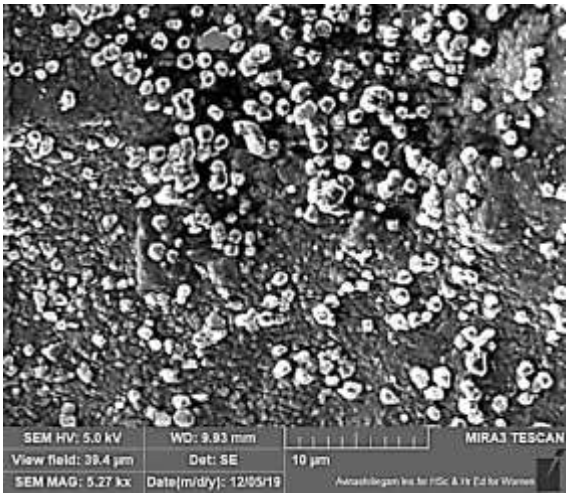

Figure 82a. FESEM image of SLFgHAaNP$_2$

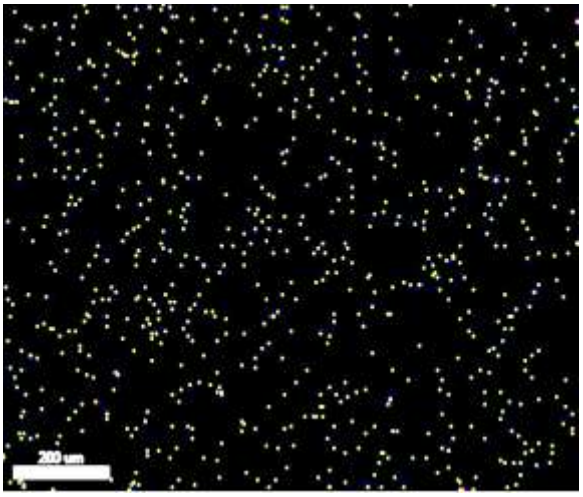

Figure 82b. Gold distribution in SLFgHAaNP$_2$

Figure 82a and b. FESEM images of a) SLFgHAaNP$_2$ and b) Mapping image of gold distribution in SLFgHAaNP$_2$

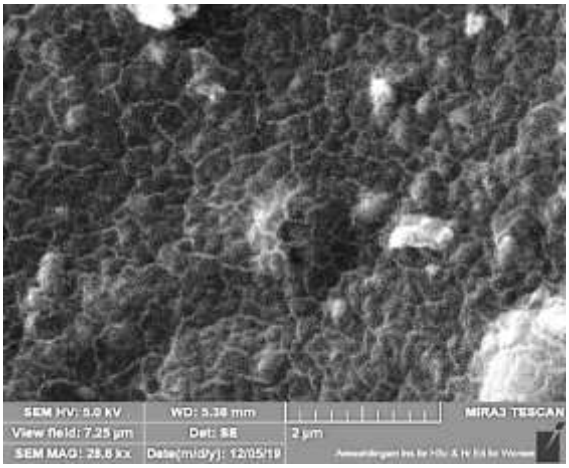

Figure 83a. FESEM image of $SLFgHAaNP_3$

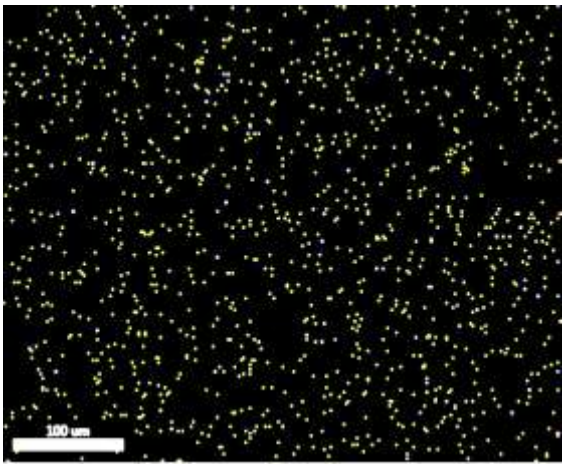

Figure 83b. Gold distribution in $SLFgHAaNP_3$

Figure 83a and b. FESEM images of a) $SLFgHAaNP_3$ and b) Mapping image of gold distribution in $SLFgHAaNP_3$

4.14 Results of biological activities of prepared skin substitutes

4.14.1 Results of antioxidant activity of prepared skin substitutes

Antioxidant activity of gold nanoparticle aided skin substitutes were tested using DPPH radical scavenging method. $SLFgNP_0$ shows less radical inhibition activity. Nanoparticles-incorporated skin substitutes show significant ($P<0.05$) activity by increasing the concentration of nanoparticles. **Figure 84** reveals the antioxidant potential of prepared skin substitutes. The highest inhibition potential was observed in the addition of higher nanoparticle concentration. The potential antioxidants of tea extract and plant embed nanoparticles present in samples enhance the free radical inhibition ability for the prepared skin substitutes.

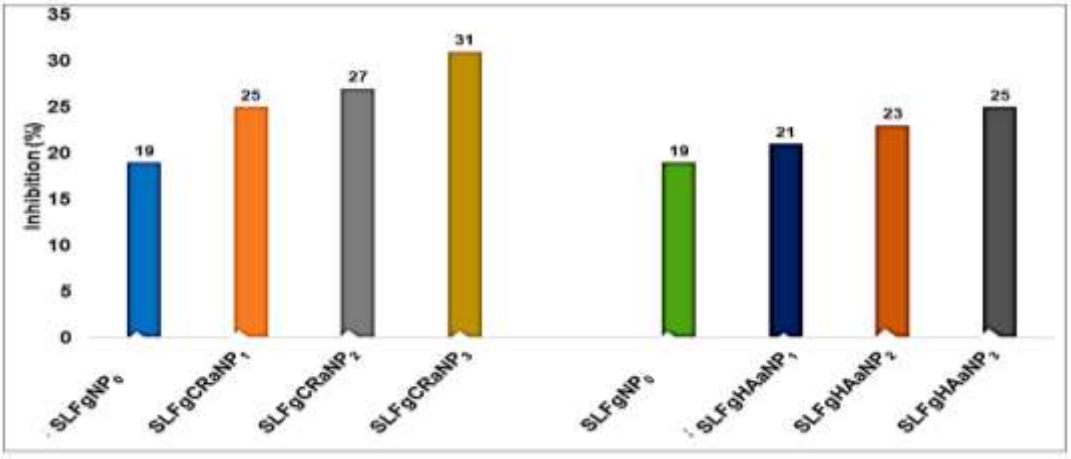

Figure 84. Antioxidant activity of gold nanoparticles-aided skin substitutes

4.14.2 Results of antifungal activity of prepared skin substitutes

Antifungal activity was tested against *Aspergillus niger* using the disk diffusion method (**Figure 85**). *Aspergillus* pathogens are responsible for severe skin infection, and it does not make responses with many antibiotics **(Prasanna Sarangan, 2016)**. The inhibition increases from 12 to 17 mm were observed using nanoparticles-aided skin substitutes. The highest inhibition zone was obtained using $SLFgCRaNP_3$ (15 mm) and $SLFgHAaNP_3$ (17 mm). The excellent antifungal activity against *Aspergillus niger* reveals that prepared skin substitutes are effective in skin-related cosmetic applications. The significant increase of inhibition may be due to the presence of bioactive plant embed gold nanoparticles.

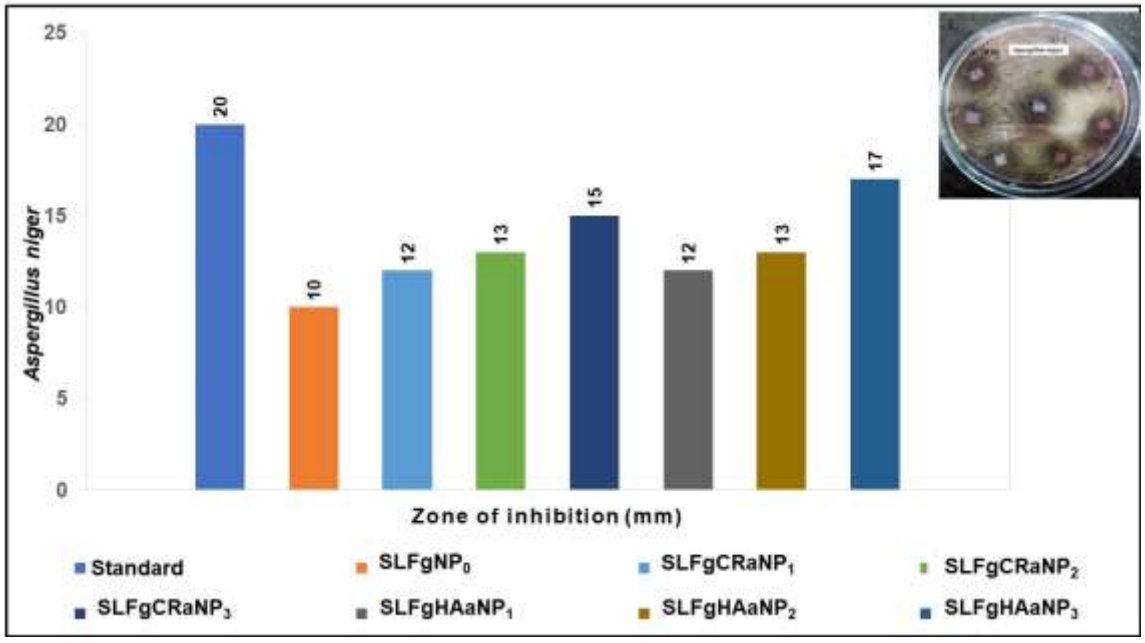

Figure 85. Antifungal activity of gold nanoparticles-aided skin substitutes against *Aspergillus niger*

4.14.3 Results of cell toxicity activity of prepared skin substitutes

4.14.3.1 Cell viability of prepared skin substitutes treated HEK-293 and A375 cell lines

The cell line toxicity of prepared skin substitutes against A375 and HEK-293 cell lines was evaluated using MTT assay and the results are given in **Table 37**. The cell toxicity of $SLFgCRaNP_1$ shows 6 to 67% on skin cancer cell line by increasing concentration from 50-250 µg/mL (**Figure 86b**). At a higher concentration (250 µg/mL), the sample shows the highest inhibition activity on A375. The toxicity of 4-77% and 4-65% observed for $SLFgCRaNP_2$ (**Figure 86c**) and $SLFgCRaNP_3$ (**Figure 86d**)

respectively. $SLFgHAaNP_1$ shows 25% cell toxicity against A375 cancer cell lines. $SLFgHAaNP_2$ and $SLFgHAaNP_3$ show 8-70 and 7-63% cell toxicity against A375 cell lines, respectively. The higher cancer cell line toxicity of 70 and 63% was observed at 250 µg/mL.

Using the prepared skin substitutes, the toxicity on normal cell lines shows less cell toxicity and more cell viability. The toxicity of $SLFgCRaNP_1$ shows 5-31%, $SLFgCRaNP_2$ shows 3-30% and $SLFgCRaNP_3$ shows 4-30% against HEK-293 cell line. The HAaNP-incorporated skin substitutes $SLFgHAaNP_1$ (**Figure 86e**), $SLFgHAaNP_2$ (**Figure 86f**) and $SLFgHAaNP_3$ (**Figure 86g**) shows 4-22%, 6-35% and 2-35% toxicity on normal cell lines respectively. The prepared samples show the highest cell toxicity on A375 cancer cells and minimum toxicity on HEK-293 cell lines. These results indicate that the prepared samples are biocompatible.

Table 37. Cell viability of prepared skin substitutes treated A375 and HEK-293 cell lines

S. No	Prepared skin substitutes	Cell viability (%)									
		A375					HEK-293				
		Concentration of samples (µg/mL)									
		50	100	150	200	250	50	100	150	200	250
1	$SLFgCRaNP_1$	94	50	42	36	33	95	83	75	71	69
2	$SLFgCRaNP_2$	96	34	30	27	23	97	88	80	76	70
3	$SLFgCRaNP_3$	96	47	43	37	35	96	90	85	79	70
4	$SLFgHAaNP_1$	96	89	80	78	75	96	90	86	80	78
5	$SLFgHAaNP_2$	92	78	46	37	30	94	75	70	67	65
6	$SLFgHAaNP_3$	93	87	50	41	37	98	78	70	68	65
7	$SLFgNP_0$	95	72	67	65	62	96	78	69	65	60
8	DOX	96	86	45	34	28	92	54	32	25	21

The IC_{50} values of prepared skin substitutes are given in **Figure 87**. The IC_{50} value of $SLFgCRaNP_2$, $SLFgCRaNP_3$, $SLFgHAaNP_1$, $SLFgHAaNP_2$ and $SLFgHAaNP_3$ obtained at 63, 76, 100, 120 and 125 µg/mL respectively. The IC_{50} values, obtained for standard (DOX) at 24 µg/mL. $SLFgCRaNP_1$ and $SLFgNP_0$ showed minimum toxicity on skin cancer cell lines up to 250 µg/mL.

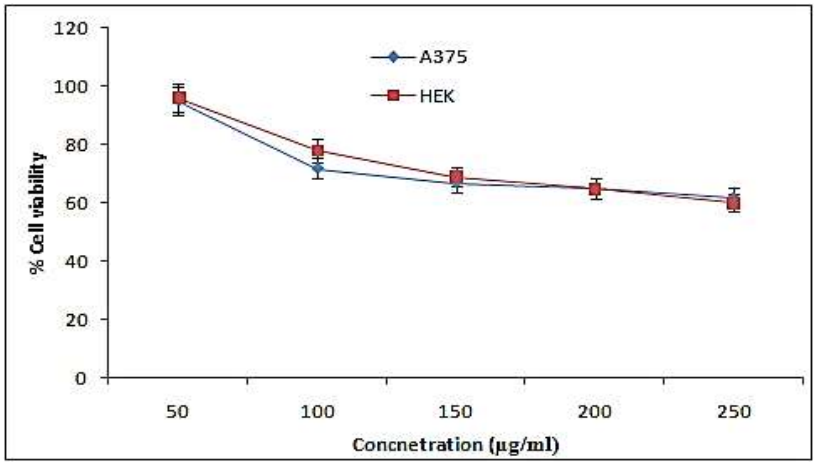

Figure 86a. Cell viability of $SLFgNP_0$

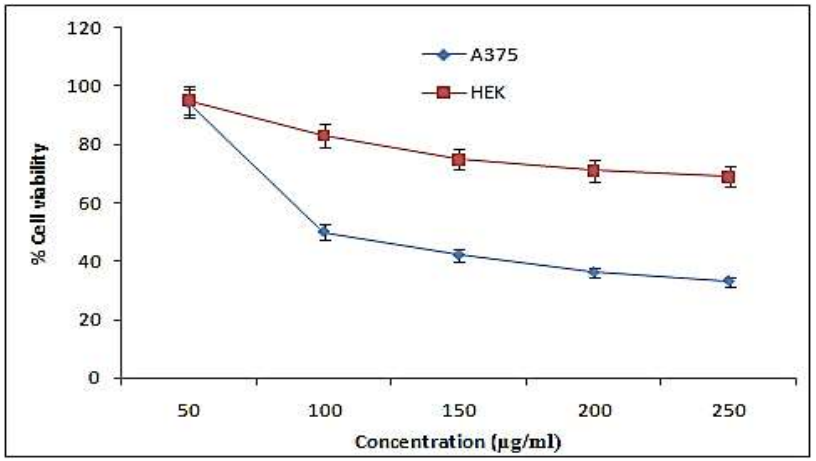

Figure 86b. Cell viability of $SLFgCRaNP_1$

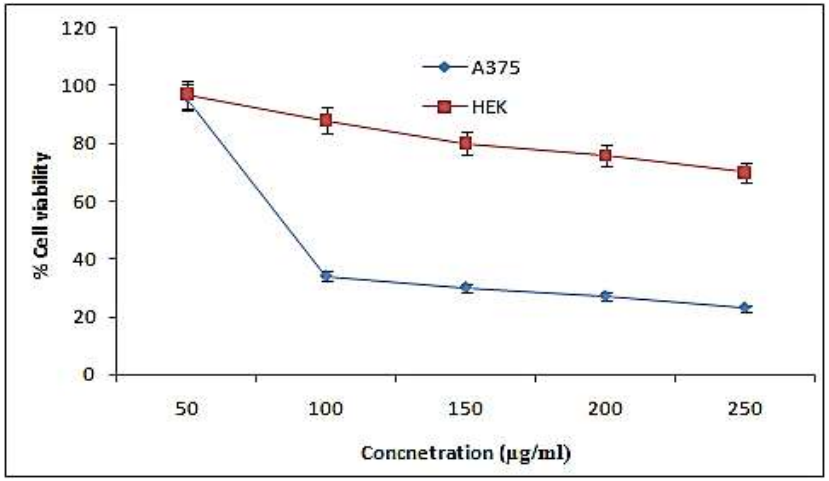

Figure 86c. Cell viability of $SLFgCRaNP_2$

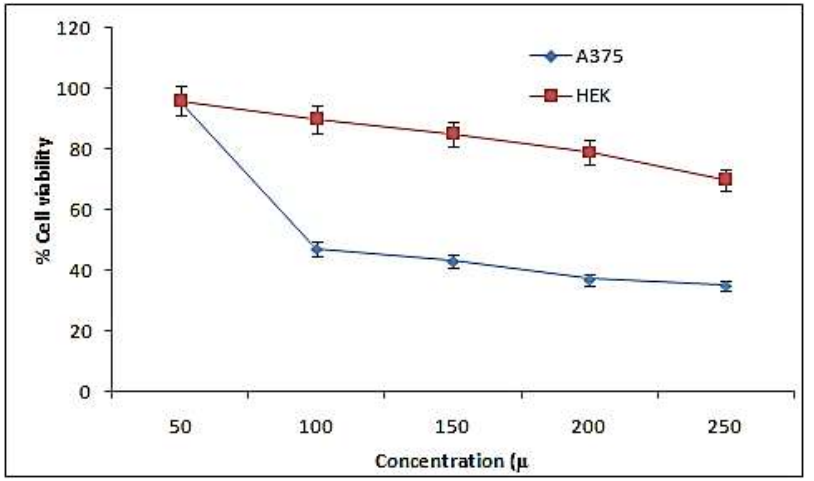

Figure 86d. Cell viability of $SLFgCRaNP_3$

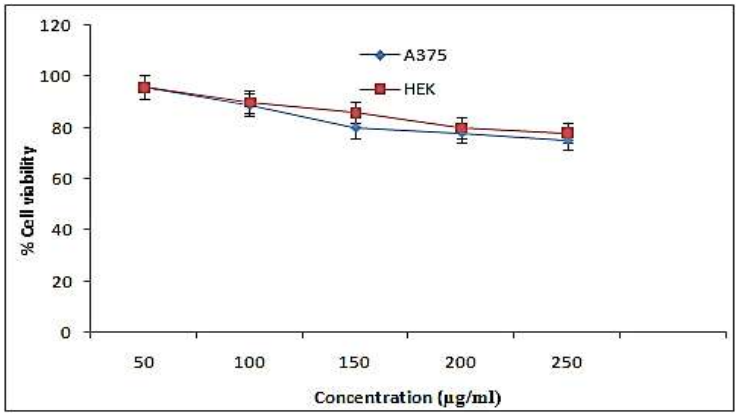

Figure 86e. Cell viability of SLFgHAaNP$_1$

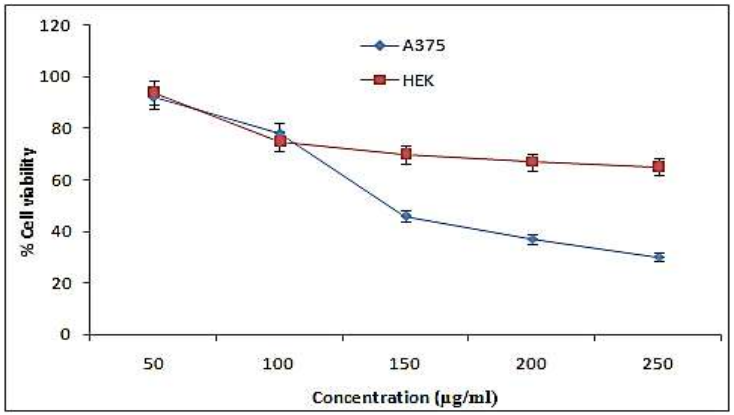

Figure 86f. Cell viability of SLFgHAaNP$_2$

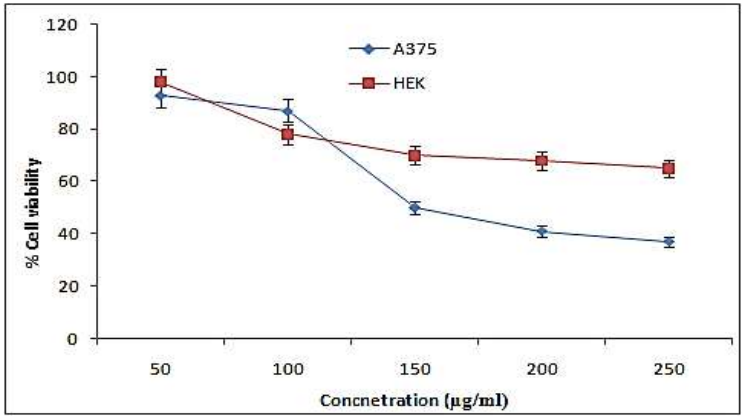

Figure 86g. Cell viability of SLFgHAaNP$_3$

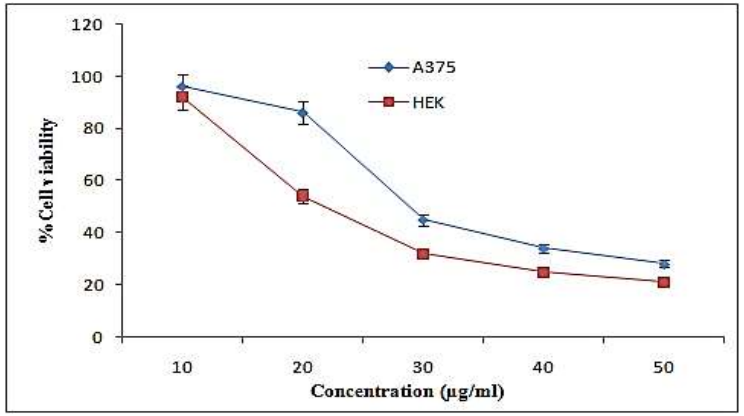

Figure 86h. Cell viability of DOX

Figure 86a-h. Cell viability of prepared skin substitutes a) SLFgNP$_0$, b) SLFgCRaNP$_1$, c) SLFgCRaNP$_2$, d) SLFgCRaNP$_3$, e) SLFgHAaNP$_1$, f) SLFgHAaNP$_2$, g) SLFgHAaNP$_3$ and h) DOX

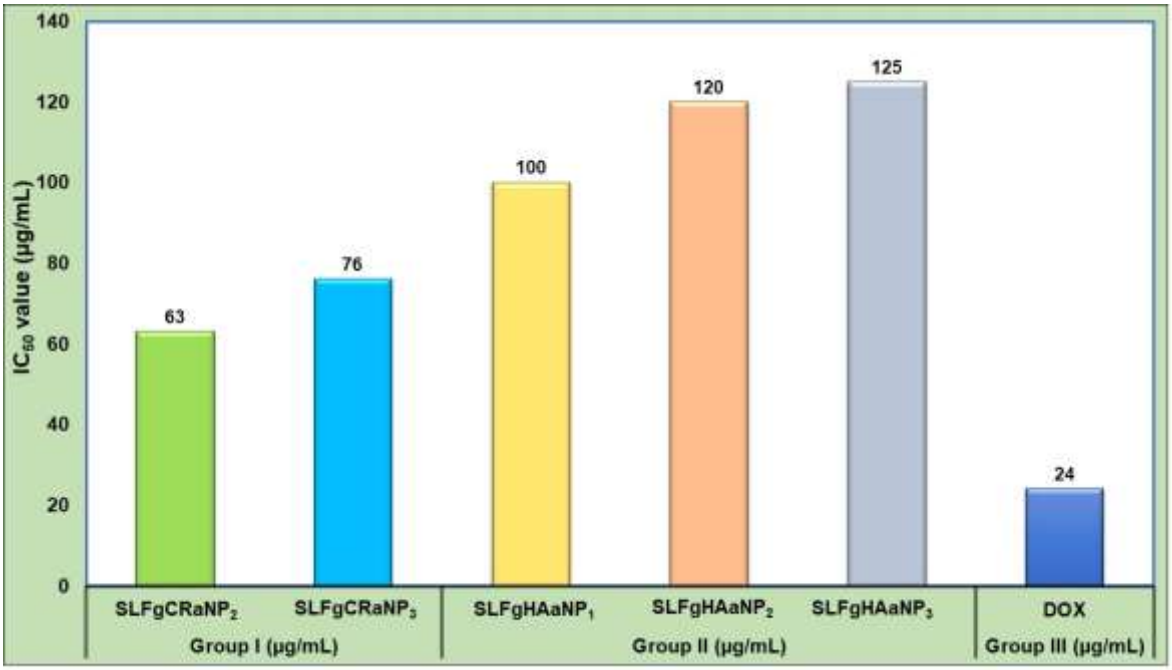

Figure 87. Graphical representation of IC_{50} value of synthesized skin substitutes against A375 cell lines

The prepared skin substitutes are contained biodegradable materials and possess highest drug-releasing and drug loading efficiency **(Malesu *et al*., 2011; Liu *et al*., 2012: Devi and Dilip, 2013; Mallikarjuna *et al*., 2015)**. In this study, biomaterials present in the samples are used to carry the plant embeds gold nanoparticles. The cell line inhibition results confirmed the release of the drug on to the cell structure. It is further confirmed by the AO/EtBr and PI staining method. The excellent targeting drug delivery of gold nanoparticles into the cell line nuclear level is shown in **Figures 88a and b**.

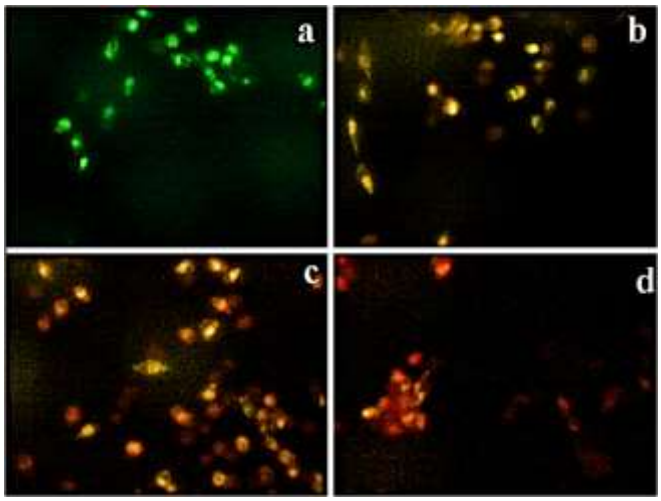

Figure 88a. AO/EtBr staining of $SLFgCRaNP_2$ treated A375 cancer cell lines

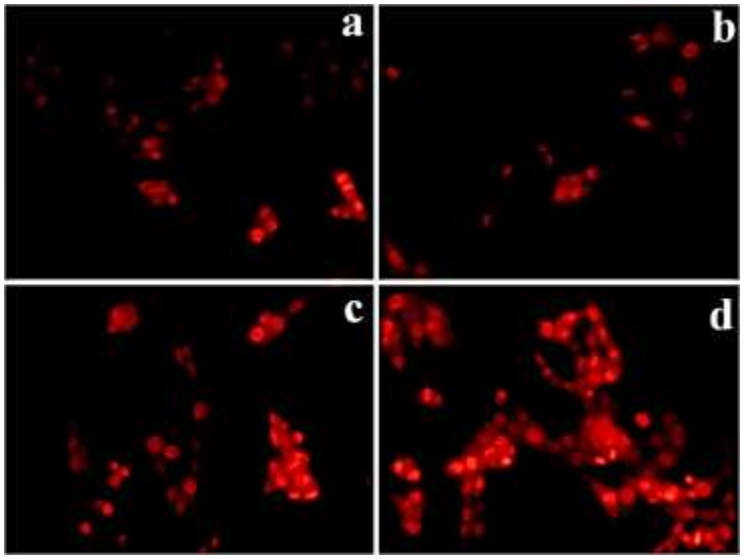

Figure 88b. PI staining of SLFgCRaNP$_2$ treated A375 cancer cell lines

Figure 88a and b. Cell damage and blistering in the cell structure of SLFgCRaNP$_2$ treated A375 cancer cell lines by AO/EtBr and PI staining

4.15. Cell growth and cell attachment studies of prepared skin substitutes

To analyze the cell growth on prepared samples, cells were cultured in a medium containing skin substitute. The cell growth was monitored for two days. Initially, the normal human cells were started to grow on both skin and cultured mediums, which is seen in **Figure 89a-c**. The maturity of the cells was observed after 24h treatment. After 24h, the cells were completely attached to the surface of skin substitutes, which is observed in **Figure 89d-f**.

Figure 89a. Image of HEK-293 cell lines and skin substitute in a cell culture medium

Figure 89b. Image of HEK-293 cell lines in a cell culture medium

Figure 89c. Image of HEK-293 cell lines in a cell culture medium

Figure 89d. Image of HEK-293 cell lines attachment in a cell culture medium

Figure 89e. Image of HEK-293 cell lines attachment in a cell culture medium

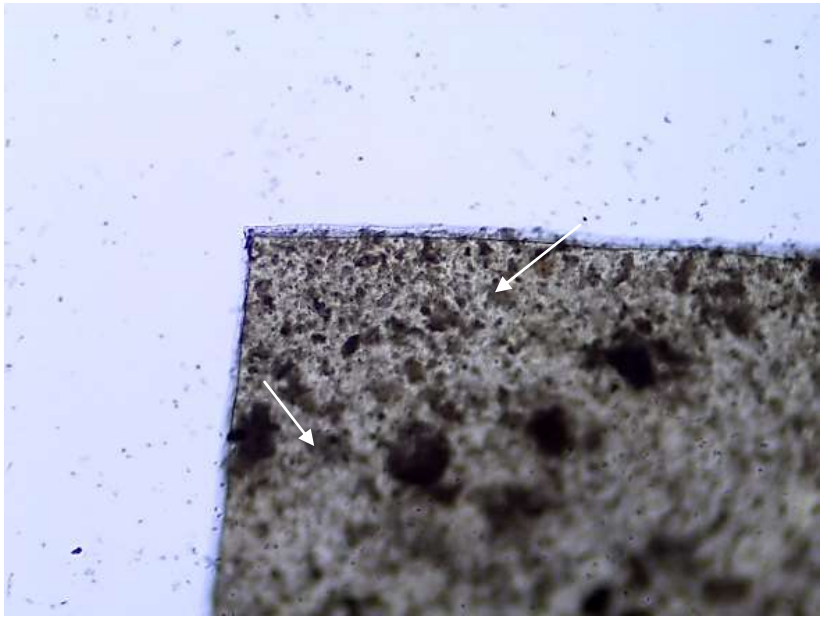

Figure 89f. Image of HEK-293 cell lines attachment in a cell culture medium

Figure 89a-f. Cell growth and cell attachment of HEK-293 cell lines on prepared skin substitutes

Chitosan, sodium alginate and gold nanoparticles are biocompatible and used in tissue engineering applications (**Cheng *et al*., 2010; Zhao *et al*., 2014; Kusumastuti *et al*., 2018)**. TiO_2 nanoparticles-aided skin substitute is used to recover the wound **(Peng *et al*., 2008)**. Alginate-gelatin hydrogels support fibroblasts attachment and cell viability **(Sarker *et al*., 2014)**. Hence the study results revealed the prepared plant embedded gold nanoparticle-aided skin substitutes to be biocompatible and hence suggested for use in artificial skin substitutes in tissue engineering and wound healing applications.